UNIVERSIDADE TECNOLÓGICA FEDERAL DO PARANÁ

RAFAEL BALDIN

IMPLEMENTAÇÃO DE ESPECTROFOTÔMETRO DE BAIXO CUSTO PARA DETECÇÃO DE MEG EM ÁGUA

CURITIBA

2023

RAFAEL BALDIN

IMPLEMENTAÇÃO DE ESPECTROFOTÔMETRO DE BAIXO CUSTO PARA DETECÇÃO DE MEG EM ÁGUA

Implementation of low cost spectrophotometer for MEG detection in water

Dissertation presented as a requirement for obtaining the Master's degree in automation and systems engineering from the CPGEI postgraduate program at the Federal Technological University of Paraná (UTFPR).
Advisor: Prof. Eduardo Nunes dos Santos
Co-advisor/Assistant: Marco José da Silva

CURITIBA

2023

Ministério da Educação
Universidade Tecnológica Federal do Paraná
Campus Curitiba

RAFAEL BALDIN

IMPLEMENTAÇÃO DE ESPECTROFOTÔMETRO DE BAIXO CUSTO PARA DETECÇÃO DE MEG EM ÁGUA

Trabalho de pesquisa de mestrado apresentado como requisito para obtenção do título de Mestre Em Ciências da Universidade Tecnológica Federal do Paraná (UTFPR). Área de concentração: Engenharia De Automação E Sistemas.

Data de aprovação: 20 de Dezembro de 2022

Dr. Eduardo Nunes Dos Santos, Doutorado - Universidade Tecnológica Federal do Paraná

Dr. Daniel Rodrigues Pipa, Doutorado - Universidade Tecnológica Federal do Paraná

Dr. Marcos Vinicio Haas Rambo, Doutorado - Universidade Federal do Paraná (Ufpr)

Documento gerado pelo Sistema Acadêmico da UTFPR a partir dos dados da Ata de Defesa em 24/02/2023.

ACKNOWLEDGMENTS

This work was only possible thanks to the contribution of many people from the CPGEI and NUEM. I am glad for all the support given by my family.

The present work was carried out with the support of the Coordination and Enhancement of Superior Level Personnel - Brazil (CAPES) - Financing code: 001.

RESUMO

O presente trabalho de dissertação de mestrado se propõe a produzir um protótipo de bancada capaz de detectar a proporção de uma solução líquida de monoetileno glicol. O módulo eletrônico utilizado para tal foi um espectrofotômetro, que é capaz de medir o conteúdo espectral de uma amostra de acordo com cada comprimento de onda que o sensor suporta, cada qual referente a uma frequência. Foram utilizadas vários LEDs como fontes de luz: ultravioleta (UV), azul, verde, amarelo e vermelho. Desses LEDs, o LED amarelo é o que obteve melhor resultado, sendo capaz de medir concentrações com mais de 50% de MEG e sem corante. Os LEDs UV e azul também obtiveram medições previsíveis, principalmente após processamento de dados. Os resultados foram satisfatórios por terem sido baseados a partir de gráficos de várias amostras e interpretando-os e identificando o comportamento do espectro. A partir disso, foram feitas curvas de predição de concentração de MEG.

Palavras-chave: Espectrofotômetro. MEG. Espectro.

ABSTRACT

The present Master dissertation aims to produce a bench prototype capable of detecting the amount of MEG in a liquid solution. The electronic module used for this was a spectrophotometer, which is capable of measuring the spectral content of a sample according to each wavelength the sensor supports, each referring to a frequency. Many LEDs were utilized was light sources: ultraviolet (UV), blue, green, yellow and red. From these LEDs, the yellow LED achieved the best result, to the point of measuring concentrations beyond 50% of MEG and without dye. The UV and blue LEDs also got predictable measures, mainly after data processing. The results were satisfactory because they were based on graphs of various samples and interpreting them and identifying the behaviour of the spectrum. From this, it was possible to plot charts predicting the amount of MEG in the samples.

Keywords: Spectrophotometer. MEG. Spectrum.

SUMMARY

1 INTRODUCTION

The petroleum industry has many challenges to overcome when it deals with liquid flow. When petroleum and gas are extracted from the bottom of the oceans, many things come along, especially water. This represents a tough challenge since the extraction system needs to be well suited to handle the incoming water, other substances and their reactions inside piping as well. Depending on how water behaves with other substances, the formation of hydrates is possible, thus generating cloggings. With this in mind, it is important to know how to deal with hydrate formation by inhibiting them with chemicals. These chemicals, in turn, need to be properly monitored in order to be properly used.

In order to achieve this, firstly, there is a need to measure this type of chemicals in a smaller scale before implementing it in a real case scenario. This means that small controlled samples should be used to validate sensoring methods such as spectrophotometry. When dealing with spectrophotometry, there are many light sources that can be used to validate, with some being more efficient than others depending on the analyte. With this being setted, it is therefore pertinent to explore different light sources to measure chemicals.

1.1 Motivation

The control of chemical inhibitors in pipelines is extremely important so that their use can be optimized. In order to achieve this, it is necessary to avoid problems with both lack and in excess of inhibitors. As they are used to prevent blockages from hydrates, if they are underused, they can be ineffective. However, if they are overused, there can be futile costs and perilous damage to the environment.

In this context, this work serves primarily to help projects dedicated to study the spectral behaviour of a chemical inhibitor called mono ethylene glycol (MEG) with the use of an optical sensor called spectrophotometer. Researchers can then understand how MEG behaves with this type of sensor and how to apply this for the best understanding and design of related projects. One example of

this is about injection efficiency, so when researchers understand the inhibitor's flow in water, they can then design better injection projects.

Another great contribution of the present work is that many LEDs (Light Emitting Diodes) of different colours were tested to their limits. This exploration opens many possibilities in order to show how accurate these light sources can be when measuring MEG.

1.2 Objectives

This work has the main goal of measuring the amount of MEG in water with a spectrophotometer. Thereat, it then becomes possible to attain relations between MEG's percentage and its spectrum's features. Therefore, this consists of:

1. creating an environment where no external light may hinder the accurate data acquirement;
2. making sure that the sensor works properly as it is intended to;
3. performing experiments with LEDs of different light colour;
4. developing algorithms to process the acquired data.

2 LITERATURE REVIEW

2.1 Petroleum industry

2.1.1 Mineral oil

Petroleum is essential in producing many important products, such as fuel and plastics. Because of this, petroleum is a crucial resource for the economy of any country. Commercial mineral oils are processed crude oil. Since crude oil is composed of many different fossils, it also renders a wide variety of oils. It is generally composed of paraffin (30%; range 15–60%), naphthenes (49%; range 30–60%), aromatics (15%; range 3–30%), and asphaltic (6%; remainder) (RAWLINGS; LOMBARD, 2012). Mineral oils are chains of hydrocarbons that can have a variety of forms. Petroleum is processed and refined in many ways in order to create a plethora of products. There are many industries that apply mineral oil, such as medicine, food, mechanical, electrical, and cosmetics. For these reasons, this type of chemical cannot only have many useful applications but can also bring many different impacts on the environment.

Petroleum, also known as crude oil, is a black liquid extracted from inside geological formations, from the bottom of the ocean to the depths of the earth. There are two sources of petroleum hydrocarbons in the context of the marine environment: the natural ones (also known as biogenic or diagenetic) and the anthropogenic ones (also known as petrogenic or pyrogenic ones (WU et al., 2001). Hydrocarbons from diagenetic sources refer to those produced by living beings, such as seaweeds, plankton, and bacteria (ADENIJI; OKOH; OKOH, 2017). However, they can also come from biological processes that involve terrestrial plants (ADENIJI; OKOH; OKOH, 2017). Hydrocarbons from pyrogenic sources usually are more prevalent in the environment than biogenic ones (ADENIJI; OKOH; OKOH, 2017). They are typically produced by a plethora of human activities that involve oil usage somehow, be that in the industries, food collection (such as fishing) or means of locomotion (NNUAR et al., 2008; STROTHER; LOWRY; BRAVO, 1987). Figure 1 illustrates how a well is drilled in order to reach a natural source

of oil reserves. The extraction of mineral oil and gas comes along with sea water. It is an undesirable procedure, but it is also a inevitable one.

This produced water (PW) comes in an enormous volume generated from the petroleum drilling (KURAIMID et al., 2021), to the point of being up to eight times bigger in terms of volume than the crude oil extracted (IGWE; SAADI; NGENE, 2013). As it can be seen in figure 1, PW is water stuck in an underground rocky reservoir and is guided to the surface along with the main products, which are crude oil and natural gas (KURAIMID et al., 2021). This creates a three-phase flow that can be seen in figure 2.

Figure 1 - Well drilling

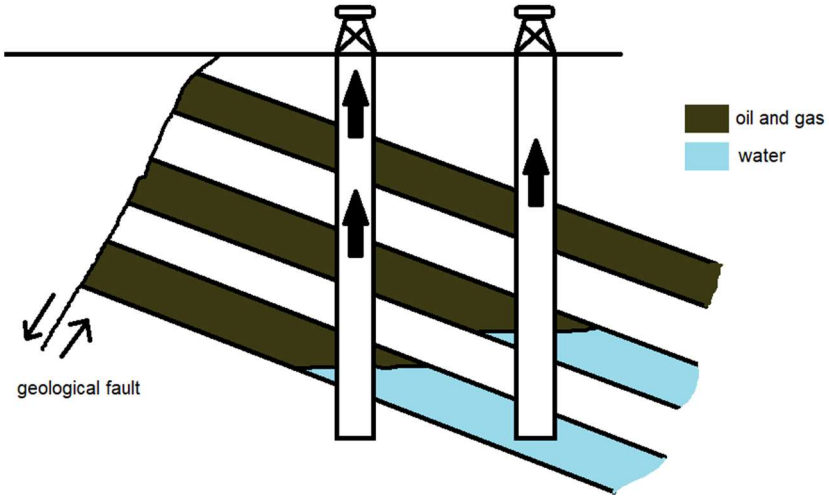

Source: Own authorship (2023).

2.1.2 Hydrate formation

In order to understand how hydrate formation works, figure 2 illustrates how the stream of petroleum extraction works until it suffers with hydrate formation. As the flow goes up, gas goes up first, oil second, and water last. This is due to their densities, with the water having the heaviest one. Therefore, when they are sucked up, gas is the first to reach the surface, followed by oil. The water, however, is kept behind until the oil is extracted. If there is any necessity to stop the process, the water is left underneath. Because of the high pressure (around 6894757 Pa) and low temperature (approximately 4 ºC), this enables the occurrence of gas hydrates when this water comes in contact with the natural gas

and oil (alkanes like methane) that are coming below it (GAO, 2008). This contact freezes the water in such a way that it agglomerates and interrupts the stream. Therefore, it is necessary to intervene, which is very costly.

It is worth noting that PW contains much more substances than just oil, such as: heavy metals, organic compounds, and anions (PERRY; GIGLIELLOK, 1990). PW is a blend of injected water, hydrocarbons, formation water, and chemicals related to the treatment (STRØMGREN et al., 1995). This treatment must occur with the PW located right before the oil that is being extracted to the surface.

Figure 2 - Petroleum flow interrupted by hydrate formation

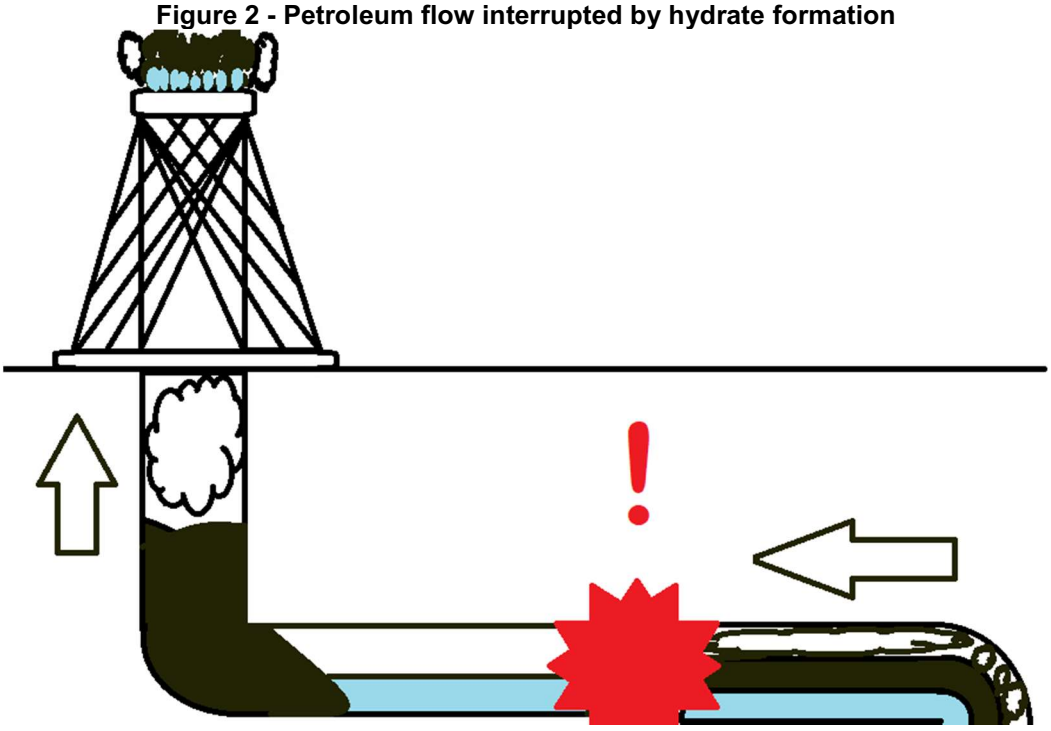

Source: Own authorship (2022).

2.2 Antifreeze methods

Considering the problem previously mentioned, it is imperative to find a solution to the problem of hydrate formation. Essentially, the following procedures help to decrease its formation: increase the temperature, lower the pressure, reduce the water volume and alter the freezing point. The following methods factor in at least one of these parameters. They can be used conjointly or not depending on the situation.

2.2.1 Pressure control

This method is about the decrease of pressure. It is not considered to be practical since high pressure is needed to conduct the flow up to the surface (ADISASMITO; PARUBAK, 2019).

2.2.2 Thermal insulation

This method helps to keep the temperature above the freezing point by covering the pipe with a material that prevents heat loss (ADISASMITO; PARUBAK, 2019).

2.2.3 Heat treatment

This method is about a heating mechanism alongside steel tubes, because the rise in temperature hinders hydrate formation (ADISASMITO; PARUBAK, 2019). However, this solution does not apply to the entire pipeline. The heaters do not cover some parts, and the oil may lose its properties, thus leading to hydrate formation (ADISASMITO; PARUBAK, 2019). Another downside is that it is costly since it needs some constant energy to keep it running (ADISASMITO; PARUBAK, 2019).

2.2.4 Gas-liquid separation

This method divides the liquid (water plus oil) phase from the gas phase. In order to implement this method properly, this needs to have an appropriate infrastructure in mind, and it still requires another method to support it, like chemical methods (ADISASMITO; PARUBAK, 2019).

2.2.5 Chemical methods

An usual strategy to deal with hydrate formation is to inject inhibitors in the form of chemicals. They can be divided into low-dosage hydrate inhibitors

(LDHIs) and Thermodynamic hydrate inhibitors (THIs).

2.2.5.1 Low-dosage hydrate inhibitors (LDHIs)

LDHIs can be separated into two groups: kinetic hydrate inhibitors (KHIs) and anti-agglomerates (AAs) (ARGO et al., 2000; FU et al., 2002; LEDERHOS et al., 1996; MITCHELL; TALLEY, 1999; NOTZ et al., 1996). KHIs manage hydrate formation by either retarding its nucleation or impeding its growth inside a specific area of sub-cooling (YANG; TOHIDI, 2011). AAs work differently, as they do not hinder the hydrate formation but obstruct the agglomeration of crystals just so that the oil remains transportable (YANG; TOHIDI, 2013).

2.2.5.2 Thermodynamic hydrate inhibitors (THIs)

Alcohols like methanol (MeOH) and mono-ethylene glycol (MEG) are typical examples of this type of inhibitor. They hinder the hydrate formation by lowering the temperature freezing point as well as increasing the pressure freezing point (YANG; TOHIDI, 2013). Thus, the water activity is reduced (YANG; TOHIDI, 2013). It can be worth noting, though, that the opposite can also happen (increase in temperature and lower in pressure) with the use of substances like tetrahydrofuran (THF) (MECH; GUPTA; SANGWAI, 2016), thus having essentially the same effect. Although, this is done more in the context of gas retention and transportation (QUEIROZ; RODRIGUEZ; CAJAIBA, 2020).

2.2.5.2.1 MEG

MEG stands for mono-ethylene glycol. It is a colourless, nearly odorless, hygroscopic, non-volatile, with low viscosity, highly soluble in polar solvents, with low chances of lighting on fire, with high availability, and thermodynamically stable (ZABOON et al., 2017) liquid alcohol constituted of organic compounds. This substance originates from hydrated ethylene oxide after passing through a thermal process or a catalytic one (SHELL, 2002).

MEG is mainly used for the manufacture of polyester fibres, in the context

of the textile industry, and polyethylene terephthalate resins (PET), in the context of the packaging industry (VEXIM, 2015). Due to all of the characteristics mentioned above, MEG is also very useful in many industrial segments, such as automotive, technologies of manufacturing, energy, transportation, and chemical (PAIVA et al., 2021). Some other significant uses of this chemical are: a drying agent for natural gas production, as fuel for batteries, as well as a refrigerating liquid for the production of beers and cars, and as defrosting of airplane windscreens (GRAS et al., 2015; HU; WANG, 2012; LEE et al., 2012, 2016; LUONG et al., 2013; PRODROMIDIS et al., 2001; SEMENOV et al., 2016). However, it is also used as an inhibitor of corrosion and antifreeze (VEXIM, 2015). In the context of this work, the application is to avoid antifreeze inside petroleum pipes.

In this context, MEG is very important to insert in PW so that the hydrate formation can be avoided. MEG is mixed with the stationary water so that hydrate formation can be avoided.

Despite being more costly, MEG is increasingly in its usage because it is more reclaimable than methanol thanks to MEG reclamation facilities (MCDOWELL; UTTAMLAL; GRAHAM, 2016). The global market of this substance is expected to expand from US$ 38.4 Bn in 2022 to US$ 65 Bn by 2032, with petrochemicals also included becaused of its UV absorbance curve being very particular (MAHENDRA SINGH, 2022).

2.3 Sensors

Some methods to monitor the concentration proportion of THI are UV-Vis spectroscopy, NIR absorption spectroscopy, and electrical conductivity (MCDOWELL; UTTAMLAL; GRAHAM, 2016). Most of these methods can rely on sample production. They can also be constrained by just sensing low THI proportions (MCDOWELL; UTTAMLAL; GRAHAM, 2016).

2.3.1 Ultrasonic sensor

It consists mainly of a transductor that sends and receives sound waves,

relying on the reading of signal energy and the propagation speed to measure the concentration of substances (REYNA et al., 2021). It is possible to measure THIs with the use of this type of sensor with satisfactory results in terms of accuracy (YANG; TOHIDI, 2011).

2.3.2 Electrical impedance and capacitance

Electrical sensors measure according to the behaviour of the flow, as the current or tension's behaviour can have a relation with chemical products concentration, like THIs and salts (YANG; TOHIDI, 2013). The electrical technique has the benefits of being safe, easy to operate, cheap, and quickly responsive (AN et al., 2014; PAL; VASUKI, 2018; STRAZZA et al., 2011; WU et al., 2015; ZHAI et al., 2015). The electrical technique can either be non-intrusive and intrusive (YANG et al., 2021). The non-intrusive methods consist of the electrodes being installed around the fluid. In contrast, the electrodes with the intrusive methods are mounted into the flow field to be in touch with the flow directly (YANG et al., 2021).

An example of this type of sensor is the one with capacitors. Its structure usually consists of one or multiple pairs of electrodes installed either on the external or the inner side of the tube walls (YANG et al., 2021). The capacitance rises proportionally to the height of the water layer (YANG et al., 2021). Capacitors can also be used along with tomography and this can be used to acquire water retention and establish the pattern of the flow in real-time (MOHAMAD et al., 2016; PERERA et al., 2017; SARDESHPANDE; HARINARAYAN; RANADE, 2015; YANG, 1996; YANG; PENG, 2002). However, this technological evolution lacks spatial resolution (YANG et al., 2021). Furthermore, despite measuring full-range retention, their sensitiveness is relatively small for great water retention circumstances (WU et al., 2015).

2.3.3 Optical sensors

There are many variations when it comes to optical sensors. They can

be a fiber-based antenna sensor with image processing, a spectrometer (MASSARO et al., 2012), or even a sophisticated camera for video metric applications. Since they do not need direct contact with flow container, they are considered non-destructive, non-intrusive, and non-invasive. Although they rely on specific light conditions to work correctly, they do not suffer from environmental issues, such as electromagnetic fields (MAHANTA; LASKAR, 2018).

2.3.3.1 Spectrum definition

The spectrum can be defined as a conglomerate of electromagnetic waves. They are defined by how energy behaves according to different frequencies of transmission. They are often classified by radiation type, such as radio, microwave, infrared, ultraviolet, x-ray, and gamma-ray. They are also measured according to wavelength (m). In the context of spectrometers, wavelengths are referred to in terms of nanometres. Considering the spectral bands that really matter for optical sensors, those are the ones from the ultraviolet (around 370 nm) to the infrared (around 750 nm). Within this range, it can be admitted that there is a group called “visible light”, which is the only visible scope in the entire spectrum. This is illustrated in figure 3.

As shown in figure 3, within the visible spectrum, there are some tagged colors. Violet (V – up to 450 nm), blue (B – from 450 nm to 495 nm), green (G – from 495 nm to 570 nm), yellow (Y – from 570 nm to 590 nm), orange (O – from 590 nm to 620 nm), and red (R) are the primary colours that represent segments of light. In the context of identifying substances, each one of them has more or less intensity within the visible spectrum. Substances, like any other visible object, absorb and reflect different colors, thus denoting a pattern that can be cataloged for calibration and verification purposes. This means that some substances can have somewhat more predictable results than others, especially if the sensor used is a colorimeter to analyse well consolidated colours. This would require the analyte to be massive and consistent. Otherwise it would not bring precise results. In any case, spectrometers have the advantage of being able analyse more in-depth, thus generally giving more reliable results.

Figure 3 - Electromagnetic spectrum and its visible part

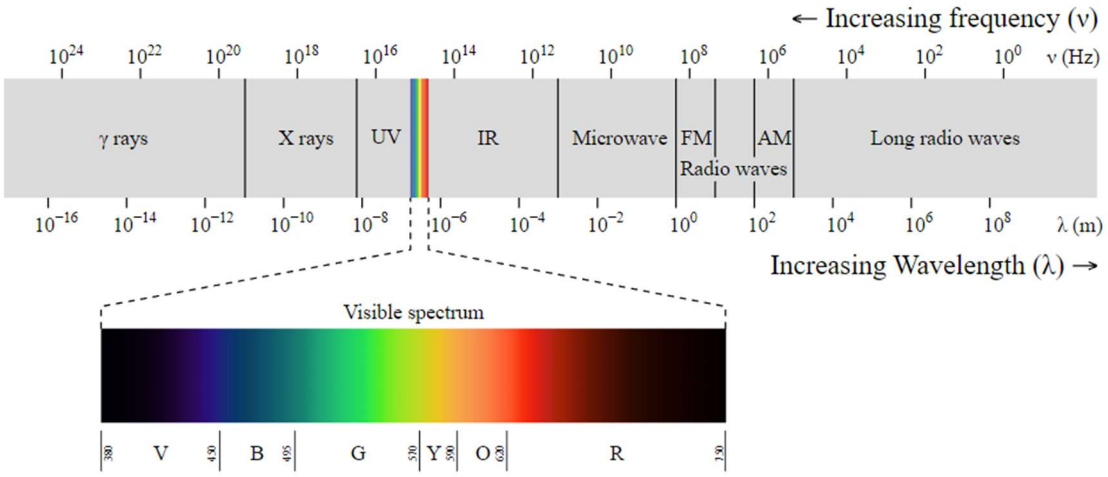

Source: WIKIMEDIA COMMONS CONTRIBUTORS (2022).

2.3.3.2 Spectrometers and spectrophotometers

This type of method is about quantifying or identifying an analyte according to the intensity of an electromagnetic radiation. This can be either visible or not (DITTES, 2013). Spectrophotometers rely on the same premise, as they can be considered a type of spectrometer. The difference relies on the use of photometers by spectrophotometer, as this sensor is focused on waves among infrared and ultraviolet.

Spectroscopic solutions are basically comprised of a transmitter and a receiver, in which a substance sample is located between them. The transmitter is a light source, while the receiver is a detector. Figure 4 illustrates how a spectrophotometer works.

Figure 4 - Generic internal spectrometer operation

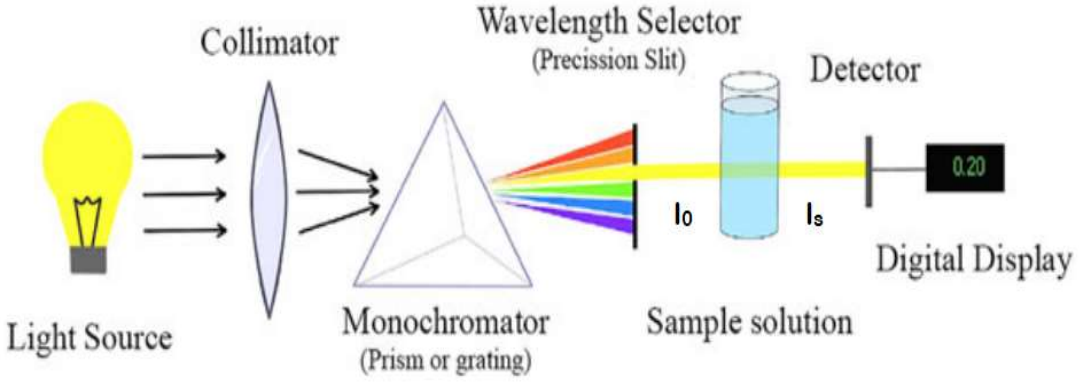

Source: BALADO SÁNCHEZ et al. (2019).

The light passes through a collimator, which tapers the light into a prism. This prism scatters many light colors toward a substance. The remaining light that managed to pass the sample goes to a detector. This detector serves to acquire data and then it displays it somehow.

When it comes down to identifying small changes in a mixed solution, spectrometers are capable of showing changes that are not even noticeable to the naked eye. Spectrometers are also more reliable than colorimeters since they can read solutions in depth, not just the surface of the solutions. Thus, they acquire more in-depth data in the same reading.

Spectrometers have many applications in the industry, such as: inspection of food, biometry, light testing, and environment mensuration instruments (e.g. liquid quality control) (ATTACHMENT 1).

2.3.3.3 Lambert-Beer Law

The Lambert-Beer Law serves to describe the interaction of light brightness when it passess through container of substances, so to discover how much light is detained in it (NURJAYADI; ROMUNDZA; MOERSILAH, 2021). The brightness strength depends in both on the solution's concentration (how much it is capable of absorbing light) as well as on the coating's thikness (NURJAYADI; ROMUNDZA; MOERSILAH, 2021).

This law is the core of the spectrometer's operation. Figure 4 shows the terms I_0 and I_S between the sample solution. They refer to initial beam and final beam, respectively. The ratio between them will denote the transmission of a given substance to a given wavelength. The equation 1 represents this relation.

$$T = \frac{I_S}{I_0} \quad (1)$$

Factoring in that there are multiple wavelengths, the end result is a vector of light intensities. This vector is used to create the transmission curve of a given substance. Based on that, it becomes possible to assess different sample solutions with similar substances to identify and even categorize their differences.

The concept of absorbance is necessary to understand in order to understand how concentration is measured. The equation 2 is about the relation between absorbance and transmission.

$$A = -\log_{10}(T) \quad (2)$$

Absorbance is also given by the equation 3, which contains the following terms: absorvity (ε), container length (l), and concentration (c).

$$A = \varepsilon l c \quad (3)$$

Out of these three, only concentration varies, which makes it directly proportional to the absorbance. Therefore, it enables the use of spectrometers to analyze a solution's concentration.

In this work, generic terms like "amplitude" or "intensity" are used in place of terms like "absorbance" or "transmittance" to describe the analytes response.

2.3.3.4 State of art

Three studies on MEG analysis with spectrometers were assessed. These studies are extremely similar to the current work, with some differences in spectrometer types and analyzed analytes. They are presented in chronological order.

The first study used two laser diodes from LaserBOXX, one in green and another in red, with the help of a fiber-optic to measure THIs.

The sensor used was a Hammamatsu C10082CA TM series mini-spectrometer, a much more sophisticated sensor used in this work (around 15 times the price, for instance). The sensor was successfully implemented to measure both MeOH and MEG up to 50% of their concentration, as shown in figure 5. The solution also consisted of saline water, while merocyanine 540 (MC540) and 3,3'-diethylthidicarbocyanine iodide (DTDCI) were the dyes used

with the THIs, with the former having its absorbance peak at 533 nm (green wavelength) and the latter having its absorbance peak at 645 nm (red wavelength) (MCDOWELL; UTTAMLAL; GRAHAM, 2016). These dyes were respectively excited with their closest laser diodes in terms of wavelength. Δλ can be described as the difference between the overtone peak wavelengths that could be observed in the solutions with salt.

Figure 5 - Calibration graphs of THIs

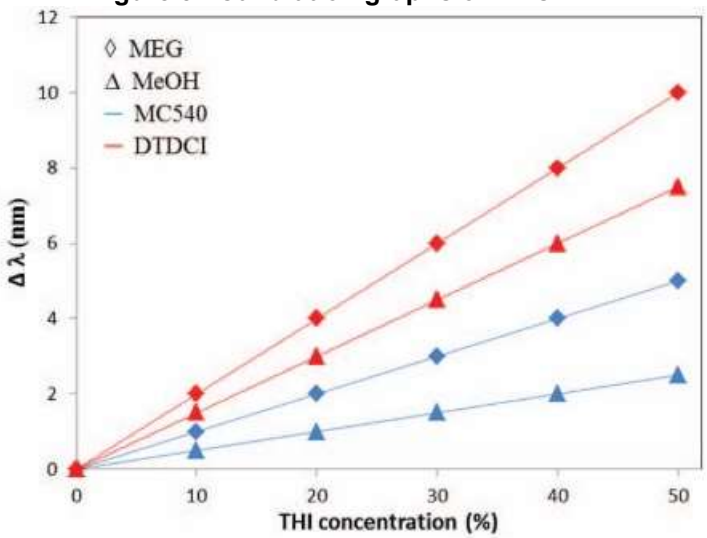

Source: MCDOWELL; UTTAMLAL; GRAHAM (2016).

However, the solution studied also had the addition of crude oil as well. Figure 6 shows how MEG concentration can interfere with the signal's amplitude of the mixture. The study also points out that UV-Vis and blue lights could have been used, but they decided not to use them. The reason is that the presence of aromatic hydrocarbons in crude oil causes inconvenient amplitude responses with these light sources. Therefore, they opted to use a light source greater than 500 nm to avoid this problem.

Despite the success of the above study presented, there can be noticed a missed opportunity. As it can be seen in figure 3, between the red light and green light, there are the yellow and orange ones. As the yellow stands between both green and red waves, and also factoring in the existence the commercial application of the yellow LED in measuring ethylene glycol, there is an investigation worth doing with this LED colour (HANNA INSTRUMENTS, 2022).

The second study is about the utilization of Fourier Transformed Near-

Infrared Spectroscopy (FT-NIR) and UV spectroscopy techniques in order to determine THIs (MeOH and MEG) and a KHI (poly(N-vinylcaprolactam) or PVCap) respectivaley. All of this was measured with salt (NaCl) as well.

Figure 6 - Amplitude responses to the solutions with different levels of MEG

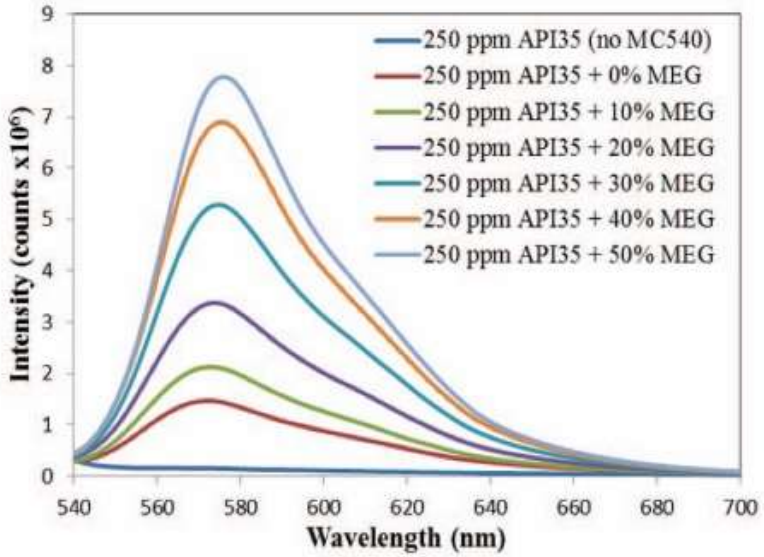

Source: MCDOWELL; UTTAMLAL; GRAHAM (2016).

Figure 7 presents the measures of pure water, MEG and MeOH separately that were extracted with the use of the FT-NIR. The sensor used was a FT-NIR spectrometer from Arcoptix with HL-2000-FHSA light source from Ocean Optics. As it is illustrated, the measures are quite distinct from each other.

In figure 8, however, all the sample mixtures follow the same standard presented by the deionized water in figure 7. The maximum amount of THIs used was 60% mass (HAGHI; YANG; TOHIDI, 2018). It serves to demonstrate that the water has a prevalent overtone when compared to the other substances.

At the end of the study, the authors got a successful result measuring MEG with salt and with PVCap. The best standard error of prediction (SEP) for MEG with NaCl was 0.142 and for MEG with PVCap and NaCl was 0.215 mass% (HAGHI; YANG; TOHIDI, 2018). This was achieved within the wavelengths of 1400 and 1850 nm (HAGHI; YANG; TOHIDI, 2018). The authors also got excellent results between 1400 nm and 1600 nm. Ranges larger than 1850 nm were not considered as the absorption of water was way too high (HAGHI; YANG; TOHIDI, 2018). This hindered the predictions of the THIs as several errors were added with the inclusion of this range (HAGHI; YANG; TOHIDI, 2018).

Figure 7 - Amplitude's responses of deionized water, MEG and MeOH with FT-NIR

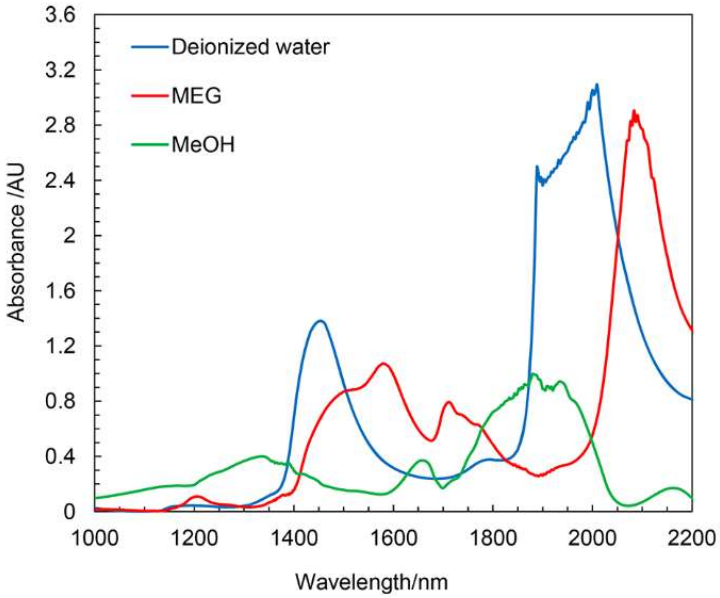

Source: HAGHI; YANG; TOHIDI (2018).

Figure 8 - FT-NIR amplitude responses of 50 water samples, with different levels of MEG and MeOH and salt

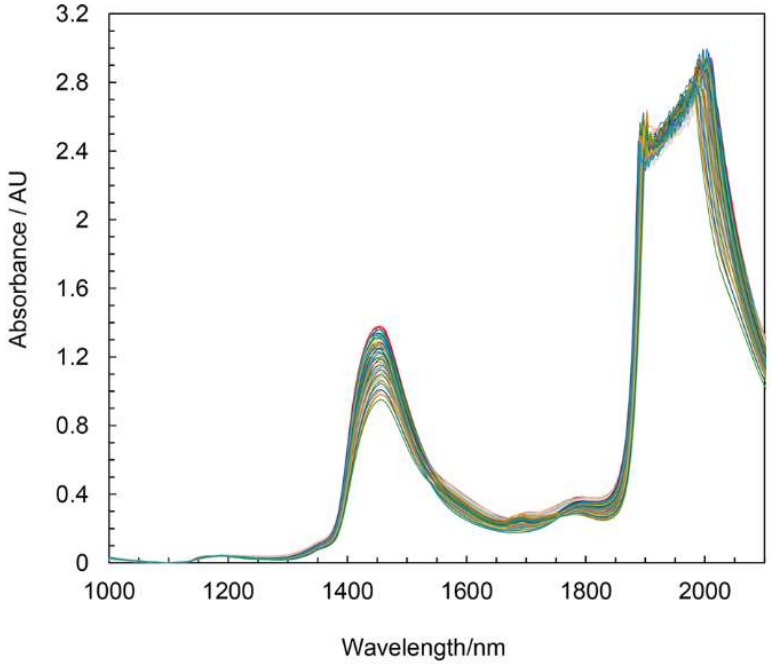

Source: HAGHI; YANG; TOHIDI (2018).

The third study investigated MEG compostion through the principles of Nuclear Magnetic Resonance (NMR) in the context of its reclamation and regeneration in subsea systems of natural gas extraction. The samples were comprised of MEG (20 up to 80 wt%), methyl diethanolamine (1 up to 10 wt%), acetic acid (1 up to 5 wt%), NaCl (4 wt%) and deionised water (SHILLIDAY et al.,

2022). The equipment used was a Spinsolve 43 MHz benchtop NMR spectrometer from Magritek.

The work concluded that it is possible to measure MEG concentrations with up to 1 wt% accuracy (SHILLIDAY et al., 2022). This surpassed FTIR techniques (5%) and sensors based on Velocity and Conductivity (2 up to 3 wt%) (SANDENGEN; KAASA, 2006; SHOUKAT; BAUMEISTER; KNUUTILA, 2019). Furthermore, it also achieved the same level of accuracy as Gas Chromatography (1 wt%) with imputities (MOKHTARI; POURABDOLLAH, 2012).

3 MATERIALS AND METHODS

This section covers everything that was essential in order to attain the results. As experiments were being performed, new materials and methods were being introduced. The materials were: a spectrophotometer, two chambers, a filter, a microcontroller, a personal computer, glass flasks, acrylic tubes, MEG (coloured and colourless), tap water, a decade box (resistors), LEDs, a symmetrical digital power supply, a suction pear and pippetes. The methods were the programming to extract and process data, used both in the Arduino and MATLAB, respectively. The electrical schematic, chamber mechanical design, and the main source codes can be accessed in a GitHub repository (BALDIN, 2023).

3.1 Hamamatsu C12880 MA sensor

In order to collect spectral features, a Hamamatsu C12880MA spectrometer and its breakout board (figure 9) were implemented. The spectrometer has many technical features, such as (ATTACHMENT 1):

a) fingertip size: 20.1 × 12.5 × 10.1 mm;
b) weight: 5 g;
c) spectral response range: 340 to 850 nm;
d) high sensitivity;
e) spectral resolution: 15 nm max;
f) supports synchronized integration;
g) hermetic package: high reliability against humidity;
h) integration with mobile measurement equipment available.

Figure 10 shows the spectrometer's pins. Each one of them has the following meaning (ATTACHMENT 1):

1) sensor power supply: 5 V (input);
2) sensor ground;
3) sensor power supply: 5 V (input);
4) sensor clock pulse (input);

5) case connection;
6) sensor start pulse (input);
7) Pulse for capturing sensor video signals (output);
8) fastening pin (it does not connect electrically);
9) sensor scan end (output);
10) sensor video output.

Figure 9 - Hamamatsu C12880MA spectrometer and breakout board

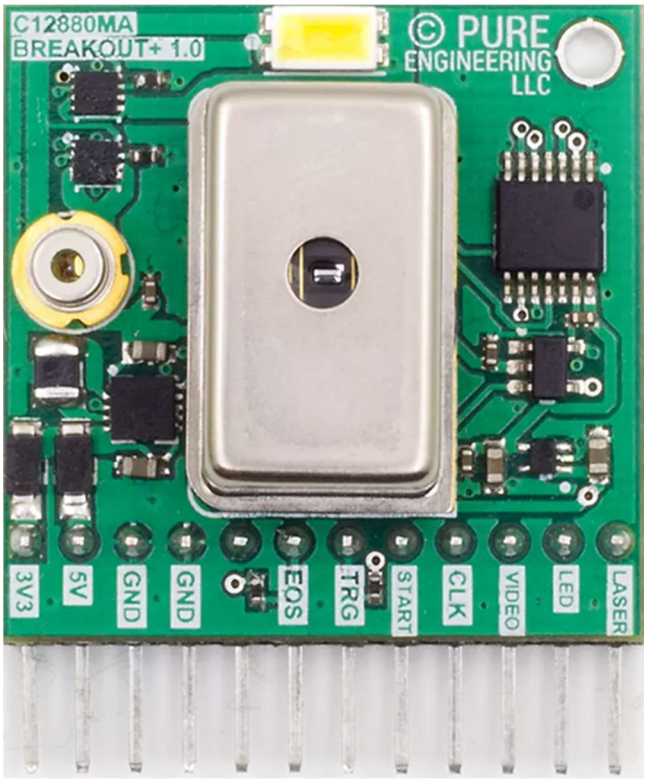

Source: HAMAMATSU (2018).

Figure 11 shows how the pins presented in figure 9 are connected to the microcontroller used in this project (Arduino Uno R3). The analogical signals captured by the sensor pass through the analogical sockets in the Arduino, where the analogue-to-digital conversion happens.

The Hamamatsu C12880MA spectrometer is considered a compact sensor, which is different from a benchtop spectrometer. Contrary to what is shown in figure 4, it has its own collimator, monochromator and detector embedded within the sensor. Figure 12 shows how it works inside. The input slit works as a collimator, the reflective concave blazed grating works as a monochromator, and the CMOS sensor is the proper detector.

Figure 10 - Hamamatsu C12880MA pins

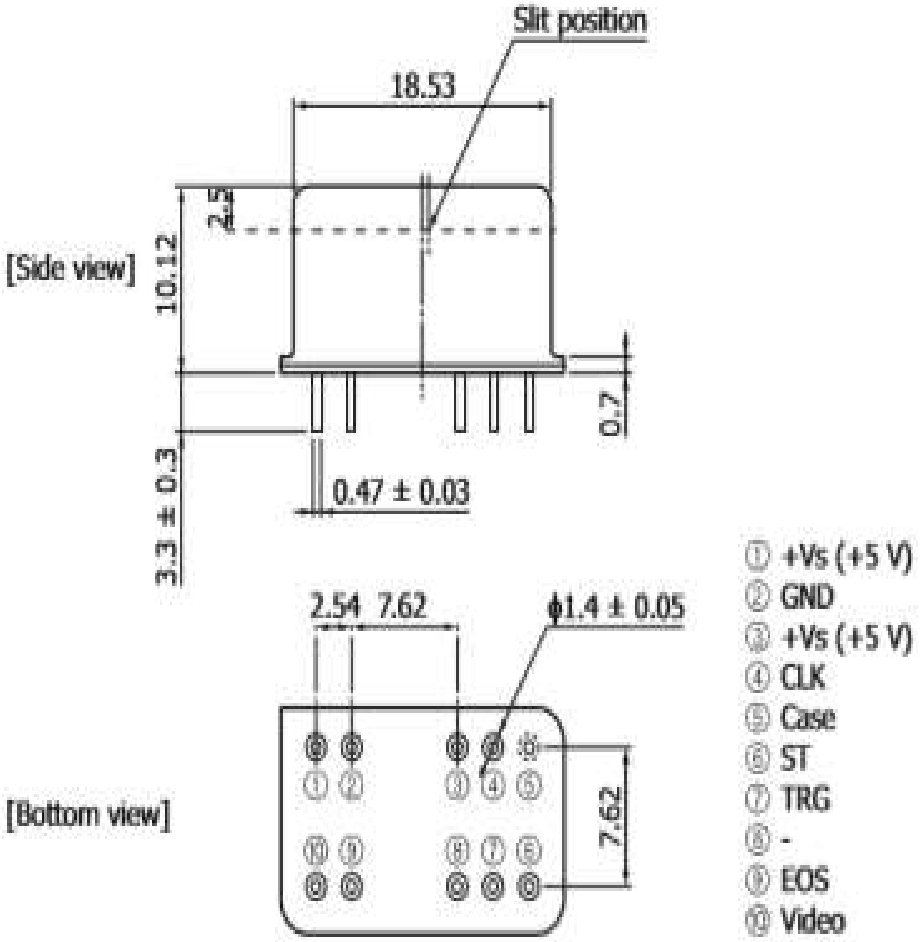

Source: HAMAMATSU (2018).

Figure 11 – pin connection between the spectrometer and the microcontroller

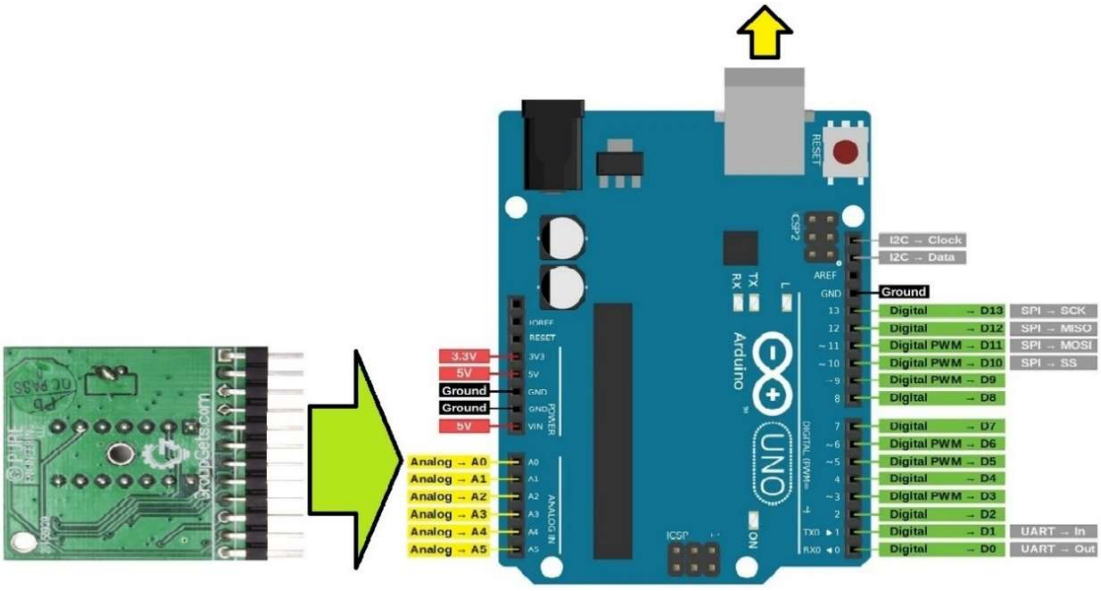

Source: HAMAMATSU, ARDUINO PIN CONFIGURATION- complete guide (2020), own authorship.

Figure 12 – Structure of the monochromatic beam of light reflects on a concaved prism until the detector, which captures the colourful beams

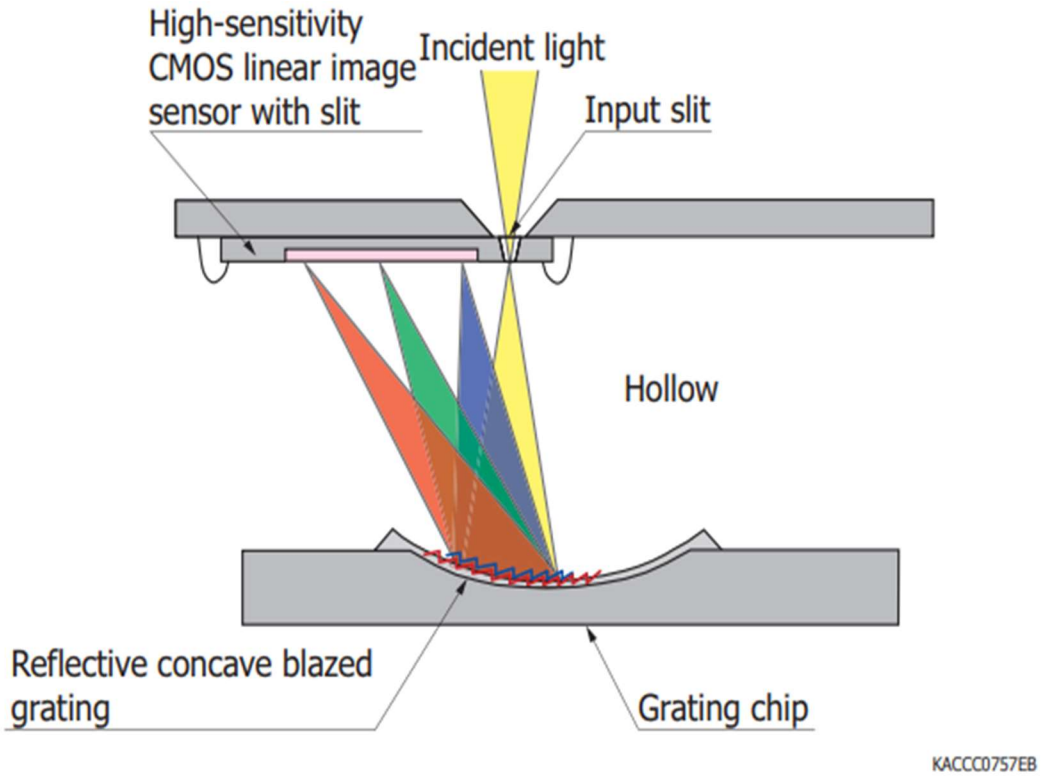

Source: HAMAMATSU (2018).

3.1.1 Main technical features

The Hamamatsu C12880MA spectrometer is part of the MS spectrometer series, thus having many equivalents and comparable technical features (ATTACHMENT 2). This series, along with other spectrometers, is grounded in the MOEMS (Micro-Opto-Electro-Mechanical Systems) technology, which involves capturing and processing optical signals in tiny dimensions by using electrical and mechanical mechanisms (FERREIRA; BALDIN, 2019).

The CMOS (Complementary Metal-Oxide-Semiconductor) is an integrated image sensor widely implemented in electronics and part of the MS series (ATTACHMENT 2). Table 1 shows the main features within this series, with the C12880MA being the only one with high sensitivity. In order for the C12880MA to achieve an elevated signal-noise mensuration, it needs to receive a low level of incident light (ATTACHMENT 2). This also forces the sensor to be placed in a dark place; otherwise, it will suffer with saturation too.

Table 1 - Hamamatsu mini-spectrometers

Parameter	Micro-spectrometer		MS series	Unit
	C12666MA	C12880MA	C11708MA	
Photo				-
Type	Spectrometer head Wide dynamic range	Spectrometer head High sensitivity	Spectrometer head For near IR	-
Spectral response range	340 to 780	340 to 850	640 to 1050	nm
Spectral resolution (FWHM)*1	15 max.		20 max.	nm
Wavelength reproducibility*2	-0.5 to +0.5			mm
Wavelength temperature dependence	-0.1 to +0.1		-0.05 to +0.05	nm/°C
Spectral stray light*1 *3	-25 max.			dB
Dimensions (W × D × H)	20.1 × 12.5 × 10.1		27.6 × 16.8 × 13	mm
Weight	5		9	g
Image sensor	CMOS linear image sensor	High-sensitivity CMOS linear image sensor	CMOS linear image sensor	-
Number of pixels	256	288	256	pixels
Slit (H × V)*4	50 × 750	50 × 500	75 × 750	µm
NA*5	0.22			-
Operating temperature*6	+5 to +50			°C
Storage temperature*6	-20 to +70			°C
Trigger compatible	-			-
Evaluation circuit (sold separately)	C14465-10	C13016	C14465	-

Source: HAMAMATSU (2018).

3.1.2 Sensor adjustment

The sensor was adjusted using a table sheet provided by Hamamatsu (ATTACHMENT 3). Each table is associated with a device serial number. It is a pixel-to-wavelength conversion. Thus, it gets from the first pixel to the 288th pixel and adapts them inside the spectral response, which in the case of Hamamatsu C12880MA is: 340 to 850 nm. Equation 4 shows how the conversion was made (ATTACHMENT 3):

$$Wavelength = a0 + b1 * pix + b2 * pix^{2} + b3 * pix^{3} + b4 * pix^{4} + b5 * pix^{5} \quad (4)$$

Each device serial number comes with its own constants, which are: a0, b1, b2, b3, b4, and b5. In the case of this study, the serial number is 17I00596, with the following constants (ATTACHMENT 3):

- a0 =3.071188765E+02,
- b1 = 2.710355256E+00,

- b2 =-1.368366888E-03,
- b3 = -5.161080308E-06,
- b4 =-1.645262382E-09,
- b5 = 2.137989782E-11.

With this defined, it was found that the resolution begins at 309.8278582 nm, and finishes at 881.9583901 nm. This adjustment in practice only affects how the data is interpreted, as it is a vector containing the correct position of the visible spectrum (figure 3) aligned to the sensor's response.

3.2 System development

The programing was made based in the C language for Arduino together with MATLAB. The spectrometer sensor was attached to the microcontroller as shown in figure 11. There is a sample in front of the sensor, and there is a LED behind it. All this setup was inside a dark chamber. As it received the signals, the microcontroller converted them and sent them to the computer through a USB B connector, as indicated in figure 11. With the help of MATLAB, it was possible to plot curves and analyze the data collected.

3.2.1 Firmware

The former code operated continuously by clock pulses in order to read converted digital signals. It also scanned data with minimal delays between readings.

The new firmware was implemented to act as a state machine with the use of switch case. This was done to save up energy and avoid unintended readings. Figure 13 shows the state machine's flowchart. This system has two states: idle and reading. The idle state is the default state, where literally nothing happens. While the user does not type letter a (which stands for "advance"), the state machine continues to be in the idle state (as a "false" state). The reading state is the state that makes the system work as it is supposed to (thus, it is considered a "true" state). The reading procedure originally consists of doing

analogical reads and printing data with a delay. This printed data was sent to the computer through a serial port, so then it could be viewed by a software like Putty or MATLAB. In order to return to the idle state, the letter r would have to be pressed.

Figure 13 – State machine implemented

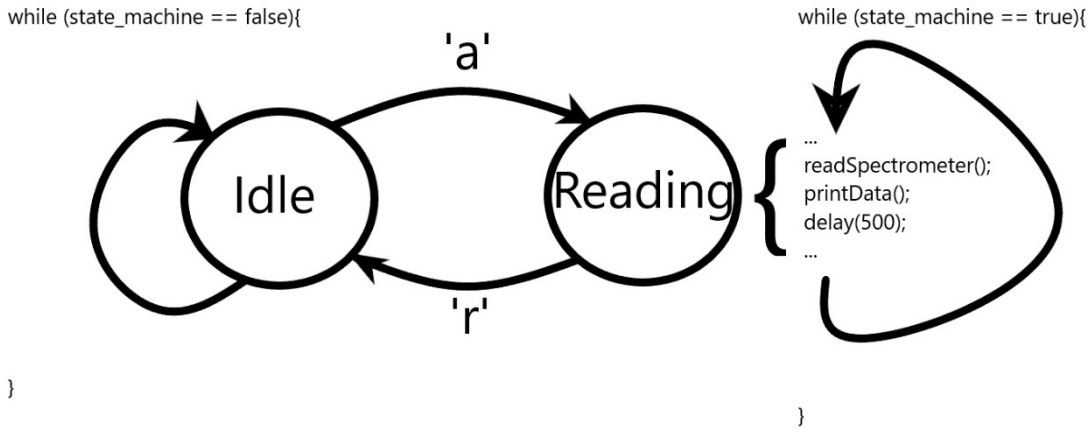

Source: Own authorship (2022).

The delays were set in order to facilitate the visualization of the data sent, as it was being plotted in MATLAB. The speed in which the sensor reads the samples was way too fast in order to observe them properly. Any detail in the plots is worth paying attention to, because often times the difference between samples can be small. By doing so, it was possible to compare the plots visually before doing a multiplot in Excel, for instance, and recalibrate the system somehow by demand.

3.2.2 Data processing

Initally, Putty was used just to show the extracted vectors. These vectors could be copied and pasted in an Excel spreadsheet, where the data could be plotted. This was a very manual (and therefore slow) and tiring data acquisition process.

So in order to solve this issue, a code in MATLAB was implemented. More specifically, MATLAB's App designer tool was utilized to make a Graphical User Interface (GUI). Figure 14 shows the app developed so that it could

accelerate data acquisition.

Figure 14 – Window representing the developed application

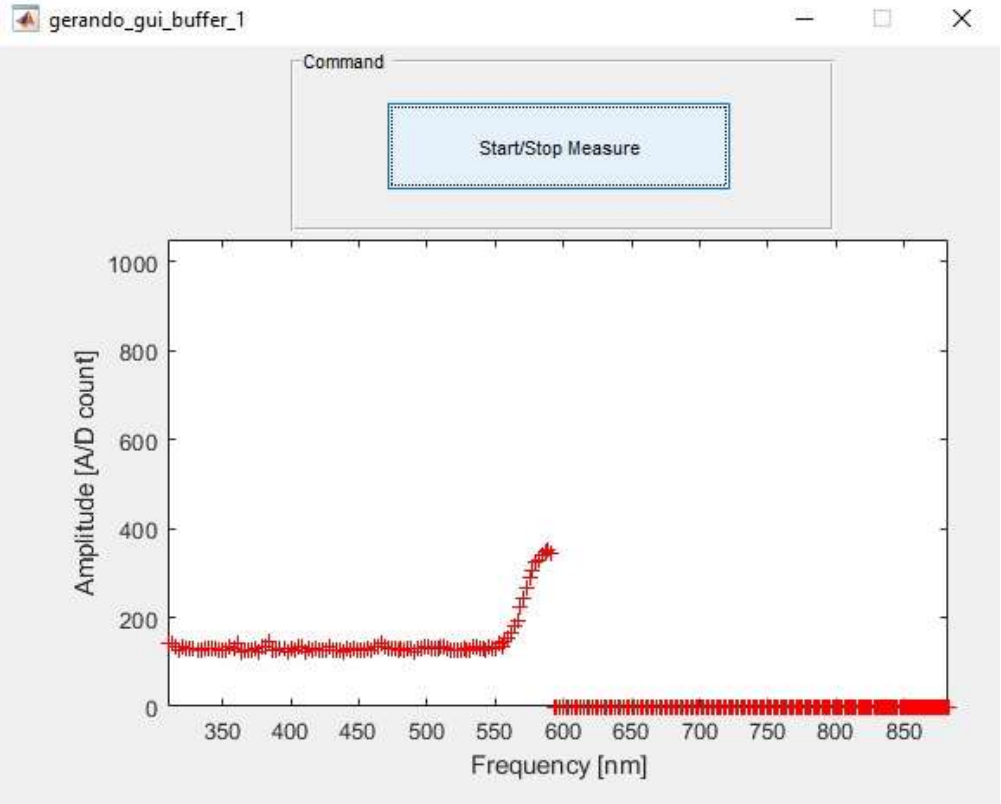

Source: Own authorship (2022).

The application is comprised of a toggle button (where it reads “Start/Stop Measure”) and a graphical area. The toggle button is responsible to operate the state machine within the Arduino. When it is pressed for the first time, it sends the letter a to the microcontroller, changing the machine state to “reading”. When it is pressed again, it sends the letter r, changing the machine state to “idle”. When it is pressed yet again, it restarts the whole process. Thus, this application operates the whole process of data acquisition through serial communication. The graphical area, as expected, is destined to draw the spectrum’s response based on the vectors obtained.

3.3 Dark chamber construction

The chamber is a crucial part of the project. It is necessary for the correct operation of the spectrophotometer, as it covers both the light emitter and the

sensor, thus avoiding environmental light (interference). The following boxes were printed using 3D printers with ABS material.

Two chambers were made: (1) for glass flasks and (2) for small acrylic pipe section (second). The first chamber can be seen in figure 15, printed in black. Black is the colour that absorbs light the most. Thus it was chosen to create an environment with the least amount of light interference.

Figure 15 – Chamber for the glass flasks

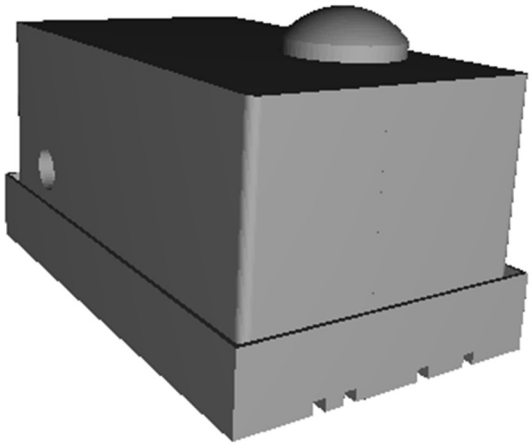

Source: Own authorship (2022).

The interior of the first box can be seen in figure 16, in which each number represents the following:

1. screw opening;
2. LED opening;
3. place where the flask is put;
4. LED jumper openings;
5. platform for the Arduino microcontroller;
6. opening for the USB B connector
7. mini wall by passing the box to fit the cover;
8. fit where the filter is put.

The screw opening was made so then it would be possible to attach a support to that. The LED opening, flask placement, the filter's fit, and the Arduino's platform follow a similar logic to that presented in figure 4. The USB B

connector's hole, along with the Arduino's platform, follows the design adopted in figure 11.

Figure 16 – The interior of the first chamber

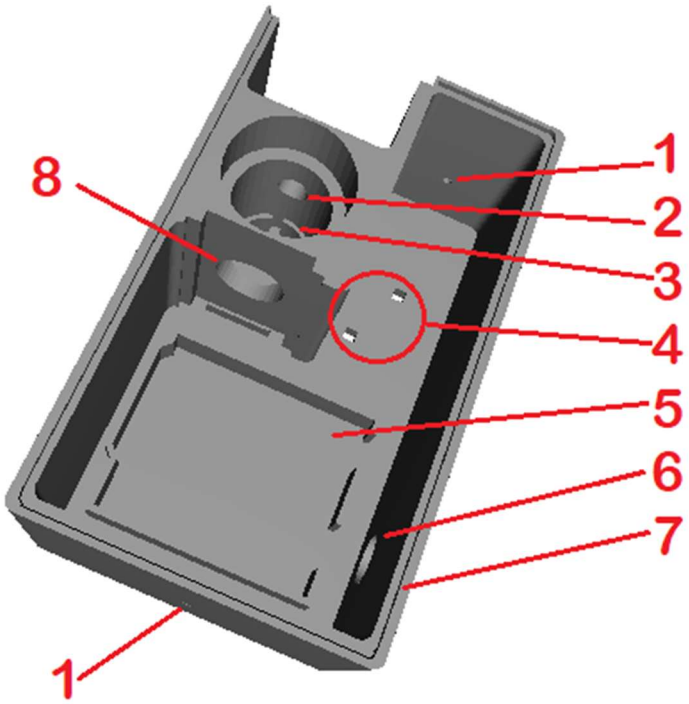

Source: Own authorship (2022).

In figure 17, it shows the other side of the chamber. Each number represents the following:

1. openings for LEDs;
2. LED jumper openings;
3. fit for the frontal LED space.

As seen, there are two positions to place the LEDs: frontal and lateral. The fit for the frontal LED space was used for better manipulation and conditioning of the frontal LED in a tiny space, which was not needed with the lateral LED. Figure 18 displays the hatch used to place in position number 3, image 17.

Similarly to figure 18, the filter's base fit was designed accordingly (image 19). Two pieces were made to fit together in the shape of pins: one male and

another female. This was necessary to hold the circular filter properly so that it could be easily detached. It was fixated in position number 8 of image 16.

Figure 17 – Interior of the first chamber, other side

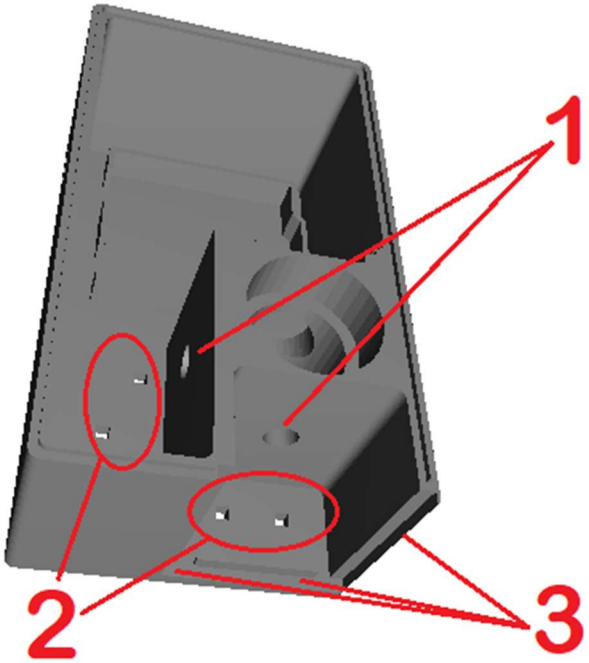

Source: Own authorship (2022).

Figure 18 – Hatch used to close the frontal space LED space

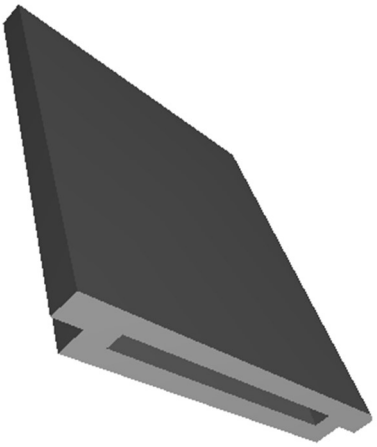

Source: Own authorship (2022).

First, the screw opening presented in figure 16 (position 1) was made to adopt a screw-based support, which was based in two pieces fixated together by

screws (figure 20). This support was created in order for the chamber not to be unstable and not to smash the LED jumpers. The small orifices on top were intended for the insertion of screws, while the jumpers passed by the openings at the bottom.

Figure 19 – Filter fitting parts

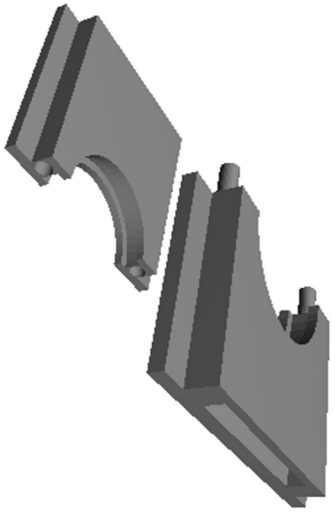

Source: Own authorship (2022).

Another base was made in parallel in the case of the above mentioned base not being satisfactory. This new base has a more simple design with an asymmetrical fit. There are pieces that are meant to be glued together with one above the other. This can be seen in figure 21.

This structure proved to be more reliable than the first one, as it lacks weak spots. The downside would be the fact that it is not strongly attached to the chamber by any means, although it is not a real issue. Therefore, it was used as the default platform.

Another important aspect of the chamber was its cover (figure 22). The slit bypassing it was designed to match the mini walls presented in position 7 in figure 16. However, the fit was not optimal and was very loose. This is probably because of the thread structure that ended up bending the structure. The solution was to screw four bolts, each one in each corner down in the walls, to assure the fixation. However, it was discovered later on that these screws are not necessary to isolate the light and were then taken out.

Figure 20 – screw based support

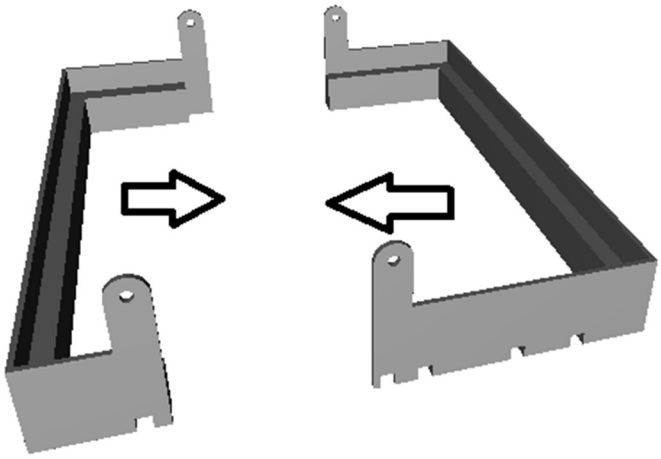

Source: Own authorship (2022).

Figure 21 – Second support

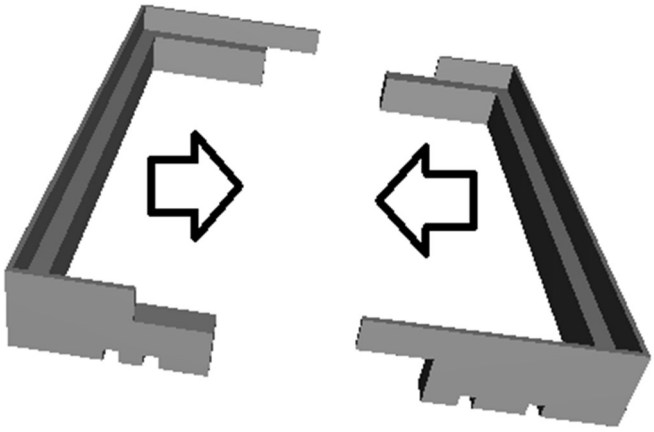

Source: Own authorship (2022).

Finally, the screw cap was made to assure that no light would enter the chamber. The first model can be seen in figure 23. This piece is threaded inside the chamber's cover.

Later on, to facilitate the threading, it was adopted another screw cap with a larger area for the fingers, especially to accommodate the thumb. This piece can be seen in figure 24. It is also worth noting that this new screw cap has less revolutions, which speed up the threading process with no light entering the chamber.

The second box was made based on the first one, and it was designed for flasks made of acrylic. The main differences are that the newest one (figure 25) does not have space for lateral LED, and it has a fit for easier removal and placement of the microcontroller (similar to number 3 from image 17).

Figure 22 – Chamber's cover

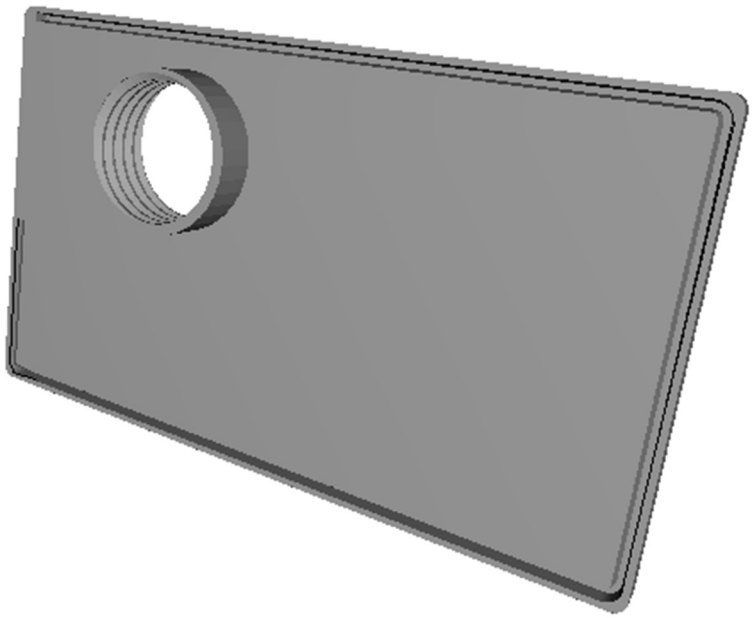

Source: Own authorship (2022).

Figure 23 – Chamber's screw cap

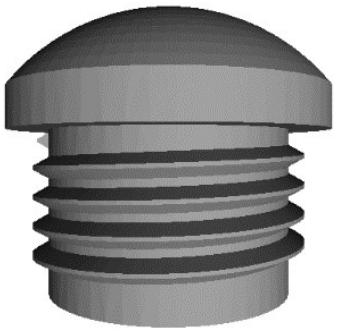

Source: Own authorship (2022).

The second box is also shorter and has a larger area for the flask slot (slightly bigger than 1 inch thick). Other differences are that LED opening is narrower, the cover and the screw cap are different as well.

Figure 24 – The new screw cap

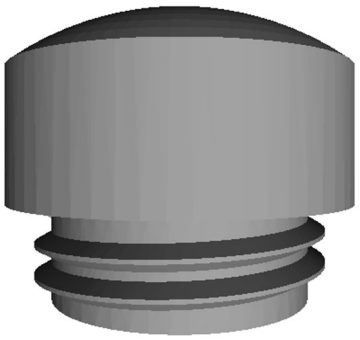

Source: Own authorship (2022).

Figure 25 – Interior of the second chamber

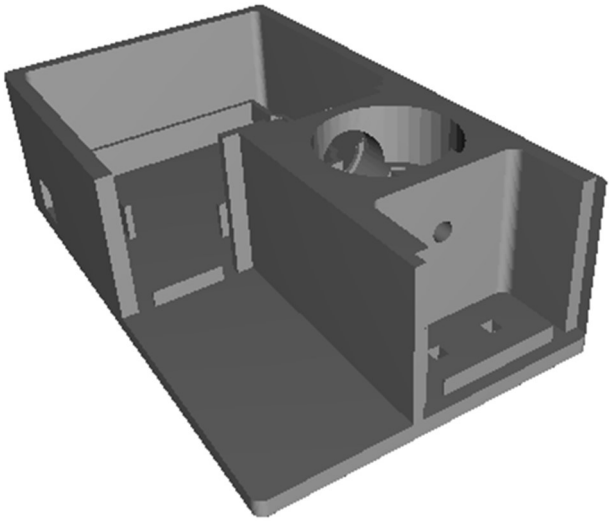

Source: Own authorship (2022).

The new cover follows the chamber's design at the top and it has a new mechanism to attach to it (figure 26). This mechanism consists in short walls (internal and external) clamping the chamber's walls. It is very loose, but it is satisfactory enough. The thread structure was shortened not to go out of its bounds, with the idea of avoiding the bending problem in the previous cover.

The new screw cap is bigger than its predecessor, has thinner walls (figure 27), and fewer revolutions (figure 28). These last two design features were chosen to accelerate the printing process and threading procedure. However, later on these were discovered to be mistakes because they made the screw

thread so fragile, to the point of ultimately breaking it. This was not a critical issue though, since it could be substituted by a tape roll for lateral covering.

Figure 26 – New cover for the new chamber

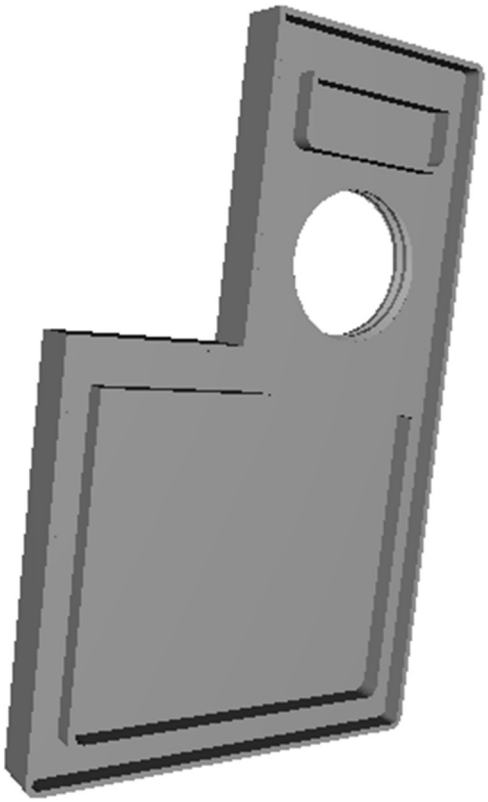

Source: Own authorship (2022).

Figure 27 – Wall differences, with the new cap on the right

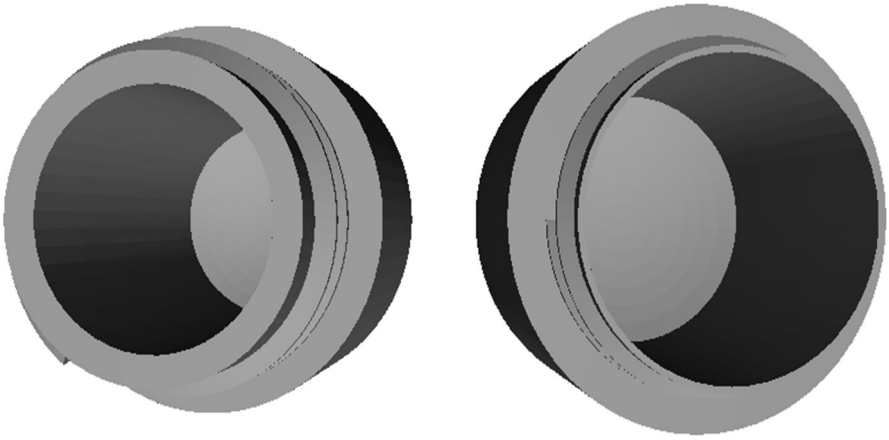

Source: Own authorship (2022).

Figure 28 – Revolution differences, with the new cap on the right

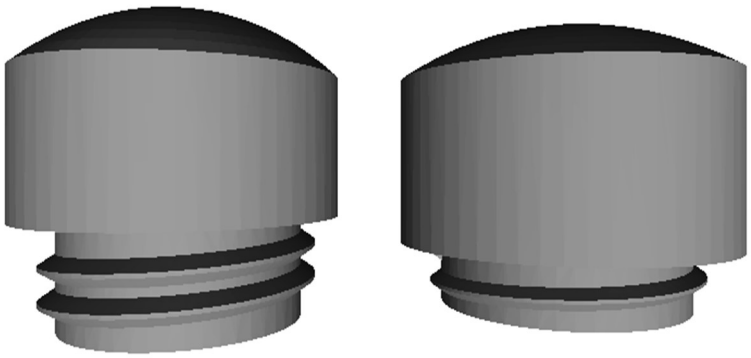

Source: Own authorship (2022).

3.4 LEDs and the circuit

The circuitry involving the LEDs can be seen in figure 29. It is comprised of a resistor from a decade box and a diode to deliver the sensor's necessary light. A controllable source of 5 V and 1 A (maximum current) was implemented, while the resistance was varied in order to alter the brightness. The resistance R, as indicated in figure 29, was modified as much as the decade box allowed (range 1 Ω to 5 MΩ) to deliver a light bright enough not to saturate the signal's amplitude. Otherwise, data would be lost in the process.

Figure 29 – Circuitry for the LED

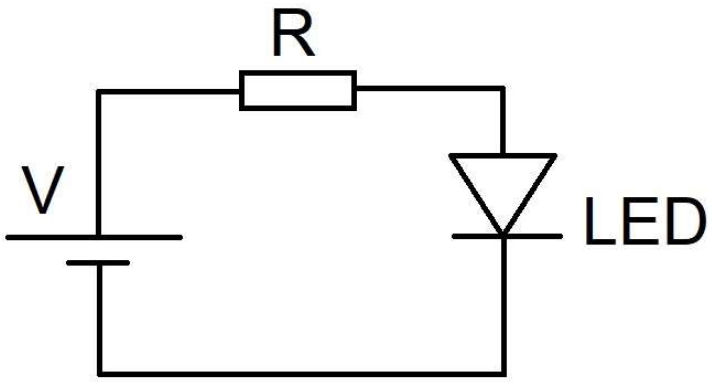

Source: Own authorship (2022).

Considering the first study presented in this work, the LEDs used in the

experiments were: UV, blue, green, yellow, and red. UV and blue were mentioned as possible light sources, while the green and red were used in the laser form. As the yellow falls between red and green spectrums, adding to the fact that there is a commercial application with it, it was considered as well.

3.5 Samples

In this study, MEG was mixed with a reddish dye called aniline (0.2 g/L) to make it visible. Then, it was mixed with water as it is miscible in it. This mixture is very homogenous, thus making the final liquid very uniform and reliable to measure. This mixture was made with a suction pear and pippetes.

The samples that were utilized can be divided in four categories: with and without reddish dye, and within glass flasks and acrylic ones. In figures 30 and 31, the glass (around 20 mL) and acrylic (around 18 mL) flasks containing dyed MEG can be seen, respectively.

As it can be seen in both figures 30 and 31, the samples were: 0% (tap water), 10%, 25%, 50%, 75%, 90%, 94%, 97%, and 100% of MEG with dye.

There were also some samples made with pure colorless MEG. Figure 32 shows these samples. However, there was no need for the 94% and 97% samples of colourless MEG, and the reason for that is explained in the results.

Figure 30 – Glass flasks with dyed MEG

Source: Own authorship (2022).

Figure 31 – Acrylic flasks with dyed MEG

Source: Own authorship (2022).

Figure 32 – Glass flasks with pure MEG (from 0% to 100% of MEG)

Source: Own authorship (2022).

3.6 Filter

The filter used in this work is a lens for the sensor from ThorLabs. As it is presented in the results section, LEDs do not respond well without the lens, especially the UV and blue ones. The lens can be seen in the image 33.

Its primary purpose was to eliminate saturated and residual fluorescence in wavelengths below 570 nm that was detected in initial tests. It also helped to shape curves in some LEDs so that the curves would vary both in amplitude and in the wavelengths of the maximum peaks instead of just amplitude. However,

with other LEDs, it did not change anything significantly further than centering peak positions on reddish wavelengths.

Figure 33 – The reddish filter

Source: THORLABS (2022).

4 EXPERIMENTS

The experiments were conducted following the following parameters:

- with and without lens;
- with and without dye;
- the frontal and lateral position of the LED;
- periods of the day (morning, afternoon and evening);
- LED colour.

The resistance from the decade box was always set in order to place signals peaks around half of the maximum amplitude. Thus, saturation could be avoided accordingly.

The chamber designed for the glass flasks (figure 15) was the one used the most. Unlike those made of glass, Acrylic flasks had visibly much more scratches and (colorless) stains on their surfaces, as they were homemade out of acrylic tubes and plates previously used in other projects. This led to the hypothesis that the glass ones were much more reliable. As the experiments were validated for the glass flasks, then they were tested with the acrylic flasks.

5 RESULTS AND DISCUSSION

This section is mainly divided in two parts by the LEDs colors, as their colours were the most decisive factor in the results presented.

The first part is about the spectral response of the LEDs within different configurations, as mentioned in the experiments section. Figure 34 is a reference to better assess the results as it is a complement to figure 3. The graphics presented in figure 34 were taken by measures of the spectrophotometer with an empty chamber. Despite the fact that the yellow LED presented an orange response, it will be treated as yellow because that is a commercially standard low cost yellow LED that looks yellow when it is off.

The second part is about the processed data based on the spectral response. These results are divided as following: each LED has a chart with the mean of three batteries of measurement (or more), a chart for maximum peak evolution (as the MEG concentration rises), and a chart for wavelength shifts between each maximum peaks (similar to figure 5). In order to make a fair and objective comparison, the selected configurations are those measured in the afternoon, with lens, and with dyed MEG.

Figure 34 – Visible spectrum in detail

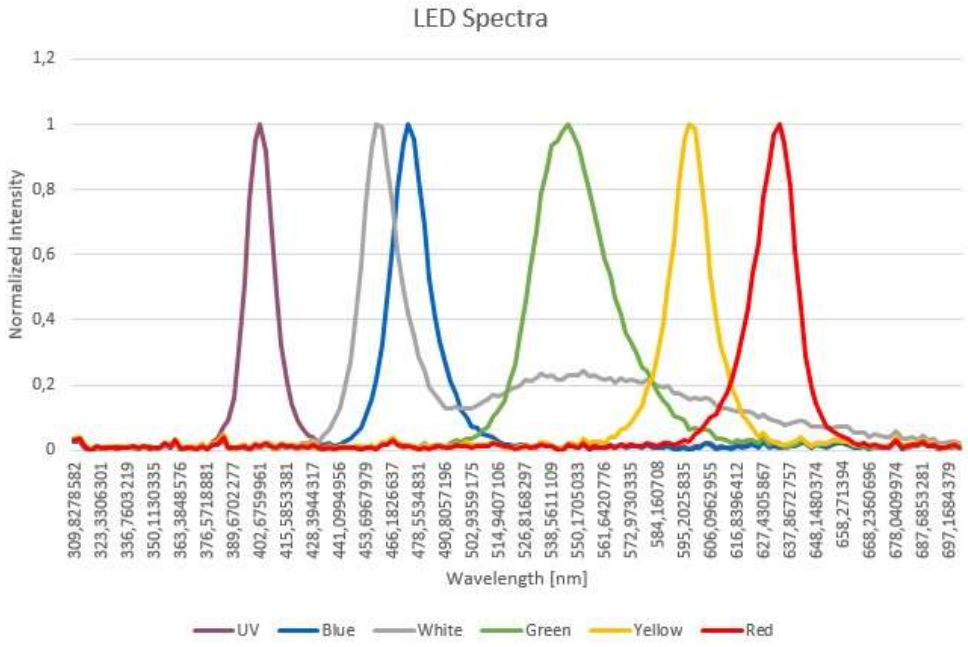

Source: Own authorship (2022).

5.1 Filter validation

In order to justify the use of the lens, measures were made to evaluate how beneficial they were for the UV LED. At first, of course, the necessity of them was unknown. When the samples were measured without dye, it was just a matter of resistance until the signal's intensity did not saturate, and it was also straightforward. With dye, however, there was always an inconvenient fluorescence in the of the UV wavelengths that was higher than the sample's fluorescence in reddish wavelengths. This made the analysis of curves peaks and their wavelengths quite unreliable. Figure 35 represents this case with a couple of measures made without lens with the UV. The ordinate axis represents the signal's intensity (A/D count), while the abscissa axis represent the wavelength (nm). It was measured with 4000 Ω. It can be noted that in this extreme case, just increasing the resistance does not allow a better assessment of the samples in addition to saturating (losing data of) the spectral response.

With the use of filter, the problems above mentioned vanished. Figure 36 illustrates that. In this case, it was measured with 1000 Ω. Considering that it did not saturate even with a lower resistance, it makes clear that the filter was efficient at solving the problem of residual fluorescence.

Figure 35 – UV response without filter

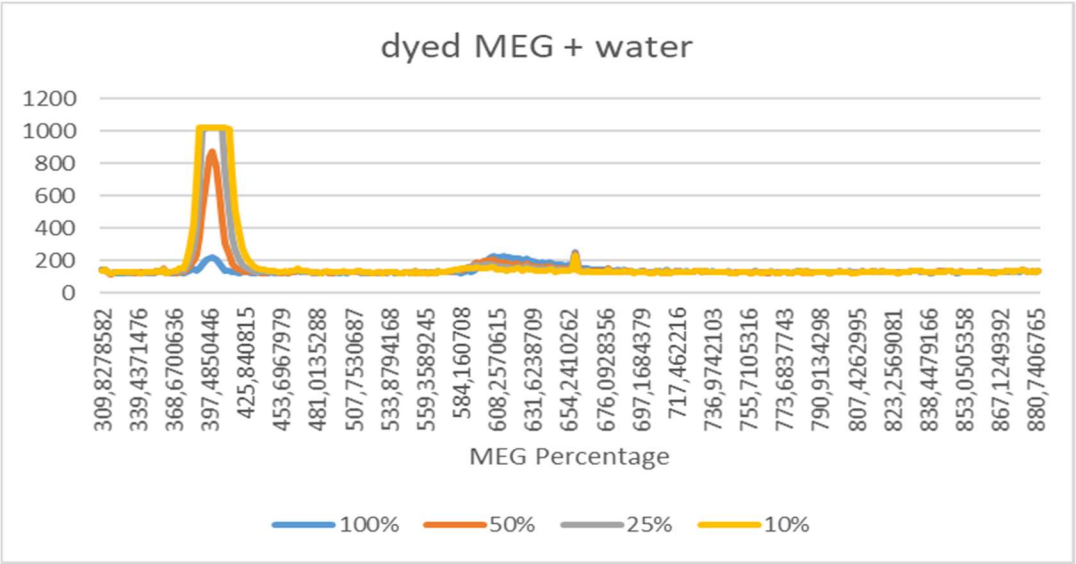

Source: Own authorship (2022).

Figure 36 – UV response with filter

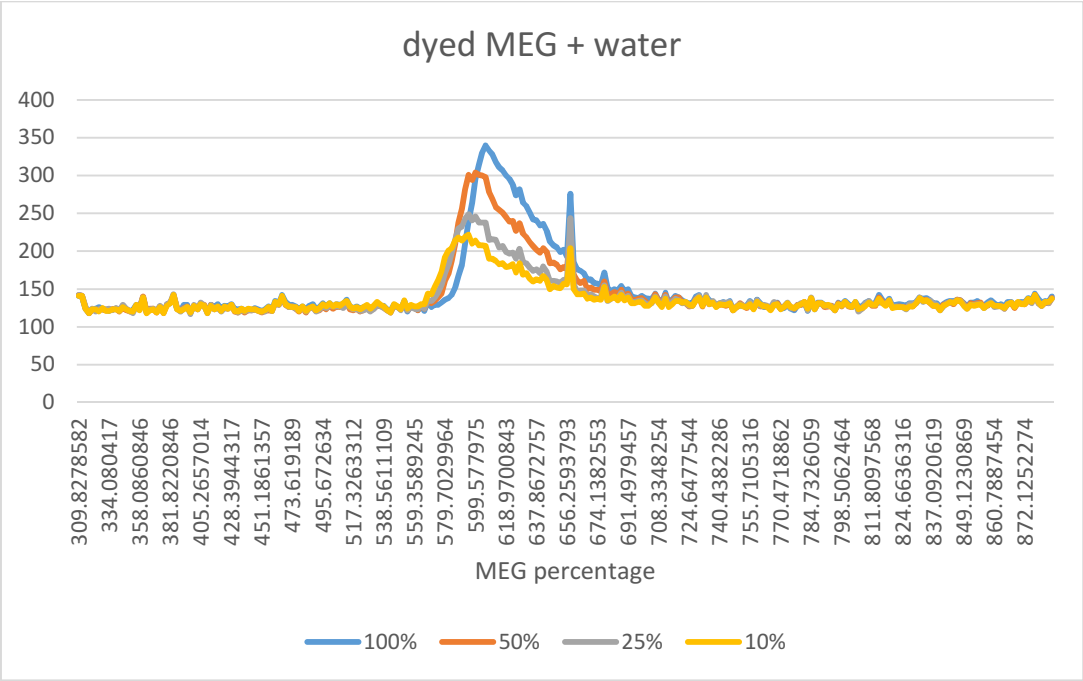

Source: Own authorship (2022).

5.2 UV LED and its spectrum

Table 2 shows the configurations used for the UV LED with the minimal amount of batteries made.

Table 2 - Experiments configurations for the UV LED

Number:	Filter:	LED's position:	Day period:	Resistance:	Number of batteries:
10	yes	frontal	morning	15k ohms	3
22	yes	frontal	afternoon	15k ohms	3
23	yes	lateral	afternoon	3,5k ohms	3
34	yes	frontal	evening	15k ohms	3
46	yes	frontal	morning	20k ohms	3
58	yes	frontal	afternoon	20k ohms	3
70	yes	frontal	evening	20k ohms	1
106	no	frontal	afternoon	1,5M ohms	1
130	no	frontal	evening	2M ohms	1

Source: Own authorship (2022).

The ultra-violet LED results in the purple curve in figure 34. 28 measures were made within 13 configurations on total. One of the measures made is

configuration 106 (figure 37), which used pure MEG in the samples. It consists in not using the filter, frontal position, measured in the afternoon, and used 1.5M Ω. This configuration was numbered the 106. The wave's peaks are around the wavelength 400 nm, which means that the experiment was successful in representing the wave colour (despite the fact that the peak could have been at a lower wavelength). However, as it can be seen, this configuration does not allow a conclusive assessment of the amount of MEG. Therefore, it was necessary to use the lens to change this.

In figure 38, it is presented a chart of this sort. The configuration used is as it follows: with filter, frontal position (LED), measured in the afternoon and used 25k Ω (in the case of colourless MEG). It was numbered condition 22.

Unfortunately, as it can be seen, it did not distinguish very well, with 90% sample being below the water sample while 100% sample standing at the top above all. Inconsistencies like this could be seen throughout most conditions for the colorless MEG. Most of the results behaved in the same manner with this type of MEG, especially without filter. Still, most of them had the curve shape the same as in figure 37.

Figure 37 – Curve samples without dye measured with the configuration 106

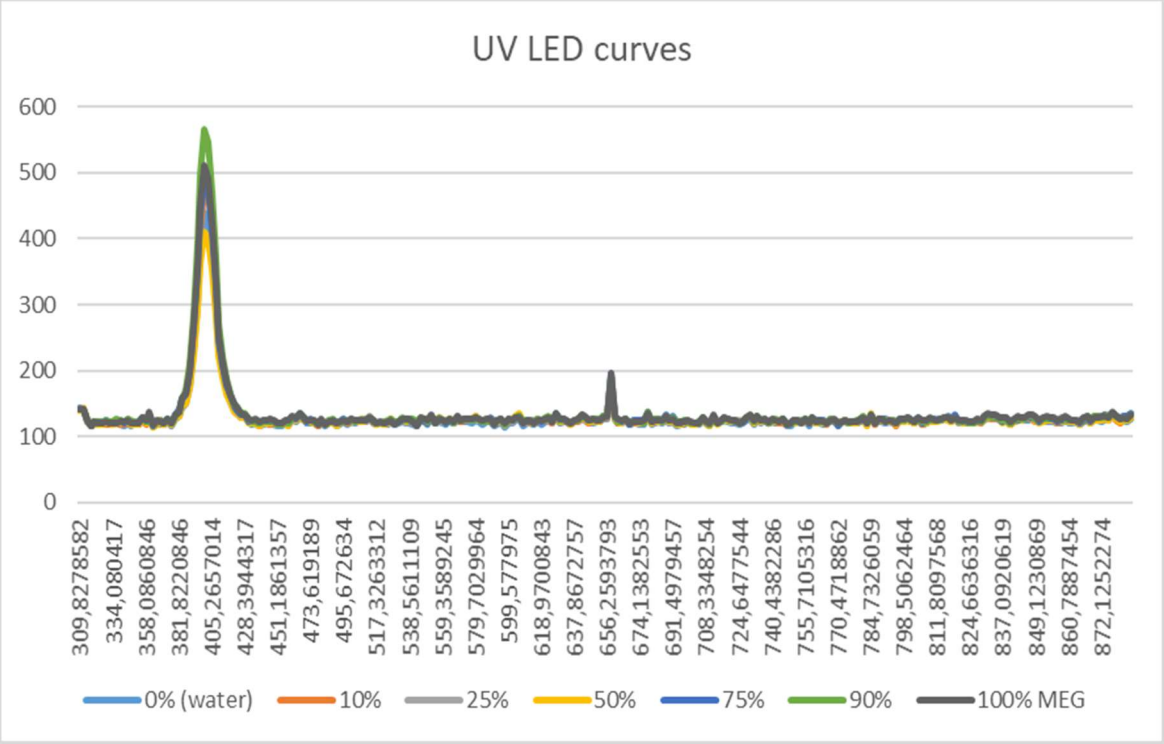

Source: Own authorship (2022).

Figure 39 shows the following characteristics: with filter, frontal position, at night with 15k Ω. It was numbered configuration 34, and it shows a much more interesting behavior compared to configuration 106, as now it is possible to understand the trend of the curves as the concentration of MEG increases. This condition can be considered a standard for this LED colour. It can be noted on the chart that as its concentration rises, the peaks grow and move more closely to the right. This is natural, as the reddish dye intensifies along with the MEG concentration. The curves come closer to wavelengths around the peak of red (600 nm to 650 nm as seen in figure 34).

Despite being a better result, there is still a problem. In spite of the increase in the peaks along with the concentration, after 90%, the peaks start to decrease in amplitude. This is worrisome, as it was not expected and thus presents a challenge to assess the data. As it will be presented later on, this strange behaviour repeats itself through out other LEDs. This is the reason why samples of 94% and 97% were selected. Thus, this behaviour could be traced properly.

Figure 38 – Curve samples without dye measured with the configuration 22

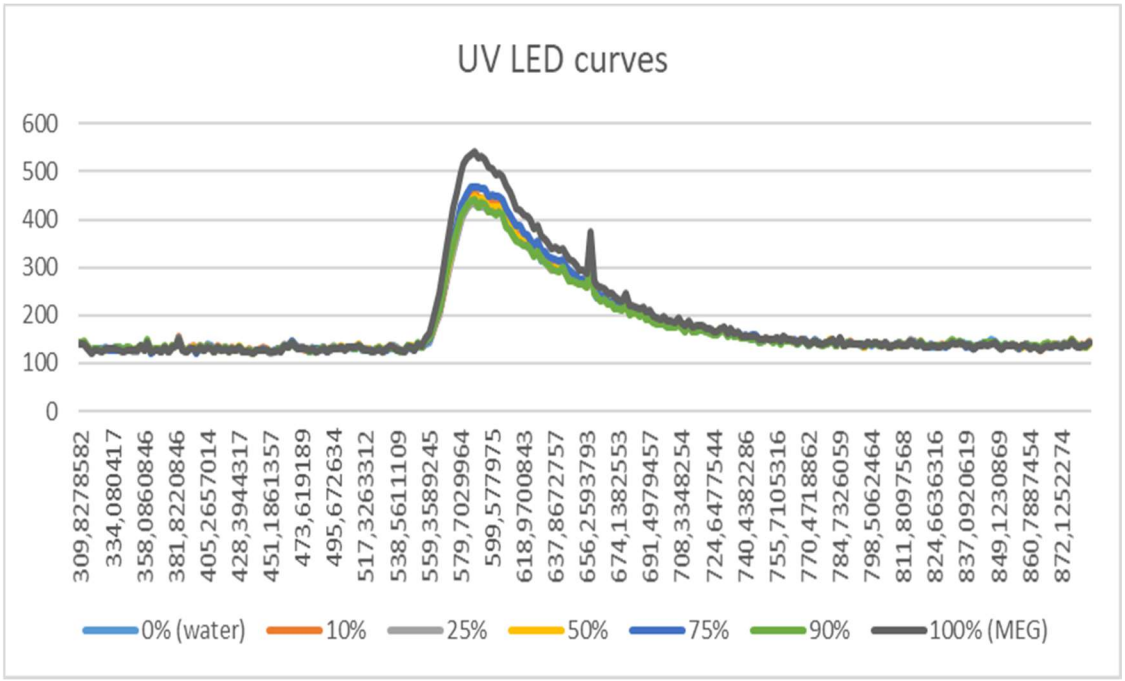

Source: Own authorship (2022)

Figure 39 – Curve samples with dye measured with configuration 34

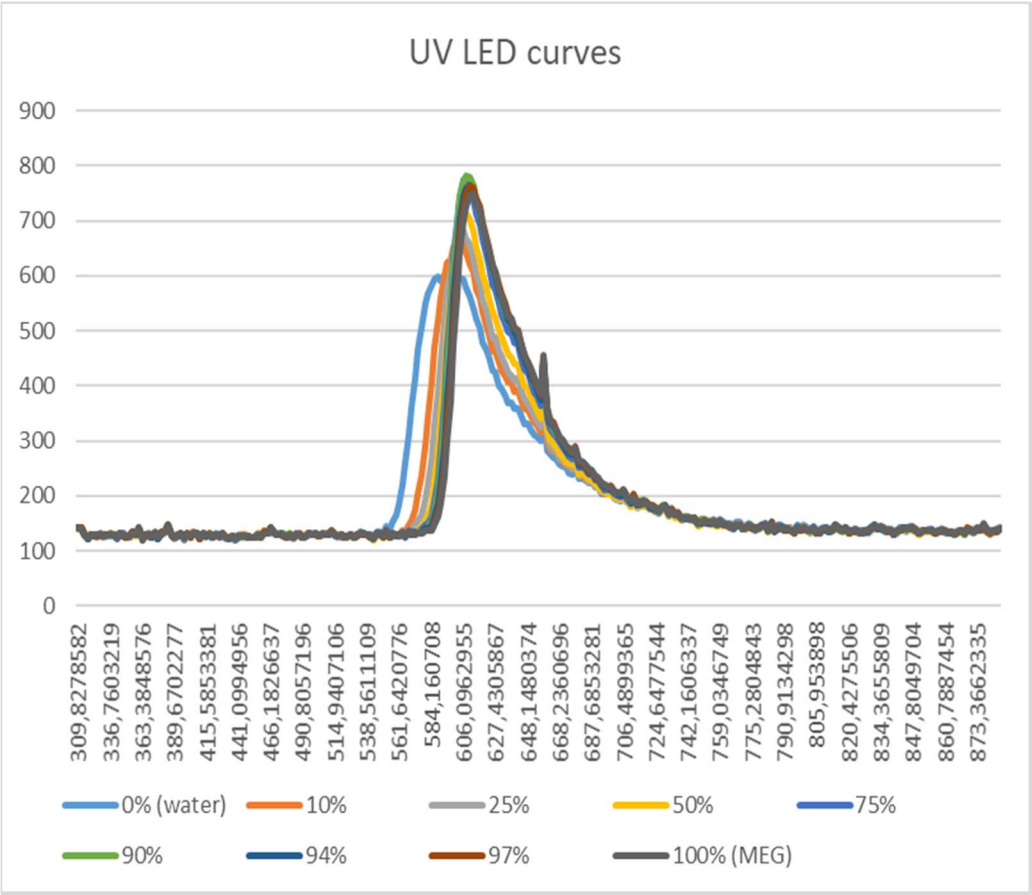

Source: Own authorship (2022).

5.3 Blue LED and its spectrum

Table 3 shows the configurations used with the minimal amount of batteries made.

Table 3 - Experiments configurations for the blue LED

Number:	Filter:	LED's position:	Day period:	Resistance:	Number of batteries:
145	yes	frontal	morning	40k ohms	3
157	yes	frontal	afternoon	40k ohms	3
158	yes	lateral	afternoon	7k ohms	3
163	no	frontal	afternoon	5M ohms	1
164	no	lateral	afternoon	7k ohms	3
169	yes	frontal	evening	40k ohms	3
172	yes	frontal	evening	60k ohms	3

Source: Own authorship (2022).

The blue LED has a very similar behaviour when compared to the UV. The blue LED results in the blue curve in figure 34. 29 measures were made within 9 configurations on total. One of the measures made is configuration 163 (figure 40), which used dyed MEG in the samples. It consists in not using the filter, using frontal position, at night with 5M Ω. The water wave's peak is around the wavelength 476 nm, which means that the experiment was successful in representing the wave colour. However, As it can be seen, this configuration does not allow a conclusive assessment of the amount of MEG above the 50%. As the liquid becomes redder, its overtone diminishes and does not go anywhere in the spectrum. This exactly effect happened to a very similar configuration but with the UV LED. Therefore, it was necessary to use the lens to change this.

Figures 41 and 42 present similar conditions to the condition 163, except that both used the lens to get to the results and each one used 40k Ω and 7k Ω respectively. They were numbered 157 and 158, respectively. Another major difference between them is that the former's LED position is frontal while in the latter it is lateral. As it can be observed, condition number 157 has a better resolution for isolating the 75% of MEG from other curves. This means that the frontal configuration is superior, at least in this case.

Figure 40 – Configuration 163

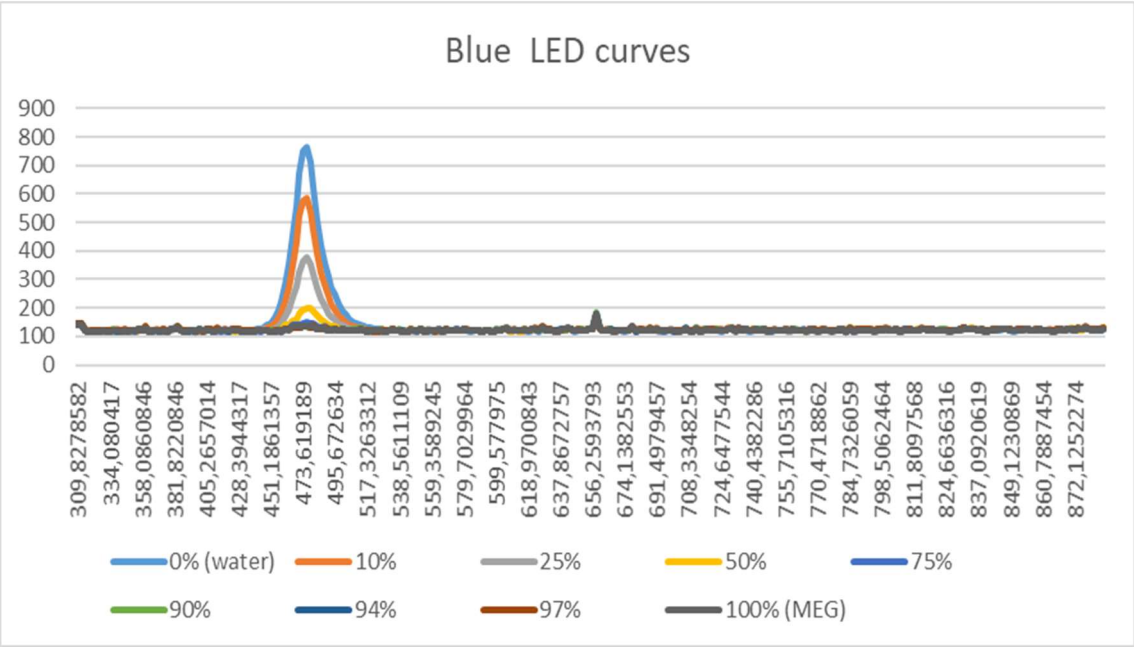

Source: Own authorship (2022).

Figure 41 – Configuration 157

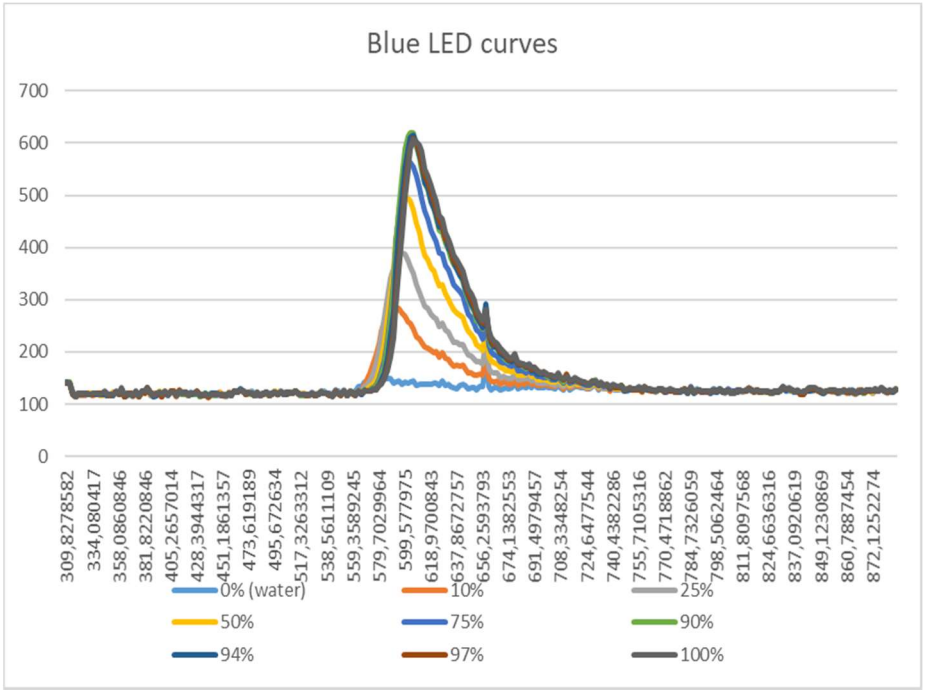

Source: Own authorship (2022).

Figure 42 – Configuration 158

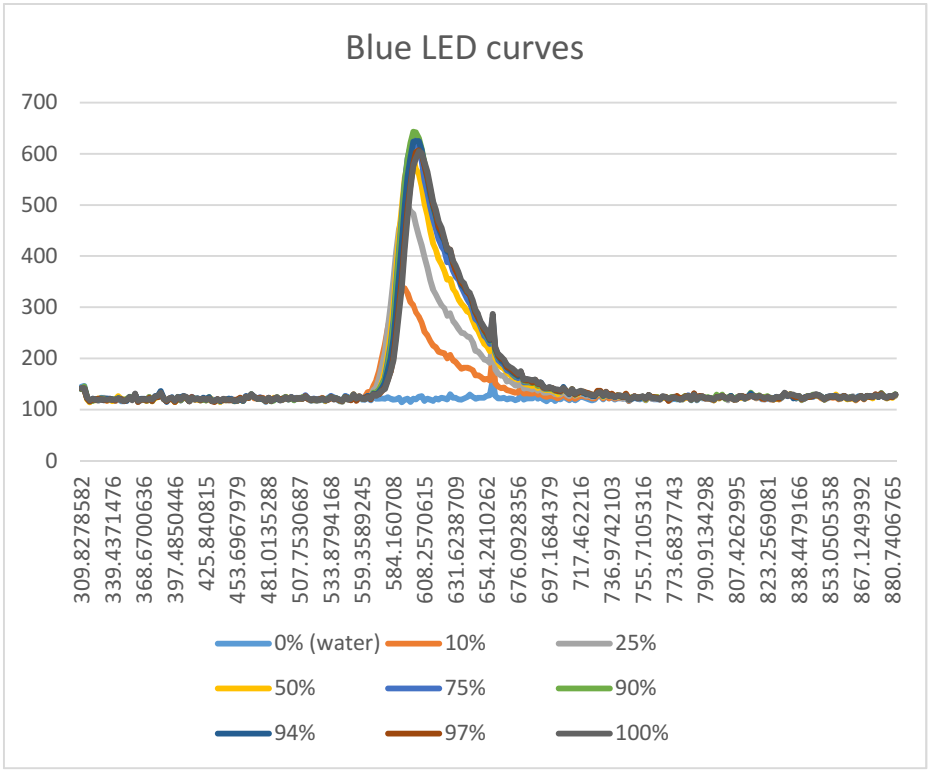

Source: Own authorship (2022).

All in all, the curves presented with the blue LED as the exciter prove to be very similar to that of the UV. The major difference is that water does not fluoresce well with the blue LED.

5.4 Green LED and its spectrum

Table 4 shows the configurations used for the green LED with the minimal amount of batteries made.

The green LED results in the green curve in figure 34. 18 measures were made within 6 configurations on total. One of the measures made is configuration 103 (figure 43). It consists in: not using the filter, not using dye, frontal position (LED), in the afternoon with 5M Ω. Although the peaks lean more towards 545 nm, which means that the experiment was successful in representing the wave colour. However, as it can be seen, this configuration does not allow any conclusive assessment of the amount of MEG. Therefore, it was necessary to use the lens to change this more than any other LED. Even with dye the results were not satisfactory. In some cases with dye, the curves could be distinguished up until 50% of MEG, while in other cases only water had an overtone effect (colourless MEG).

Table 4 - Experiments configurations for the green LED

Number:	Filter:	LED's position:	Day period:	Resistance:	Number of batteries:
7	yes	frontal	morning	800k ohms	3
19	yes	frontal	afternoon	800k ohms	3
20	yes	lateral	afternoon	35k ohms	1
31	yes	frontal	evening	800k ohms	3
55	yes	frontal	afternoon	1M ohms	3
67	yes	frontal	evening	1M ohms	1
80	no	lateral	morning	30k ohms	3
103	no	frontal	afternoon	5M ohms	1
104	no	lateral	afternoon	30k ohms	3
115	no	frontal	afternoon	4M ohms	1

Source: Own authorship (2022).

After applying the filter and dye, the results enhanced greatly. Configuration 7 (figure 44) shows a standard situation where both the filter and dye were applied. This also consists in frontal LED position and it was measured in the morning with 800k Ω. Despite looking much better, the green LED still presents inconsistencies that made it worse than the previous LEDs.

Figure 43 – Configuration 103

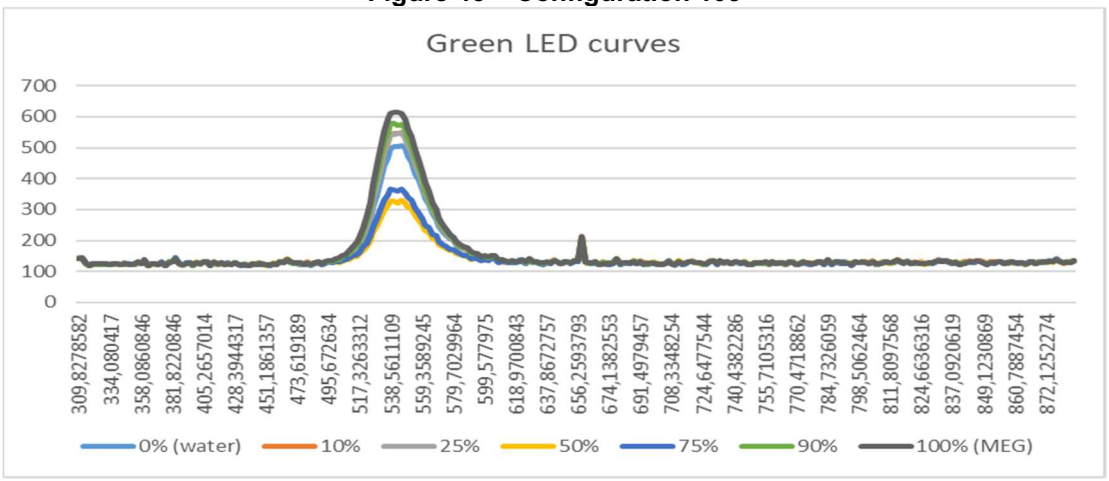

Source: Own authorship (2022)

Figure 44 – Configuration 7

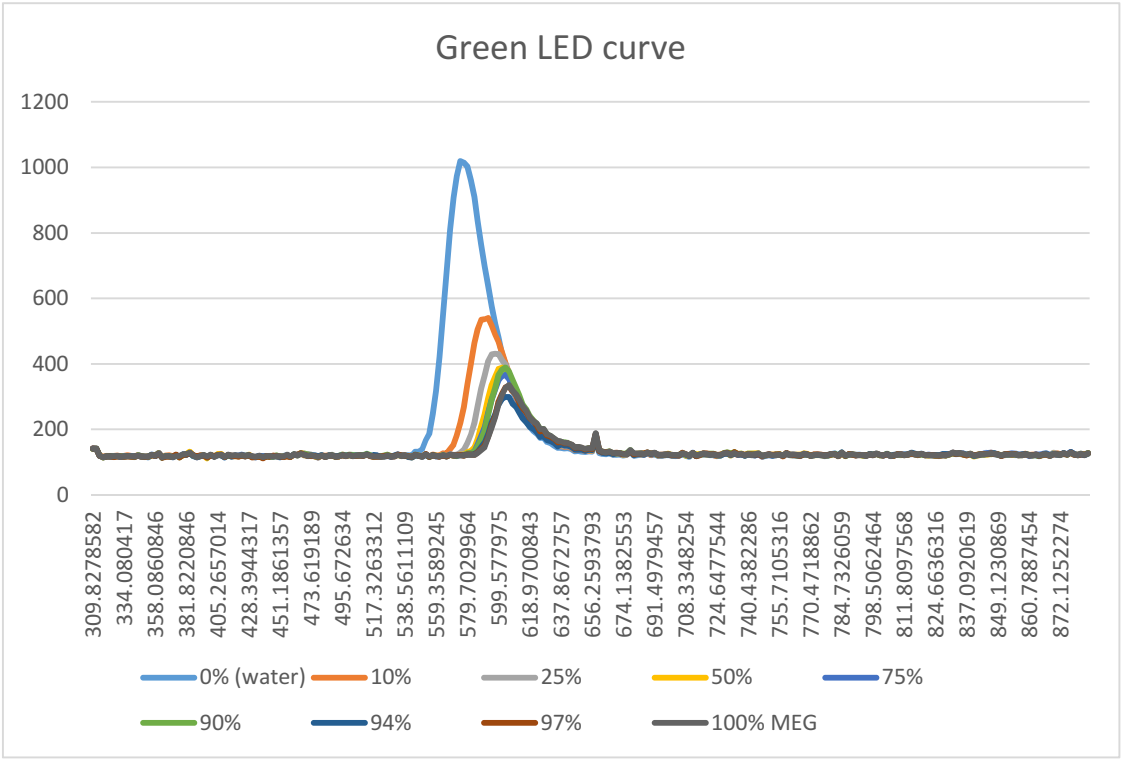

Source: Own authorship (2022).

The greatest peak value belongs to the water and as the concentration of MEG grows, the peaks should always get smaller. However, in this case, the 90% curve managed to get higher than the 75%, while the smallest one was the 94% curve. This is type of inconsistency was very common through the experiments, especially with the 90% curve.

5.5 Yellow LED and its spectrum

Table 5 shows the configurations used for the yellow LED with the minimal amount of batteries made.

Table 5 - Experiments configurations for the yellow LED

Number:	Filter:	LED's position:	Day period:	Resistance:	Number of batteries:
181	yes	frontal	morning	15k ohms	3
187	no	frontal	morning	15k ohms	3
188	no	lateral	morning	1K ohms	1
193	yes	frontal	afternoon	15k ohms	3
199	no	frontal	afternoon	15k ohms	3
200	no	lateral	afternoon	100 ohms	3
205	yes	frontal	evening	15k ohms	3
211	no	frontal	evening	40k ohms	3
212	no	lateral	evening	100 ohms	3

Source: Own authorship (2022).

The yellow LED results in the “yellow” curve presented in figure 34. Around 120 measures were made within around 20 configurations on total. Configuration 199 was one of the measures made with pure MEG, and it can be seen in figure 45. It consists in not using filter, frontal position, in the afternoon with 15k Ω. The peaks are around 588 nm, which means that the experiment was successful in representing the wave colour. As it can be seen, this configuration allows a conclusive assessment about the amount of MEG, contrary to the other LEDs so far. The chart shows that there is an increase in the peaks height as the

concentration rises. It was not necessary to use the lens to change the overtone presented, even though there were many experiments in which it was utilised.

Because of the first measure being a successful one, many other configurations were tested. The lens was used most of the time to allow a better comparison with the other LEDs. Configuration 211 (figure 46) shows an example of an excellent result which looks very similar to what was shown for the green LED in figure 44. Configuration 211 is similar to configuration 199, except that it was measured at night, with 40k ohms, and with coloured MEG.

Figure 46 presents a standard measure for the yellow LED. Except for lateral configurations where the curves would appear in the similar way to the blue curves, but in a very disarrayed way. Because of the success of the measures taken with the glass flasks, there were some measures taken with the acrylic flasks. The results were similar to those shown in figure 46.

Figure 45 - Configuration 199

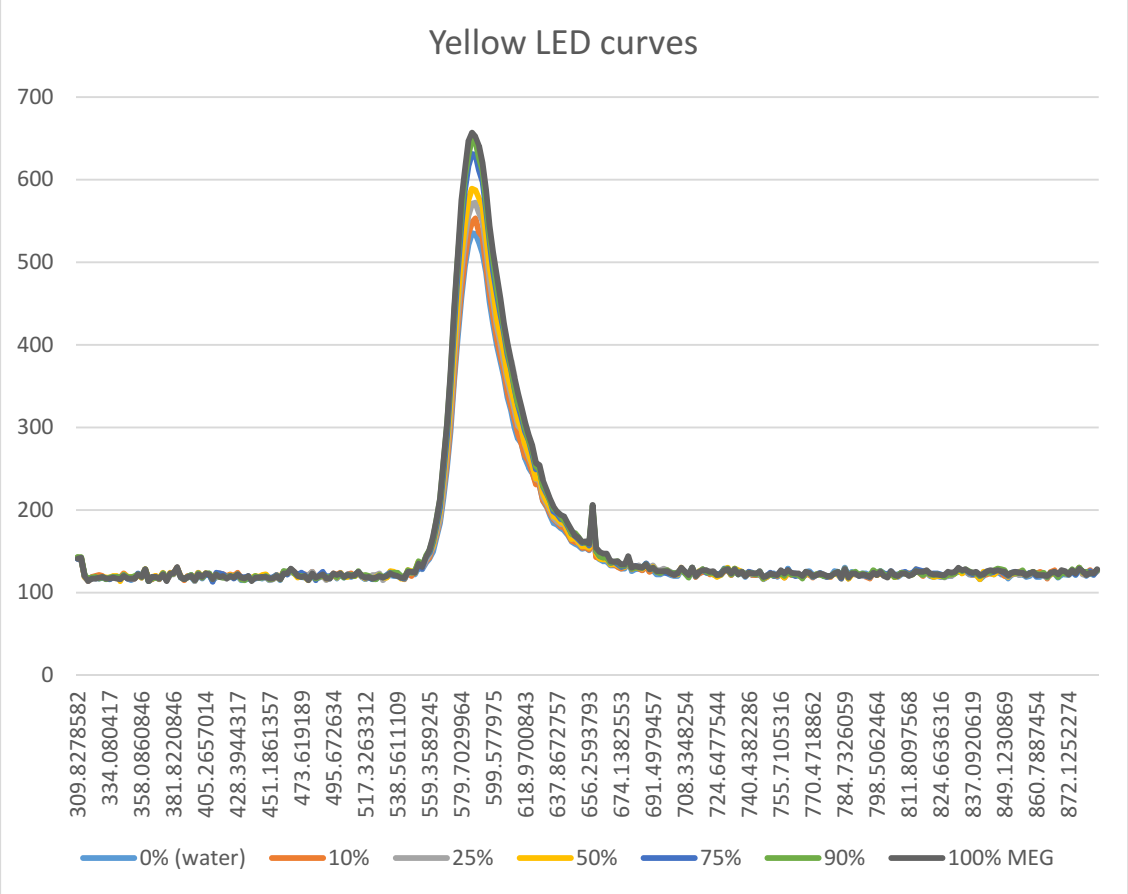

Source: Own authorship (2022).

Figure 46 – Configuration 211

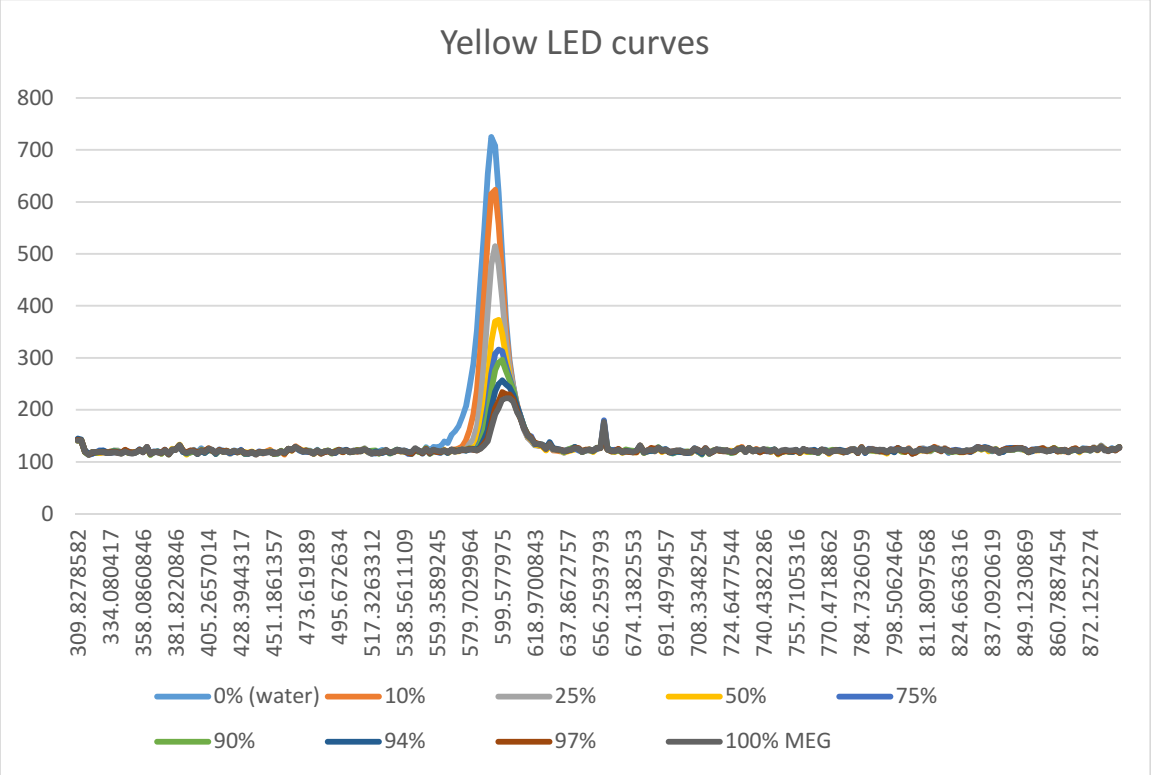

Source: Own authorship (2022).

5.6 Red LED and its spectrum

Table 6 shows the configurations used for the red LED with the minimal amount of batteries made.

Table 6 - Experiments configurations for the red LED

Number:	Filter:	LED's position:	Day period:	Resistance:	Number of batteries:
16	yes	frontal	afternoon	900k ohms	3
17	yes	lateral	afternoon	600 ohms	1
28	yes	frontal	evening	900k ohms	1
52	yes	frontal	afternoon	1,2M ohms	3
64	yes	frontal	evening	1,2M ohms	1
100	no	frontal	afternoon	900k ohms	1
101	no	lateral	afternoon	15k ohms	1

Source: Own authorship (2022).

The red LED results in the red curve in figure 34. Around 11 measures were made within around 6 configurations on total. Configuration 100 is one of the measures made that can be seen in figure 47, in which the percentages refer to the amount MEG in the samples. It did not use a filter, the samples had dye, the LED was in a frontal position, the resistance used was 900k Ω, and it was extracted in the afternoon. The wave's peaks are around the wavelength 631.62 nm, which indicates that the experiment was successful in representing the wave colour. However, this colour does not present a fully progressive logic in the peaks, despite growing steadily up until 90%.

Other configurations were extremely similar in form, regardless of the use of filter or dye. They mostly varied in amplitude and they had a much less logical progression. However, figure 48 shows condition 17, with a smaller difference in the spectrum, but still lacking a clear and logical trend in its peaks. This configuration is similar to that of 100, but it was measured laterally, with the filter on, and with just 600 Ω. It can be seen that around waves 579.70 and 612.56 nm, there was a reflectance of the waves with yellowish and orange tones that showed some kind of logical growth. There could be some sort of area integration in this region to discover the MEG concentration. It would require more measures with similar conditions in order to validate a meaningful trend though.

Figure 47 – Configuration 100

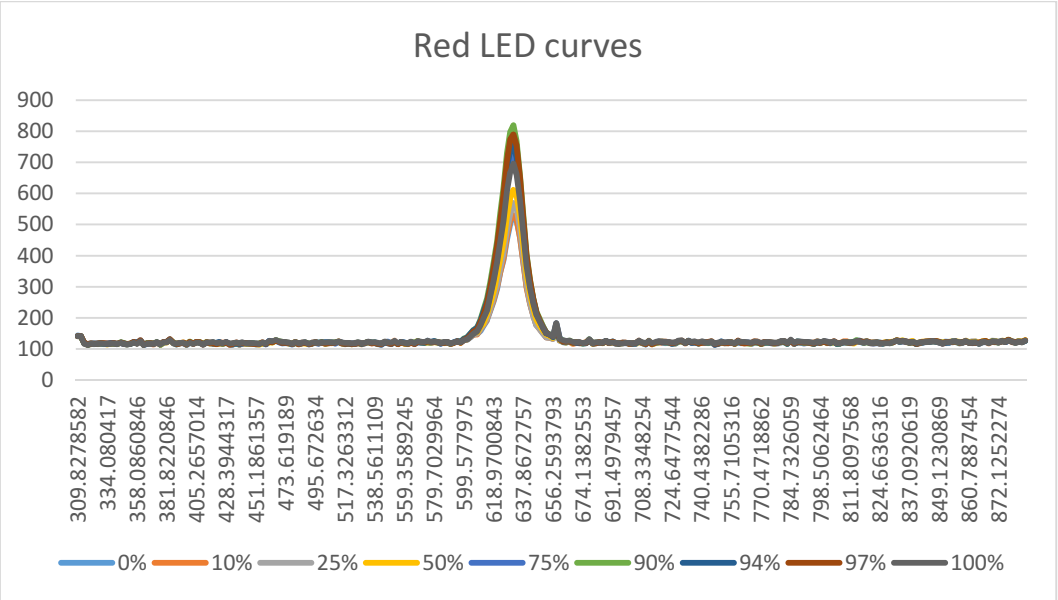

Source: Own authorship (2022).

Overall, since the dye was the same colour as the LED and the filter, there was no variation in the wavelengths, making it the most predictable and least meaningful experiment.

Figure 48 – Configuration 17

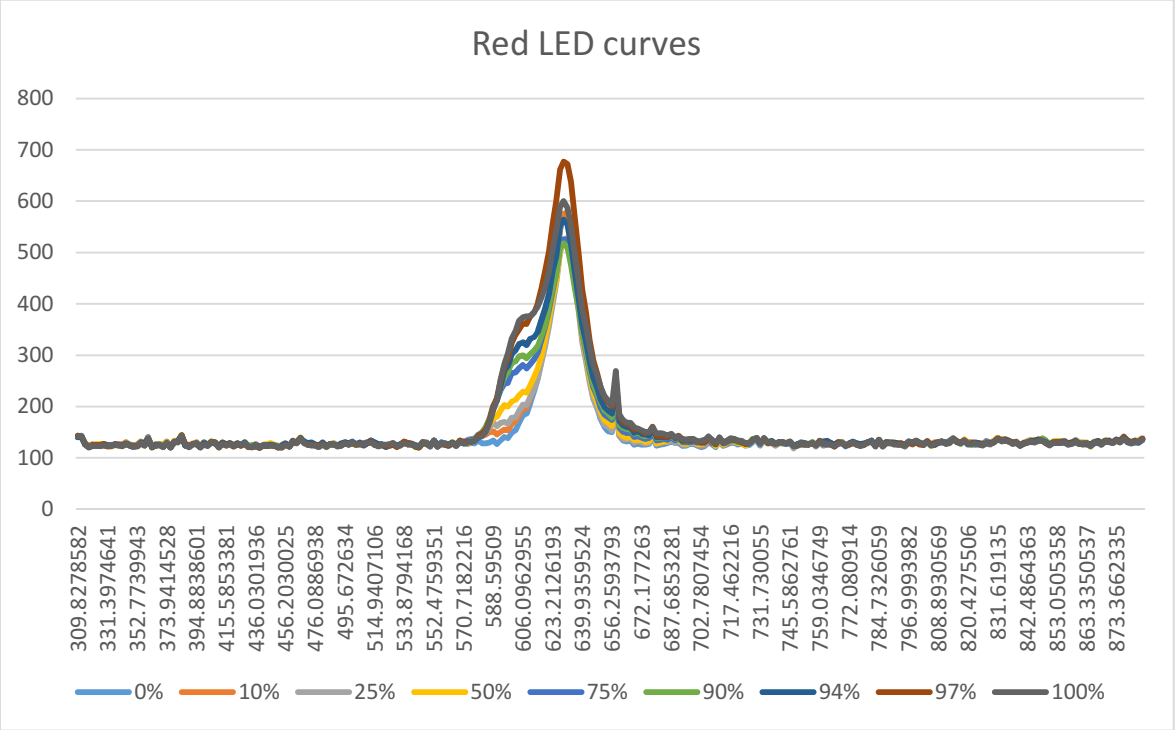

Source: Own authorship (2022).

5.7 UV LED and processed data

In figure 49, there can be seen the fluorescence for the UV LED. As expected, as the solution becomes redder, it shifts to the right towards the red light's fluorescence. After 90%, it goes down a little bit, making this excitation method far from predictable around this point.

The second chart presented in figure 50 shows how the curves maximum peaks have an exponencial progression. Something worth noting is that the amplitude has a very low standard deviation, with largest one being 0.0229 (at 10% of MEG).

Figure 49– Configuration 22 and its curves

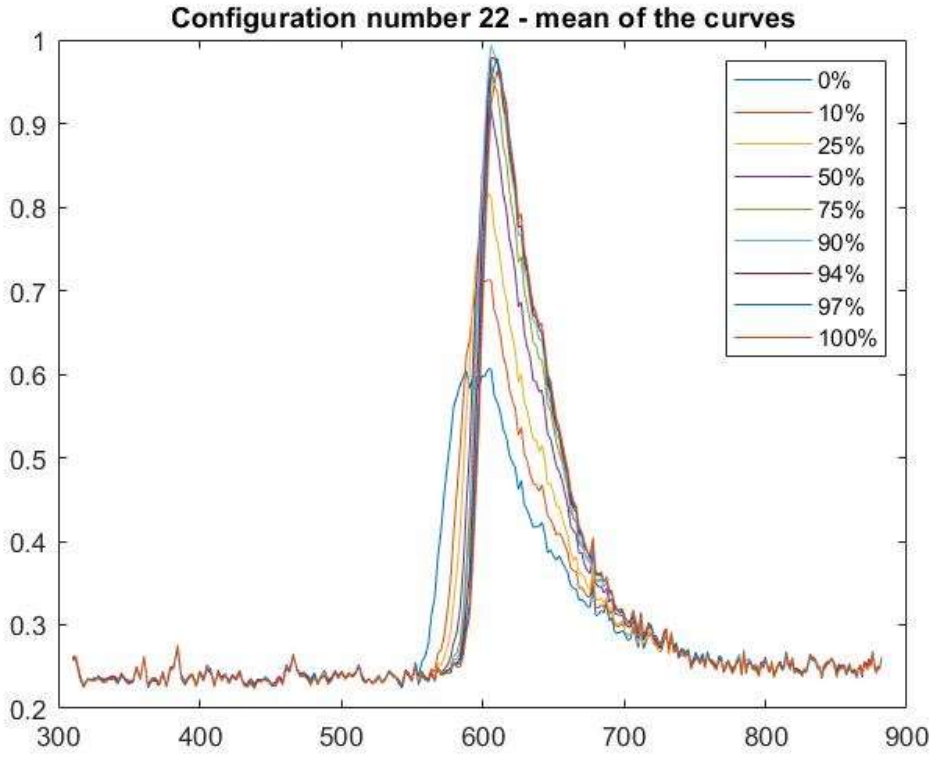

Source: Own authorship (2022).

Figure 50 – Configuration 22 and its peaks

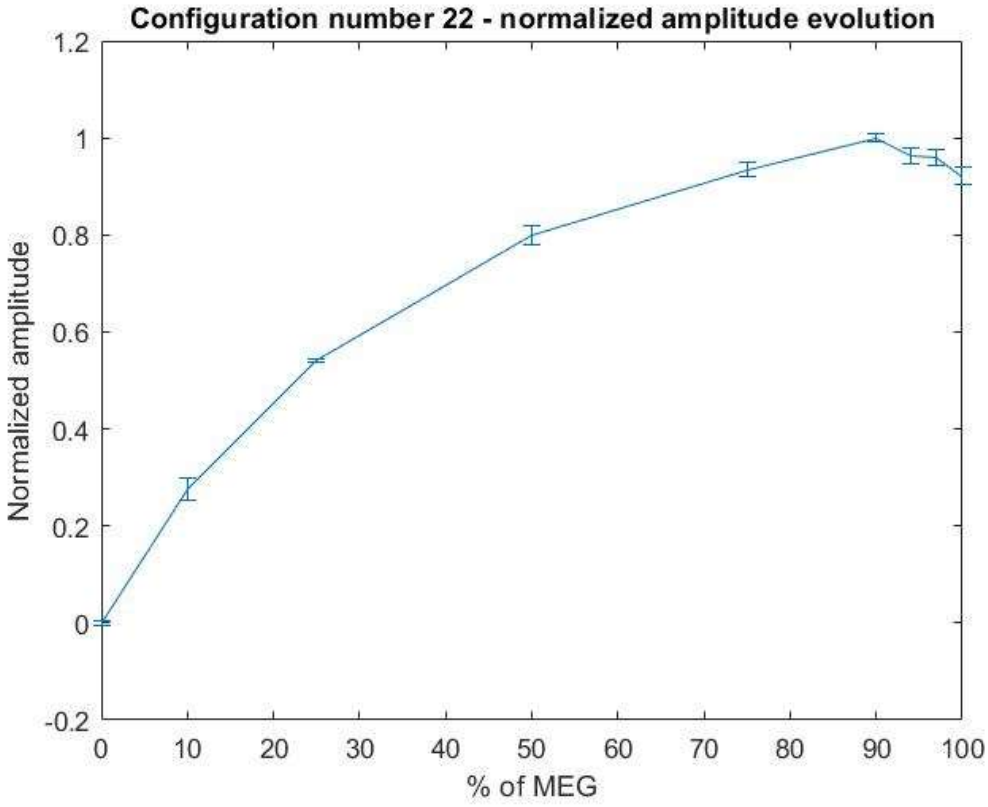

Source: Own authorship (2022).

Figure 51 presents the difference between wavelengths in an incremental mode. Unfortunately, this method does not seem to be satisfactory to assess the liquid's behaviour through UV as well, as the concentrations of 50%, 75% and 90% do not vary. The same can be declared about the 97% and 100% concentrations.

Figure 51 – Configuration 22 and its wavelength shifts

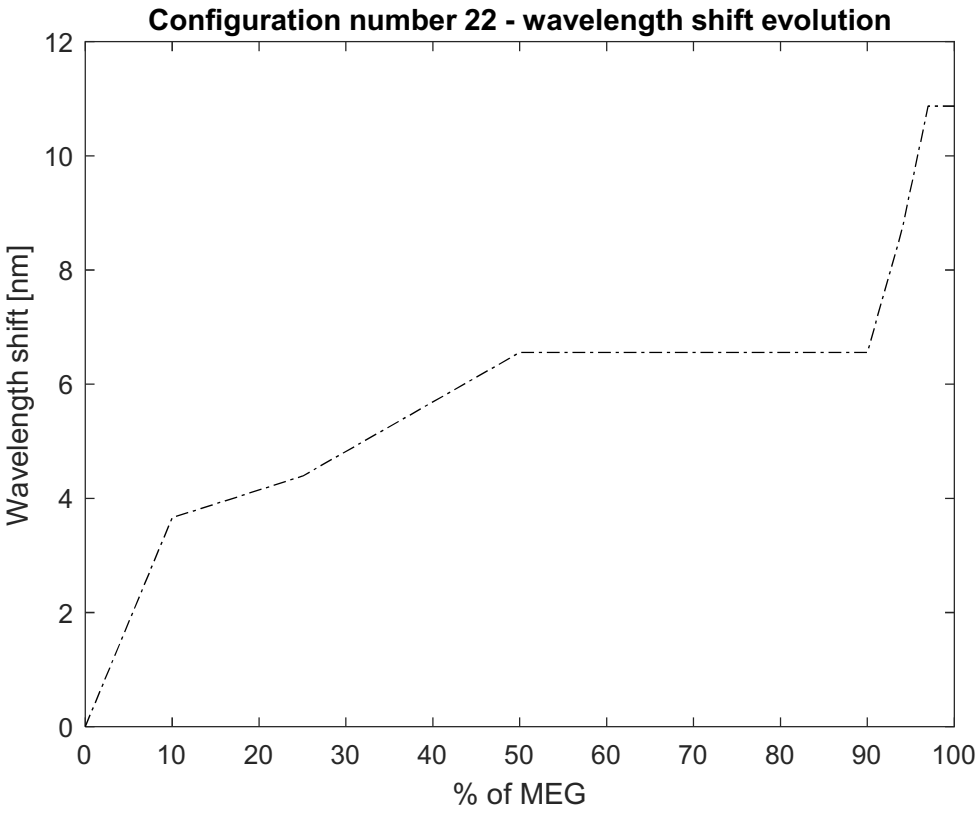

Source: Own authorship (2022).

5.8 Blue LED and processed data

In figures 52, 53 and 54, there can be seen results for the blue LED about overtone, maximum peaks, and wavelength shifts, respectively.

As with UV, the curves have a tendency to get greater as the MEG concentration increases. Still, it also has the same tendency to decline after 90% of MEG.

The peaks amplitudes seem problematic. By them, it can be concluded

that there is no distinction above 90% (and below as well, for a certain extent). The standard deviation, however, is very low, with the biggest one achieving 0.011 (in 25%).

Figure 52 – Configuration 157 and its response

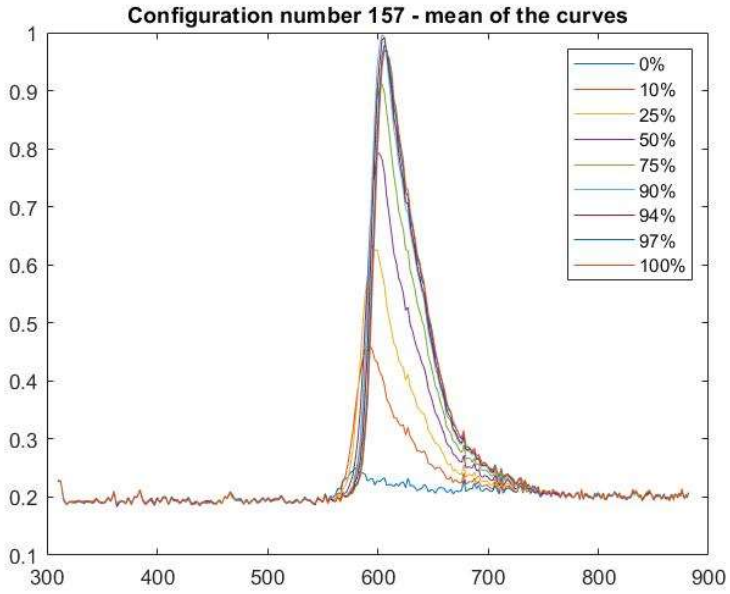

Source: Own authorship (2022).

Figure 53 – Configuration 157 and its peaks

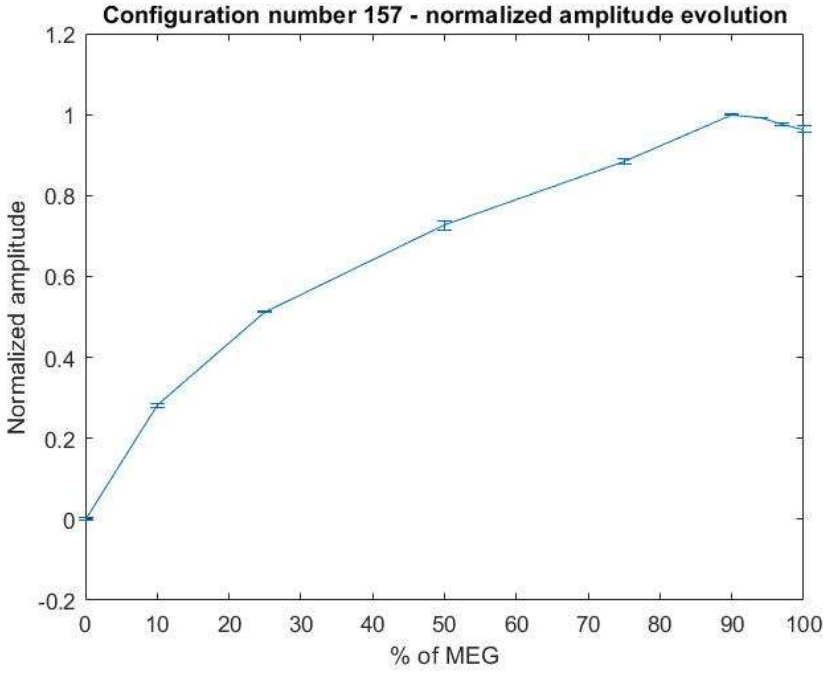

Source: Own authorship (2022).

The wavelength shifts look more promising, especially when compared those from the UV (figure 51). Despite its sharp beginning (from 0% up to 10%), it is reliable to trace a cubic function and assess its behaviour.

Figure 54 – Configuration 157 and its wavelength shifts

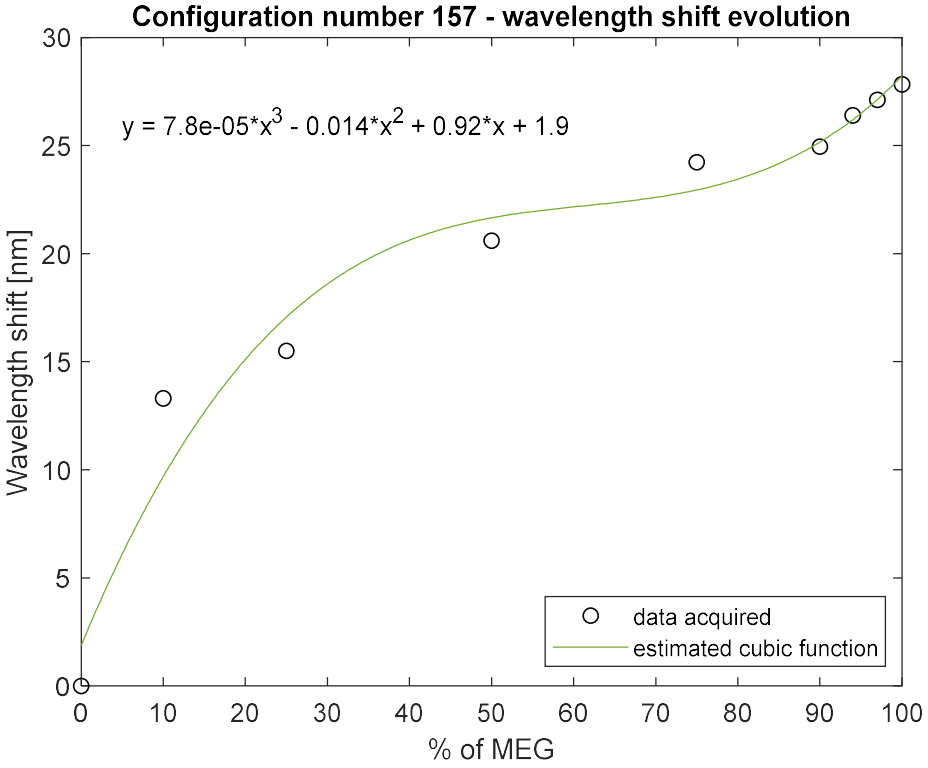

Source: Own authorship (2022).

5.9 Green LED and processed data

In figures 55, 56 and 57, there can be seen results for the green LED about overtone, maximum peaks, and wavelength shifts, respectively.

The curves have a tendency to get smaller as the MEG concentration increases. As it can be observed in both figures 55 and 56, there is a huge gap between 0% and 10%, while there does not appear any significant difference among concentrations beyond 50%. The small standard deviations does not offset the almost flat line between 50% and 90%.

Despite figure 57 appearing better than the previous two, there was actually no difference between 50% and 75%. Even if there was a traced function

to predict the curve's behaviour, there wouldn't have any guarantee that it would inform the correct concentration for any percentage within this range.

Figure 55 – Configuration 19 and its response

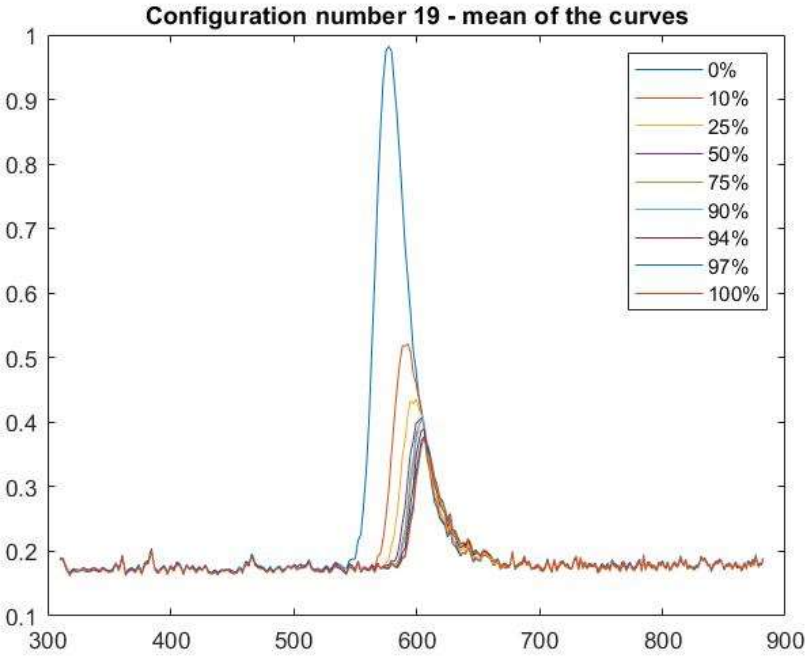

Source: Own authorship (2022).

Figure 56 – Configuration 19 and its peaks

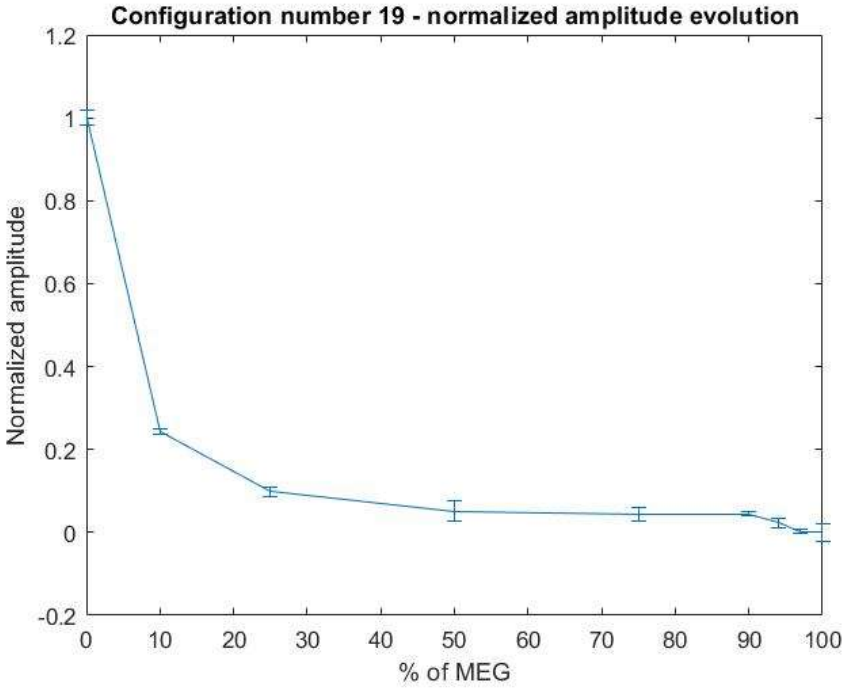

Source: Own authorship (2022).

Figure 57 – Configuration 19 and its wavelength shifts

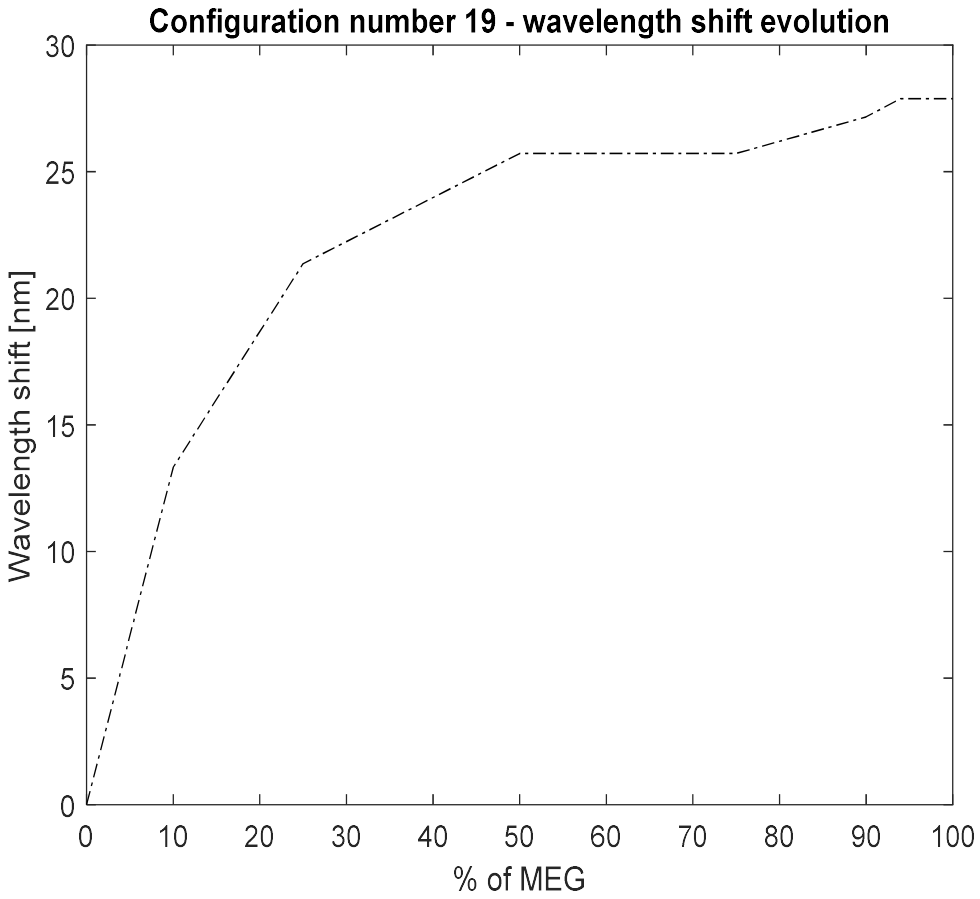

Source: Own authorship (2022).

5.10 Yellow LED and processed data

In figures 58, 59 and 60, there can be seen results for the yellow LED about overtone, maximum peaks, and wavelength shifts, respectively. The results came by adapting the glass flasks in the newest chamber.

As it can be seen, the yellow light has a very similar response to that of the green LED. The main difference between the two is that the yellow LED showed a much better performance at maximum peaks, and arguably a worse performance considering the wavelength shifts.

In fact, the yellow LED is the LED that allows the best prediction of the curves behaviour, to the point of having a more stable cubic function to predict values. This function is presented in the first chart in figure 59. As for the standard deviation, the highest one is 0.057 for the concentration of 75% of MEG. Fortunatelly, the cubic function fits quite well inside the deviations, as the worst

case lies in the 50% mark with approximately just 3% of residual variation (second chart in figure 59).

As for the differences in wavelengths, the results were not as promising. From 10% to 25%, and from 75% to 94%, there were no changes whatsoever. This makes this method of identifying concentrations unreliable.

Figure 58 – Configuration 193 and its overtone

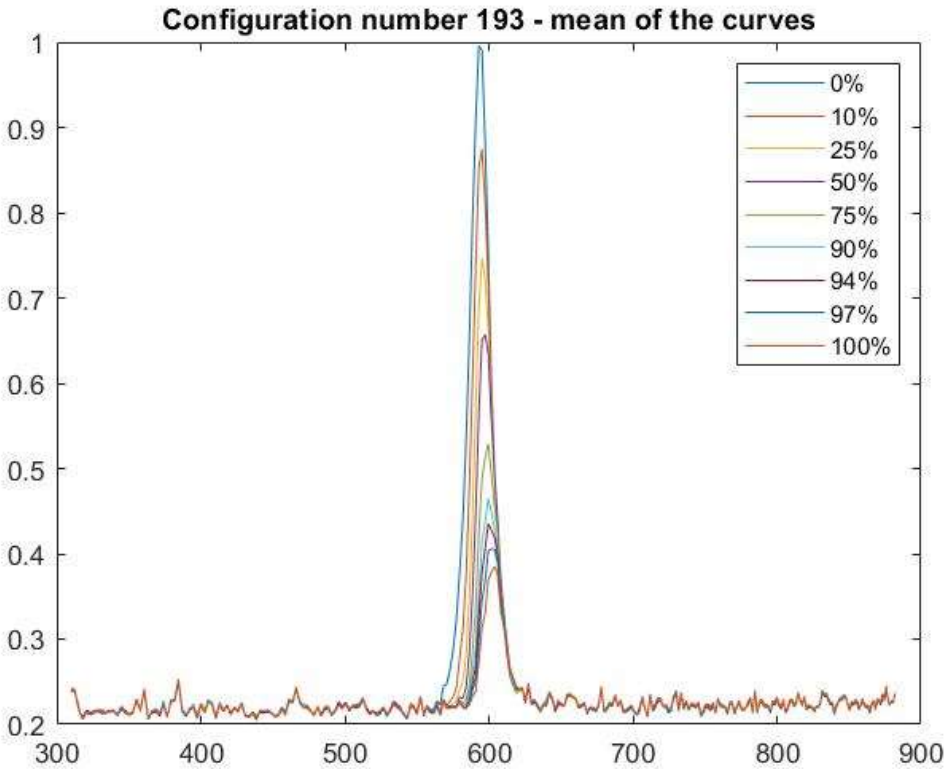

Source: Own authorship (2022).

Figure 59 – Subplot of configuration 193 with its peaks and the residuals.

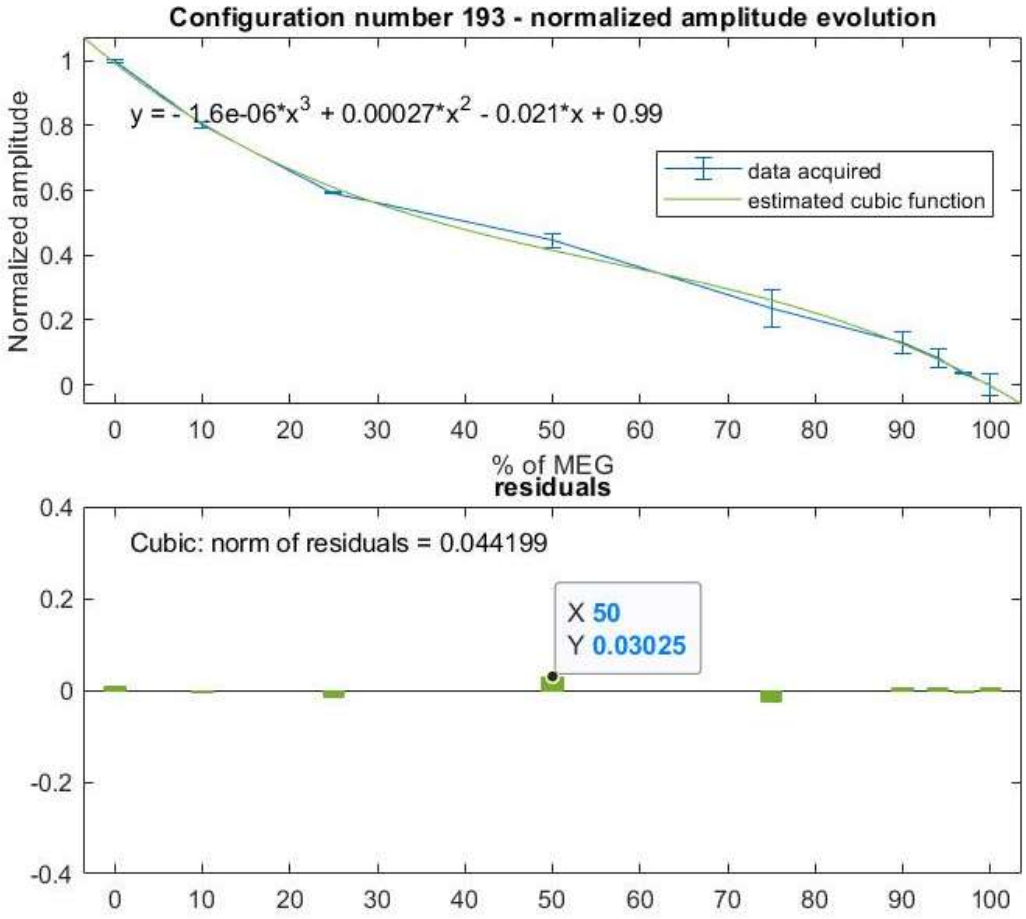

Source: Own authorship (2022).

Figure 60 – Configuration 193 and its wavelength shifts

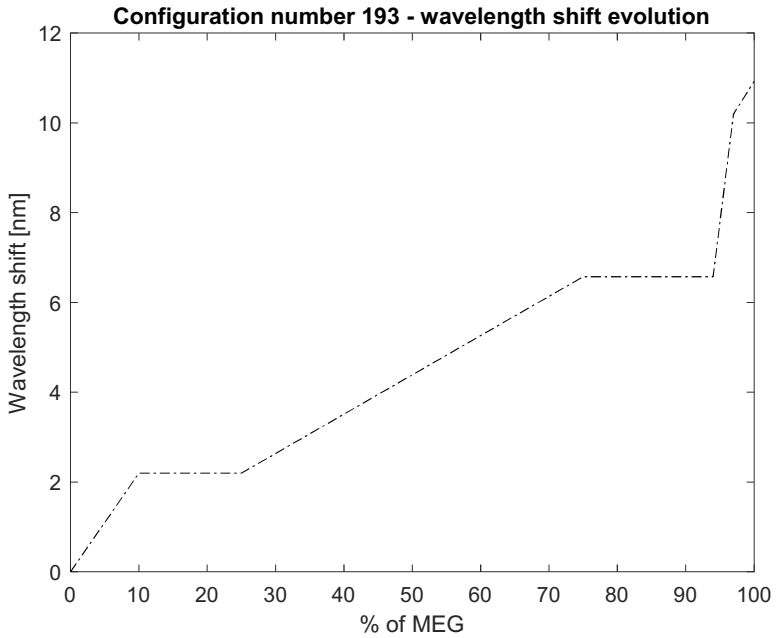

Source: Own authorship (2022).

6 CONCLUSIONS

This work has been all about the measurement of different concentrations of MEG in different configurations. For every aspect of the results, it is worth pointing out that the following items can definitely alter the curves presented:

- chamber's architecture;
- chamber's colour;
- chamber's material;
- flask's material;
- flask's format;
- flask's thickness;
- LED's colour;
- LED's position;
- Sensor (spectrometer);
- dye colour;
- temperature/period of the day;
- filter;
- current reliability;
- sample's quality (contamination and proportion);
- current level.

With these characteristics thus setted, this conclusion is mainly focused on the LED's colours, as they were the main aspects of the experiments.

Before concluding with the LEDs, it is important to conclude that the filters were extremely helpful in shaping the spectrum response of the UV, blue and green LEDs, while not being very useful for the red and yellow LEDs.

The UV LED did not fare very well in the experiments. The wavelength shifts were limited up to 50% of MEG, while the signal's intensities up to 75% of MEG concentration.

The blue LED, which is almost never mentioned in the literature, had either similar or better results than those of the UV. It is clear in figure 53 that the blue LED allows more concentration of MEG to be identified than the UV LED

(higher than 75%, but still lower 90%), when it comes to signals amplitude. As for the wavelength shift, it is possible to trace a cubic function to predict the concentration.

The green LED had an unfortunate result when it came to intensity. The amplitude is difficult to distinguish in roughly half of the concentration samples. As for the wavelength shift, it is better as it is more predictable with a near cubic function. However, one-fourth of the signal is indistinguishable (50%-75%).

The yellow LED had the best results. It had a very near-to-linear amplitude behavior, even accurately traced by a cubic function. The same cannot be affirmed for its wavelength shifts, though, since it has many gaps, as already mentioned.

The red LED had by far the worst results as its curves did not vary in wavelength and its amplitudes did not follow any logical progression whatsoever.

6.1 Considerations about the blue and UV LEDs

Most LEDs curves failed to show some kind of progressive function in both amplitude and wavelength shifts. In order to get around this problem, there were some methods developed to find the most linear or at least the most predictable relation as possible between concentrations and another feature of the spectrum's response for the blue and UV LEDs.

In the case of the UV LED, a cut can be made around the water curve (0%). This curve can then be integrated, obtaining its area and the areas of the other curves within. Then, as the waves shift toward the red spectra, the areas get smaller as the MEG concentration increases. Thereby, there is definitely a progressive logic that could become a function (contrary to what was seen in figures 50 and 51).

An example of this method is shown in figure 61, and its results in figure 62. In order to generate these charts, 15 measures were used from samples from 0% to 100% as shown in figure 30 from 5 configurations presented in table 2. Two of these conditions were measured during mornings (different resistances), two in the afternoons (different resistances), and one at night. A proportional mean was made with all of them, and then they were normalized from 0 to 1.

Figure 61 – Curves delimited by the water curve for the UV LED

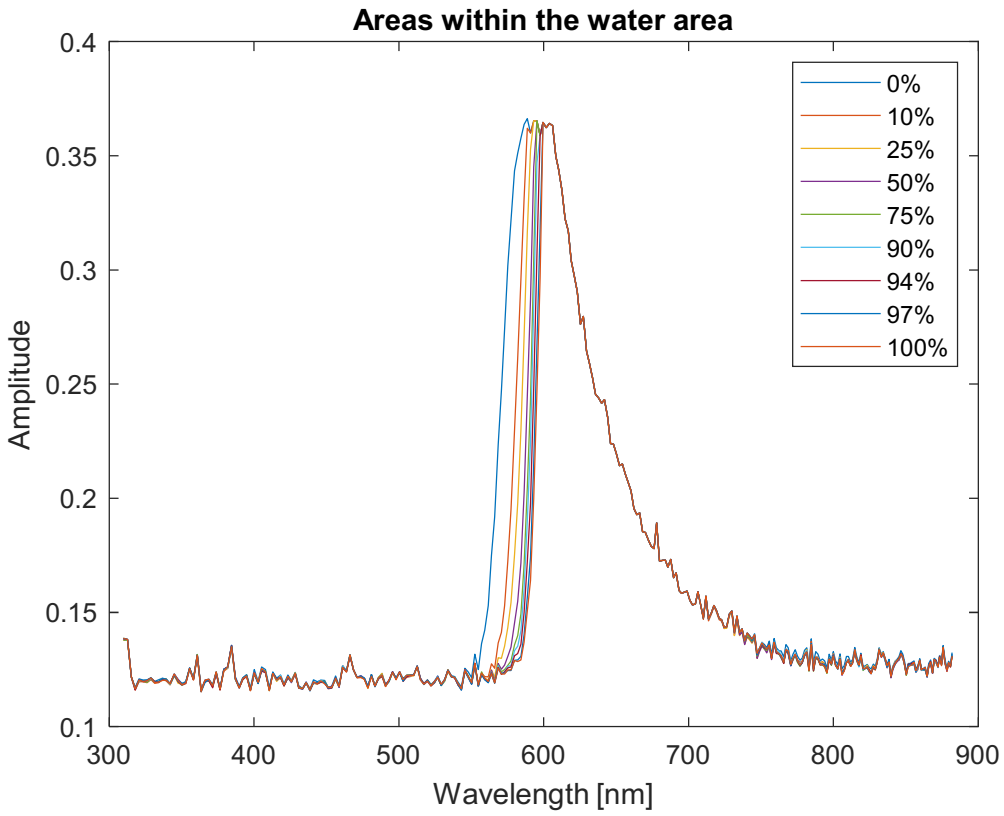

Source: Own authorship (2022).

Figure 62 – Areas size based in many samplesfor the UV LED

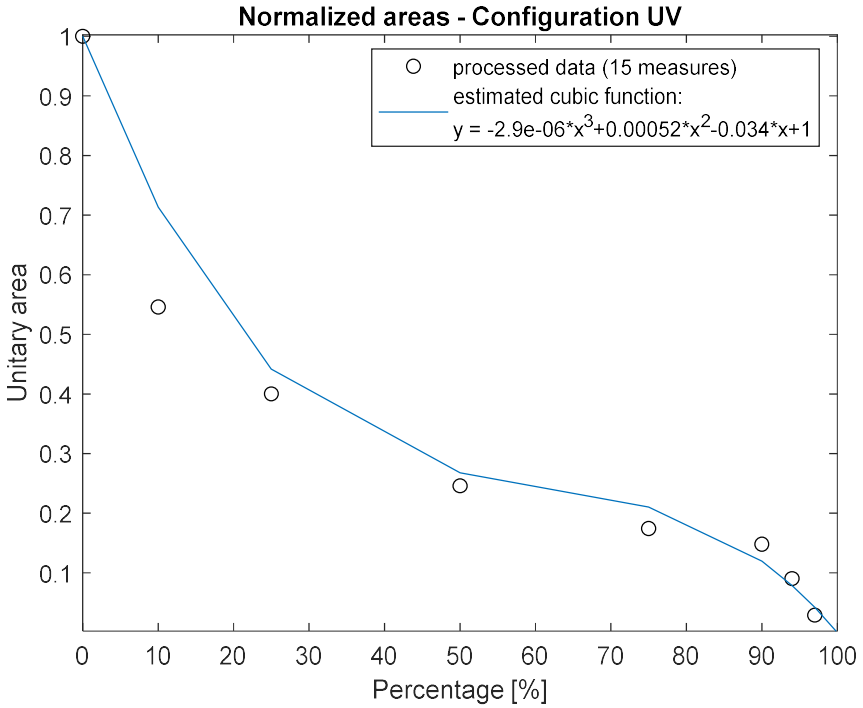

Source: Own authorship (2022).

With the function generated in figure 62, it becomes easier to predict the concentration measure, even if it is far from being linear.

A similar approach could be made in the case of the blue LED as it was made for the UV LED. But this time, a cut would be made within the MEG curve (100%). Figure 63 shows how the curves would be moulded, while figure 64 shows its results in normalized area.

It is noticeable that a cubic function with a closer to linear behaviour could be made to trace the curve's behaviour, which is already an advancement compared to the function presented in figure 54.

It is worth noting that in order to attain these functions, the system would have to be calibrated with the extreme samples (0% and 100% for the UV and blue LEDs, respectively). This should occur ideally close to measuring the other samples, as the MEG's volumetric density varies depending on the environmental temperature.

Figure 63 – Curves delimited by the 100% MEG curve for the blue LED

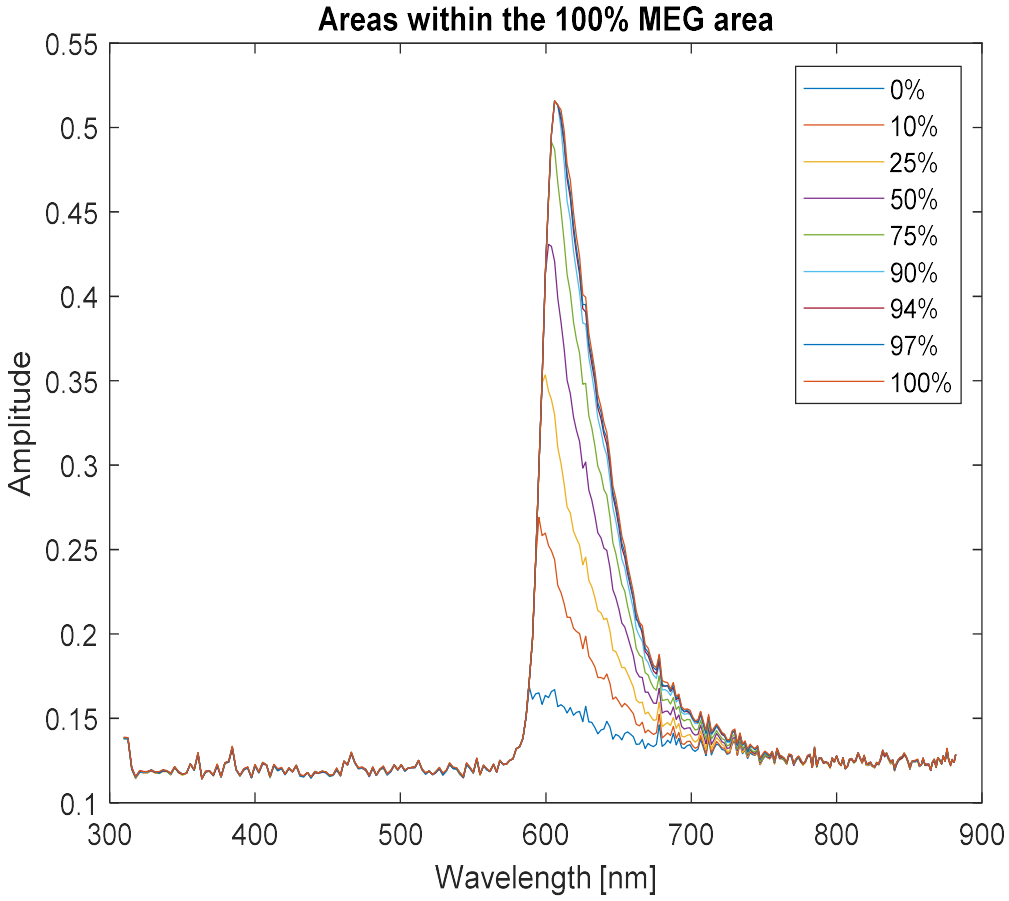

Source: Own authorship (2022).

Figure 64 – Areas size based in many samples for the blue LED

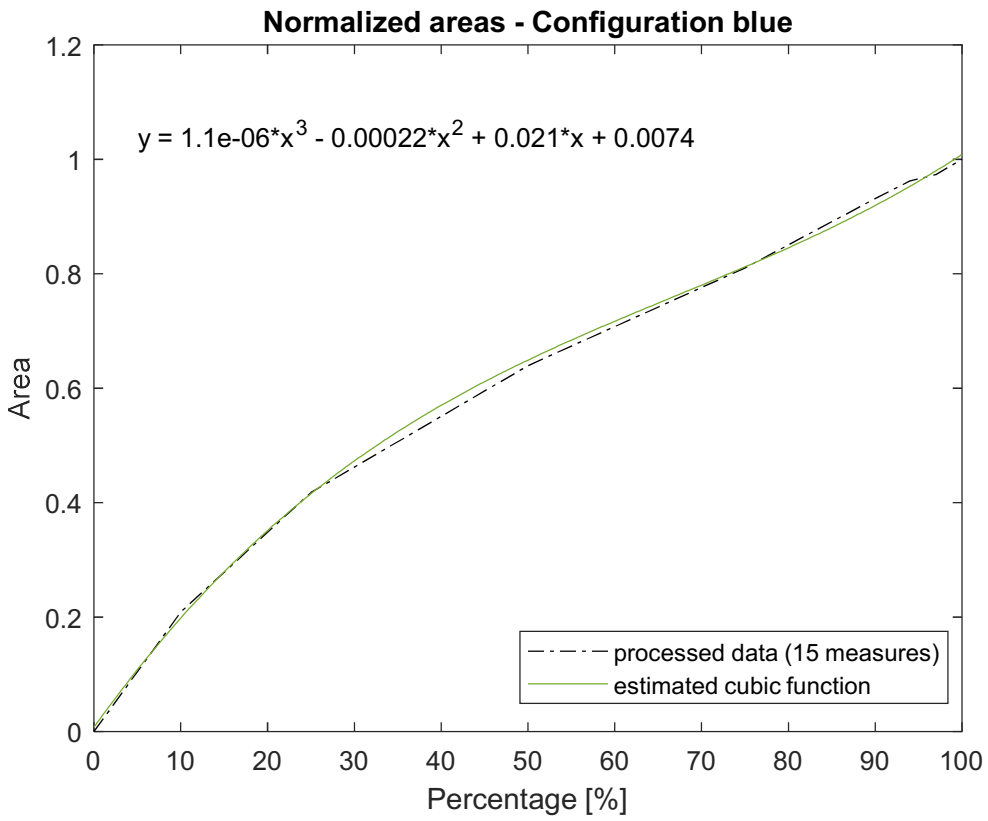

Source: Own authorship (2022).

By comparing figures 62 and 64, it is possible to conclude that the UV harder to predict, in spite of being more reliable to calibrate (as water's volumetric density does not vary according to the temperature, thus varying its volumetric concentration). It also shows that the blue LED could have been overlooked by researchers in general by not considering it in their researches.

6.2 Future works

There are plenty of future works that can be made considering the elaborated points at the beginning of the conclusion section. However, one of the main challenges would be to measure MEG (as well as other THIs) in a bypass mechanism, where there would be a flow of water mixed with MEG. One of the main challenges of this experiment would be to measure accurately any flow type in real time. A flow may have different behaviours according to the

substances quantity and the solution’s flow speed. This creates different shapes of bubbles that may interfere in the sensor’s reading.

Different types of PW with different salinity levels would also be an interesting cases to investigate, especially in the petroleum industry context. Even other substances like moderate oil concentrations could be considered, spectrophotometry-wise.

REFERENCES

ARDUINO PIN CONFIGURATION: Complete Guide 2021. Disponível em: <https://robu.in/arduino-pin-configuration/>. Acesso em: 5 dez. 2022.

ADENIJI, A. O.; OKOH, O. O.; OKOH, A. I. Analytical methods for the determination of the distribution of total petroleum hydrocarbons in the water and sediment of aquatic systems: A review. **Journal of Chemistry**, v. 2017, 2017.

ADISASMITO, S.; PARUBAK, E. Ethylene glycol injection for hydrate formation prevention in deepwater gas pipelines. **MATEC Web of Conferences**, v. 268, p. 02003, 2019.

AN, Z. et al. Liquid holdup measurement in horizontal oilвЂ“water two-phase flow by using concave capacitance sensor. **Measurement : journal of the International Measurement Confederation**, v. 49, p. 153–163, 2014.

ARGO, C. B. et al. Commercial deployment of low-dosage hydrate inhibitors in a Southern North Sea 69 km wet-gas subsea pipeline. **SPE Production & Facilities**, v. 15, n. 02, p. 130–134, 2000.

BALADO SÁNCHEZ, C. et al. Spectrophotometers for labs: A cost-efficient solution based on smartphones. **Computer Applications in Engineering Education**, v. 27, n. 2, p. 371–379, mar. 2019.

BALDIN, R. **RafBal / Mestrado**. Disponível em: <https://github.com/RafBal/Mestrado>. Acesso em: 11 jan. 2023.

DITTES, N. Water in Grease Condition Monitoring Literature Review. p. 18, 2013.

FERREIRA, G. M.; BALDIN, R. **IMPLEMENTAÇÃO DE ESPECTROFOTÔMETRO DE BAIXO CUSTO PARA MONITORAMENTO DE QUALIDADE DE GASOLINA**. Curitiba, Paraná, Brasil: Universidade Federal do Paraná, 2019.

FU, B. et al. Application of low-dosage hydrate inhibitors in deepwater operations. **SPE Production & Facilities**, v. 17, n. 03, p. 133–137, 2002.

GAO, S. Investigation of interactions between gas hydrates and several other flow assurance elements. **Energy & Fuels**, v. 22, n. 5, p. 3150–3153, 2008.

GRAS, K. et al. Determination of ethylene glycol in lubricants by derivatization static headspace gas chromatography. **Analytical Methods**, v. 7, n. 13, p. 5545–5550, 2015.

HAGHI, R. K.; YANG, J.; TOHIDI, B. Integrated near infrared and ultraviolet spectroscopy techniques for determination of hydrate inhibitors in the presence of nacl. **Industrial and Engineering Chemistry Research**, v. 57, n. 34, p. 11728–11737, 2018.

HU, X.; WANG, J. A simple route of modifying copper electrodes for the determination of methanol and ethylene glycol. **Electroanalysis**, v. 24, n. 7, p.

1639–1645, 2012.

IGWE, C. O.; SAADI, A. A. L.; NGENE, S. E. Optimal Options for Treatment of Produced Water in Offshore Petroleum Platforms Journal of Pollution Effects & Control. **Journal of Pollution Effects & Control**, v. 1, n. 1, p. 1–5, 2013.

KURAIMID, Z. K. et al. Treatment of Produced Water Generated at Alommara Oil Field-Missan Oil Company, IRAQ for Reinjection Application. **Chemical Methodologies**, v. 5, n. 4, p. 348–355, 2021.

LEDERHOS, J. P. et al. Effective kinetic inhibitors for natural gas hydrates. **Chemical Engineering Science**, v. 51, n. 8, p. 1221–1229, 1996.

LEE, J.-B. et al. The comparison of derivatization methods for the determination of ethylene glycol in lubricant oil sample by GC/MS. **Bulletin of the Korean Chemical Society**, v. 33, n. 12, p. 4243–4246, 2012.

LEE, J. et al. On□fiber Derivatization for Determination of Ethylene Glycol Concentration in Lubricant oil By SPME□GC/MS. **Bulletin of the Korean Chemical Society**, v. 37, n. 6, p. 938–941, 2016.

LUONG, J. et al. Determination of trace ethylene glycol in industrial solvents and lubricants using phenyl boronic acid derivatization and multidimensional gas chromatography. **Analytica chimica acta**, v. 805, p. 101–106, 2013.

MAHANTA, D. K.; LASKAR, S. Water Quantity-Based Quality Measurement of Transformer Oil Using Polymer Optical Fiber as Sensor. **IEEE Sensors Journal**, v. 18, n. 4, p. 1506–1512, 2018.

MAHENDRA SINGH. **Monoethylene Glycol (MEG) Demand to Surge at 5.4% CAGR Amid Burgeoning Demand for Polyester Fibre**. Disponível em: <https://www.prnewswire.com/news-releases/monoethylene-glycol-meg-demand-to-surge-at-5-4-cagr-amid-burgeoning-demand-for-polyester-fibre-301617817.html>. Acesso em: 27 mar. 2023.

MASSARO, A. et al. Optical performance evaluation of oil spill detection methods: Thickness and extent. **IEEE Transactions on Instrumentation and Measurement**, v. 61, n. 12, p. 3332–3339, 2012.

MCDOWELL, G. R.; UTTAMLAL, M.; GRAHAM, A. A Novel In-Line Fibre-Optic Sensor for the Detection of Hydrate Inhibitors within the Oil and Gas Industry. p. 4–6, 2016.

MECH, D.; GUPTA, P.; SANGWAI, J. S. Kinetics of methane hydrate formation in an aqueous solution of thermodynamic promoters (THF and TBAB) with and without kinetic promoter (SDS). **Journal of Natural Gas Science and Engineering**, v. 35, p. 1519–1534, 2016.

MITCHELL, G. F.; TALLEY, L. D. **Application of kinetic hydrate inhibitor in black-oil flowlines**. SPE Annual Technical Conference and Exhibition. **Anais**...OnePetro, 1999.

MOHAMAD, E. J. et al. Measurement and analysis of water/oil multiphase flow using Electrical Capacitance Tomography sensor. **Flow Measurement and Instrumentation**, v. 47, p. 62–70, 2016.

MOKHTARI, B.; POURABDOLLAH, K. Determination of hydrate inhibitor in crude oil by nanoextraction–gas chromatography. **Journal of Separation Science**, v. 35, n. 1, p. 79–85, 1 jan. 2012.

NNUAR, N. A. A. et al. Spatial distribution of petroleum hydrocarbon in sediments of major rivers from east coast of peninsular Malaysia. **Coastal Marine Science**, v. 32, n. 1, p. 9–18, 2008.

NOTZ, P. K. et al. Application of kinetic inhibitors to gas hydrate problems. **SPE Production & Facilities**, v. 11, n. 04, p. 256–260, 1996.

PAIVA, V. M. et al. Electrochemical analysis of monoethylene glycol using rGO/AuPd-np-modified glassy carbon electrode. **Bulletin of Materials Science**, v. 44, n. 4, p. 14–16, 2021.

PAL, A.; VASUKI, B. Void fraction measurement using concave capacitor based sensor вЂ“ Analytical and experimental evaluation. **Measurement : journal of the International Measurement Confederation**, v. 124, p. 81–90, 2018.

PERERA, K. et al. Imaging of oil-water flow patterns by Electrical Capacitance Tomography. **Flow Measurement and Instrumentation**, v. 56, p. 23–34, 2017.

PERRY, C. W.; GIGLIELLOK, K. **EPA perspective on current RCRA enforcement trends and their application to oil and gas production wastes**. Proceedings of the US Environmental Protection Agency's First International Symposium on Oil and Gas Exploration and Production Waste Management Practices, New Orleans, LA. **Anais**...1990.

PRODROMIDIS, M. I. et al. Amperometric Detection of Periodate Using a Graphite Electrode Modified with a Novel α□Keggin□Type Silicotungstic Acid Salt and Determination of Ethylene Glycol in Antifreeze Fluids. **Electroanalysis: An International Journal Devoted to Fundamental and Practical Aspects of Electroanalysis**, v. 13, n. 11, p. 960–966, 2001.

QUEIROZ, A.; RODRIGUEZ, J. E. N.; CAJAIBA, J. Programmable actuator based on RGB monitoring for detection and dissociation of gas hydrates. **Journal of Natural Gas Science and Engineering**, v. 84, n. May, 2020.

RAWLINGS, A. V.; LOMBARD, K. J. **A review on the extensive skin benefits of mineral oil. International Journal of Cosmetic Science**, dez. 2012.

REYNA, C. A. B. et al. Water content monitoring in water-in-oil emulsions using an Ultrasonic Multiple-Backscattering Sensor. **Machines**, v. 9, n. 12, p. 1–10, 2021.

SANDENGEN, K.; KAASA, B. Estimation of Monoethylene Glycol (MEG) Content in Water + MEG + NaCl + NaHCO3 Solutions. **Journal of Chemical & Engineering Data**, v. 51, n. 2, p. 443–447, 1 mar. 2006.

SARDESHPANDE, M. V; HARINARAYAN, S.; RANADE, V. V. Void fraction measurement using electrical capacitance tomography and high speed photography. **Chemical Engineering Research and Design**, v. 94, p. 1–11, 2015.

SEMENOV, A. P. et al. Inhibiting gas hydrate formation by polymer–

monoethylene glycol mixture. **Chemistry and Technology of Fuels and Oils**, v. 52, n. 1, p. 43–51, 2016.

SHELL. **Monoethylene glycol**. Disponível em: <https://www.shell.com/business-customers/chemicals/factsheets-speeches-and-articles/factsheets/mono-ethylene-glycol.html>. Acesso em: 9 set. 2022.

SHILLIDAY, E. R. et al. Quantitative measurement of Mono-Ethylene Glycol (MEG) content using low-field Nuclear Magnetic Resonance (NMR). **Journal of Natural Gas Science and Engineering**, v. 101, n. February, p. 104520, 2022.

SHOUKAT, U.; BAUMEISTER, E.; KNUUTILA, H. K. **ATR-FTIR Model Development and Verification for Qualitative and Quantitative Analysis in MDEA–H2O–MEG/TEG–CO2 Blends**. **Energies**, 2019.

STRAZZA, D. et al. Capacitance sensor for hold-up measurement in high-viscous-oil/conductive-water core-annular flows. **Flow measurement and instrumentation**, v. 22, n. 5, p. 360–369, 2011.

STRØMGREN, T. et al. Acute toxic effects of produced water in relation to chemical composition and dispersion. **Marine Environmental Research**, v. 40, n. 2, p. 147–169, 1995.

STROTHER, T.; LOWRY, S.; BRAVO, B. **Measurement of Dispersed Oil in Water Using an Infrared Analysis Method**, 1987. (Nota técnica).

VEXIM. **Mono ethylene glycol antifreeze coolant**. Disponível em: <https://www.equilex.com/products/ethylene-glycol>. Acesso em: 27 mar. 2023.

WIKIMEDIA COMMONS CONTRIBUTORS. **File : EM spectrum . svg**. Disponível em: <https://commons.wikimedia.org/w/index.php?title=File:EM_spectrum.svg&oldid=680392141>. Acesso em: 18 ago. 2022.

WU, H. et al. Design of a Conductance and Capacitance Combination Sensor for water holdup measurement in oilвЂ“water two-phase flow. **Flow measurement and instrumentation**, v. 46, p. 218–229, 2015.

WU, Y. et al. Occurrence of n-alkanes and polycyclic aromatic hydrocarbons in the core sediments of the Yellow Sea. **Marine Chemistry**, v. 76, n. 1, p. 1–15, 2001.

YANG, J.; TOHIDI, B. Characterization of inhibition mechanisms of kinetic hydrate inhibitors using ultrasonic test technique. **Chemical Engineering Science**, v. 66, n. 3, p. 278–283, 2011.

YANG, J.; TOHIDI, B. Determination of hydrate inhibitor concentrations by measuring electrical conductivity and acoustic velocity. **Energy and Fuels**, v. 27, n. 2, p. 736–742, 2013.

YANG, W. Q. Hardware design of electrical capacitance tomography systems. **Measurement Science and Technology**, v. 7, n. 3, p. 225–232, 1996.

YANG, W. Q.; PENG, L. Image reconstruction algorithms for electrical capacitance tomography. **Measurement Science and Technology**, v. 14, n. 1, p. R1–R13, 2002.

YANG, Y. et al. Area-alterable liquid electrode capacitance sensor for water holdup measurement in oil–water two-phase flow. **Asia-Pacific Journal of Chemical Engineering**, v. 16, n. 5, p. 13–15, 2021.

ZABOON, S. et al. Recovery of mono-ethylene glycol by distillation and the impact of dissolved salts evaluated through simulation of field data. **Journal of Natural Gas Science and Engineering**, v. 44, p. 214–232, 2017.

ZHAI, L. et al. Liquid holdup measurement with double helix capacitance sensor in horizontal oil–water two-phase flow pipes. **Chinese Journal of Chemical Engineering**, v. 23, n. 1, p. 268–275, 2015.

ATTACHMENT 1 - HAMAMATSU C12880MA DATASHEET

HAMAMATSU
PHOTON IS OUR BUSINESS

Micro-spectrometer

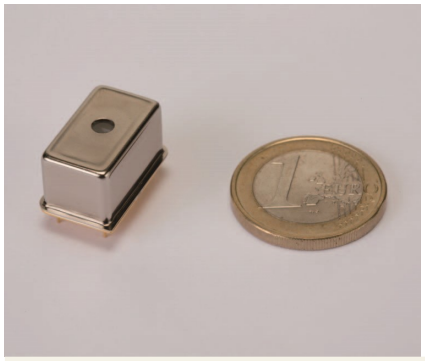

C12880MA

Finger-tip sized, ultra-compact spectrometer head supporting high sensitivity and long wavelength region

The C12880MA is a high-sensitivity, ultra-compact (finger-tip sized) spectrometer head that supports the long wavelength region (up to 850 nm). Hermetically sealed packaging provides improved humidity resistance. This product is suitable for integration into a variety of compact devices.

Features

- **Finger-tip size: 20.1 × 12.5 × 10.1 mm**
- **Weight: 5 g**
- **Spectral response range: 340 to 850 nm**
- **High sensitivity**
- **Spectral resolution: 15 nm max.**
- **Supports synchronized integration (electronic shutter function)**
- **Hermetic package: high reliability against humidity**
- **For integration into mobile measurement equipment**
- **Wavelength conversion factors*1 are listed on final inspection sheet.**

Applications

- **Food inspection**
- **Biometry (POC)**
- **Tester for lights, LEDs, etc.**
- **Water quality control monitors and other environment measuring instruments**
- **Various light level measurements**

*1: Conversion factors for converting the image sensor pixel number into a wavelength. A calculation factor for converting the A/D converted count into the input light level is not provided.

Structure

Parameter	Specification	Unit
Image sensor	High-sensitivity CMOS linear image sensor with slit	-
Number of pixels	288	pixels
Pixel size (H × V)	14 × 200	µm
Slit*2 (H × V)	50 × 500	µm
NA*3	0.22	-
Dimensions (W × D × H)	20.1 × 12.5 × 10.1	mm
Weight	5	g

*2: Entrance slit aperture size
*3: Numeric aperture (solid angle)

Absolute maximum ratings (Ta=25 °C unless otherwise noted)

Parameter	Symbol	Condition	Value	Unit
Supply voltage	Vs max		-0.3 to +6	V
Clock pulse voltage	V(CLK)		-0.3 to +6	V
Start pulse voltage	V(ST)		-0.3 to +6	V
Operating temperature	Topr	No dew condensation*4	+5 to +50	°C
Storage temperature	Tstg	No dew condensation*4	-20 to +70	°C

*4: When there is a temperature difference between a product and the surrounding area in high humidity environment, dew condensation may occur on the product surface. Dew condensation on the product may cause deterioration in characteristics and reliability.
Note: Exceeding the absolute maximum ratings even momentarily may cause a drop in product quality. Always be sure to use the product within the absolute maximum ratings.

Recommended terminal voltage (Ta=25 °C)

Parameter		Symbol	Min.	Typ.	Max	Unit
Supply voltage		Vs	4.75	5	5.25	V
Clock pulse voltage	High level	V(CLK)	Vs - 0.25	Vs	Vs + 0.25	V
	Low level		0	-	0.3	
Start pulse voltage	High level	V(ST)	Vs - 0.25	Vs	Vs + 0.25	V
	Low level		0	-	0.3	

Electrical characteristics [Ta=25 °C, Vs=5 V, V(CLK)=V(ST)=5 V]

Parameter	Symbol	Min.	Typ.	Max	Unit
Clock pulse frequency	f(CLK)	0.2	-	5	MHz
Video rate	VR	-	f(CLK)	-	Hz
Output impedance*5	Zo	-	150	-	Ω
Current consumption*6	I	-	20	-	mA

*5: Video signal output terminal (10-pin)
An increase in the current consumption at the video output terminal also increases the chip temperature and so causes the dark current to rise. To avoid this, connect a buffer amplifier to the video output terminal so that the current flow is minimized.
*6: f(CLK)=5 MHz

Electrical and optical characteristics [Ta=25 °C, Vs=5 V, V(CLK)=V(ST)=5 V]

Parameter	Symbol	Min.	Typ.	Max	Unit
Conversion efficiency	CE	-	50	-	$\mu V/e^-$
Dark output voltage*7	Vd	-	0.8	-	mV
Saturation output voltage*8	Vsat	-	4.3	-	V
Readout noise	Nr	-	1.8	-	mV rms
Output offset voltage	Vo	0.3	0.5	0.9	V
Spectral response range	λ	-	340 to 850	-	nm
Spectral resolution (FWHM)	-	-	12	15	nm
Wavelength reproducibility*9	λr	-0.5	-	+0.5	nm
Wavelength temperature dependence	λTd	-0.1	-	+0.1	nm/°C
Spectral stray light*10	SL	-	-	-25	dB

*7: Integration time=10 ms
*8: Relative value in reference to output offset voltage Vo
Example: When output offset voltage Vo is 0.5 V and saturation output voltage Vsat is 4.3 V, the saturation voltage at the video signal output terminal is 4.8 V.
*9: Measured under constant light input conditions
*10: The ratio of the count measured when a light spectrum (655 nm) is input to the count measured at that wavelength ± 40 nm.

Optical component layout

Besides a CMOS image sensor chip integrated with an optical slit by etching technology, the C12880MA employs a reflective concave blazed grating formed by nanoimprint. In addition, the glass used in the light path of the previous C10988MA-01 is not used in the C12880MA, making it extremely compact.

Structure

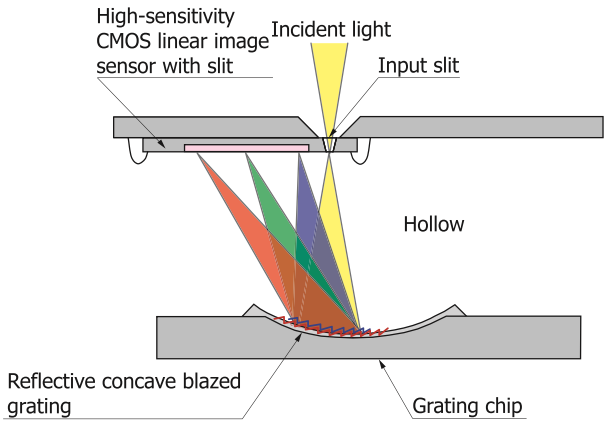

KACCC0757EB

High-sensitivity CMOS linear image sensor with a slit [Incident light side (back of chip)]

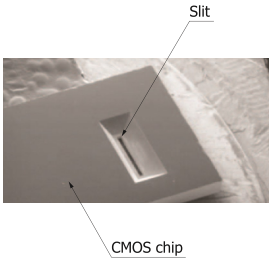

Spectral response (typical example)

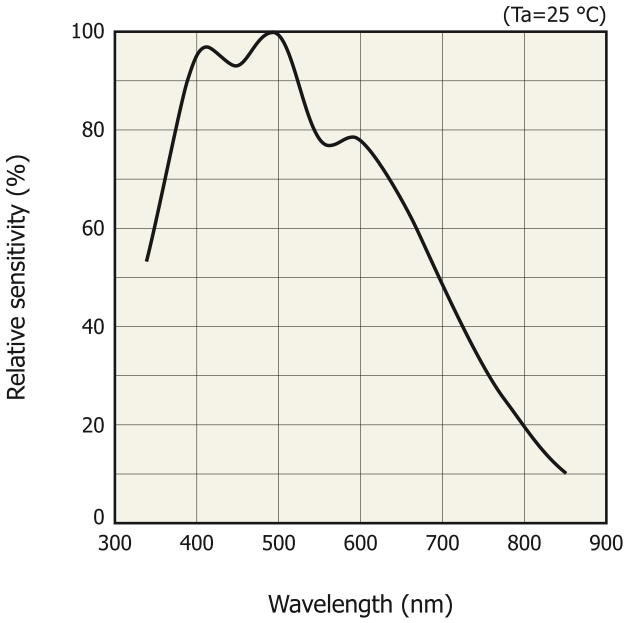

KACCB0381EA

Spectral resolution vs. wavelength (typical example)

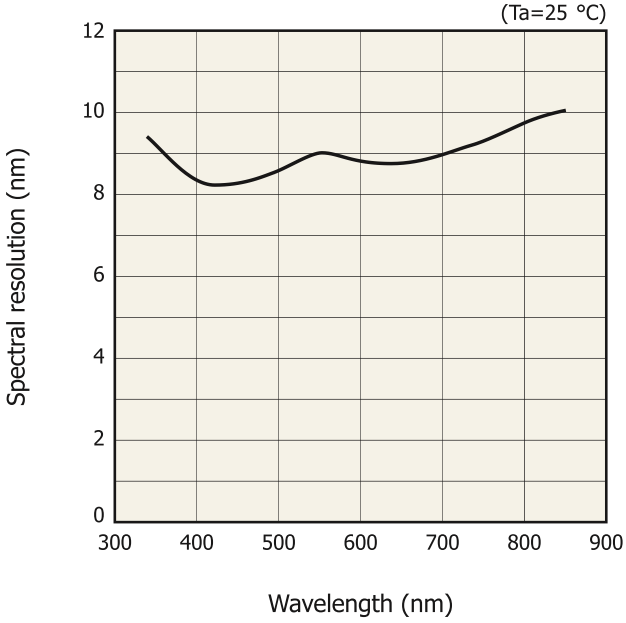

KACCB0382EA

Linearity (typical example)

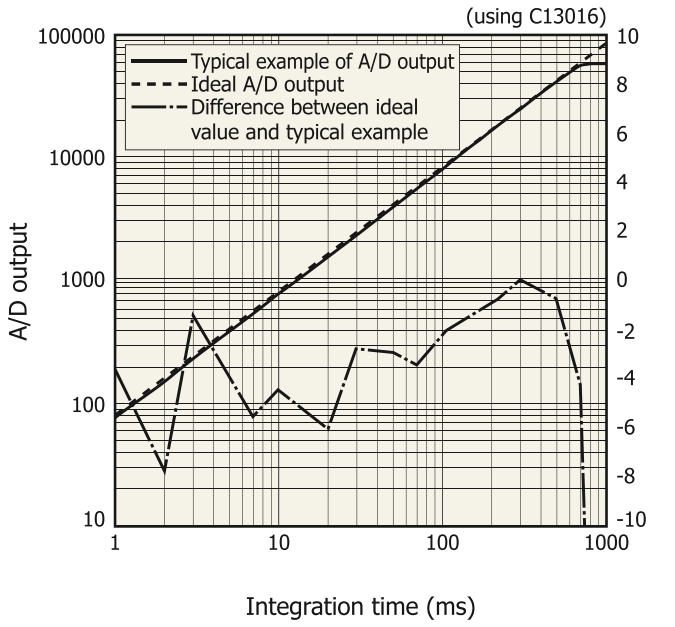

KACCB0383EA

A/D output is the output with dark output is subtracted when light is input. The difference between the ideal value and typical example contains a measurement error. The smaller the A/D output, the larger the measurement error.

Dark output vs. ambient temperature (typical example)

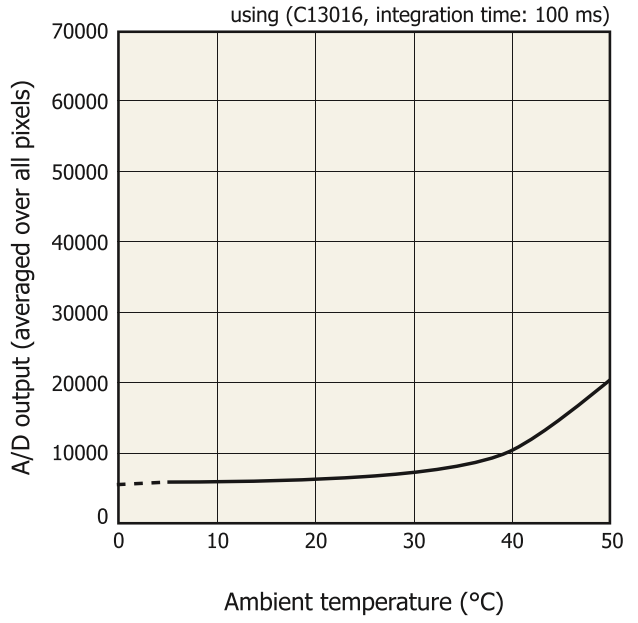

KACCB0384EA

A/D output is the sum of the sensor and circuit offset outputs and the sensor dark output.

Measurable incident light level

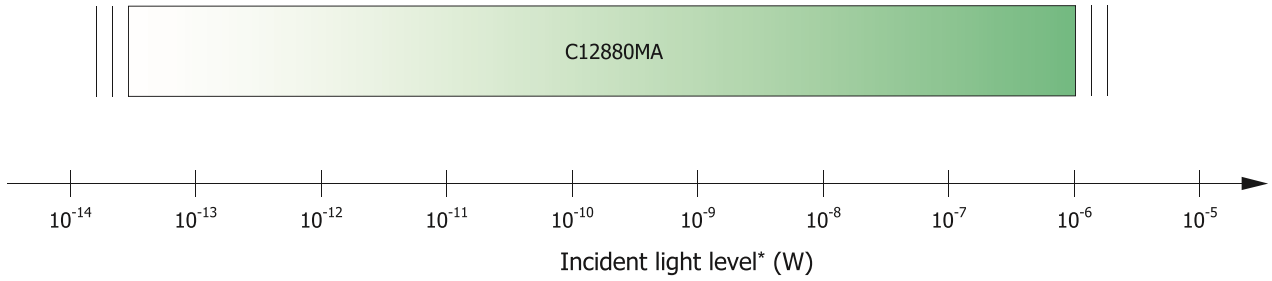

* Using C13016, input spot diameter 800 µm (λ=600 nm)

KACCB385EA

Recommended driver circuit example

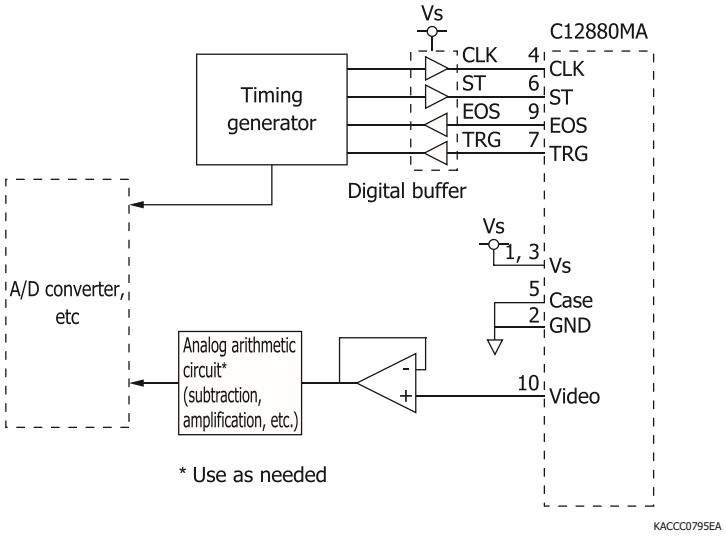

Precautions

· The packaging of the C12880MA is electrically conductive, so be careful when designing the circuit to avoid short circuit caused by contact with a circuit pattern.
· If external force is repeatedly applied to the lead pins, this may damage the lead pins.
· To prevent damage due to soldering, be careful of the soldering temperature and time.
As a general guide, finish soldering within 3.5 seconds at 350 °C or less when soldering by hand, or within 10 seconds at 260 °C or less when using a solder bath.

Dimensional outline (unit: mm, tolerance unless otherwise noted: ±0.2)

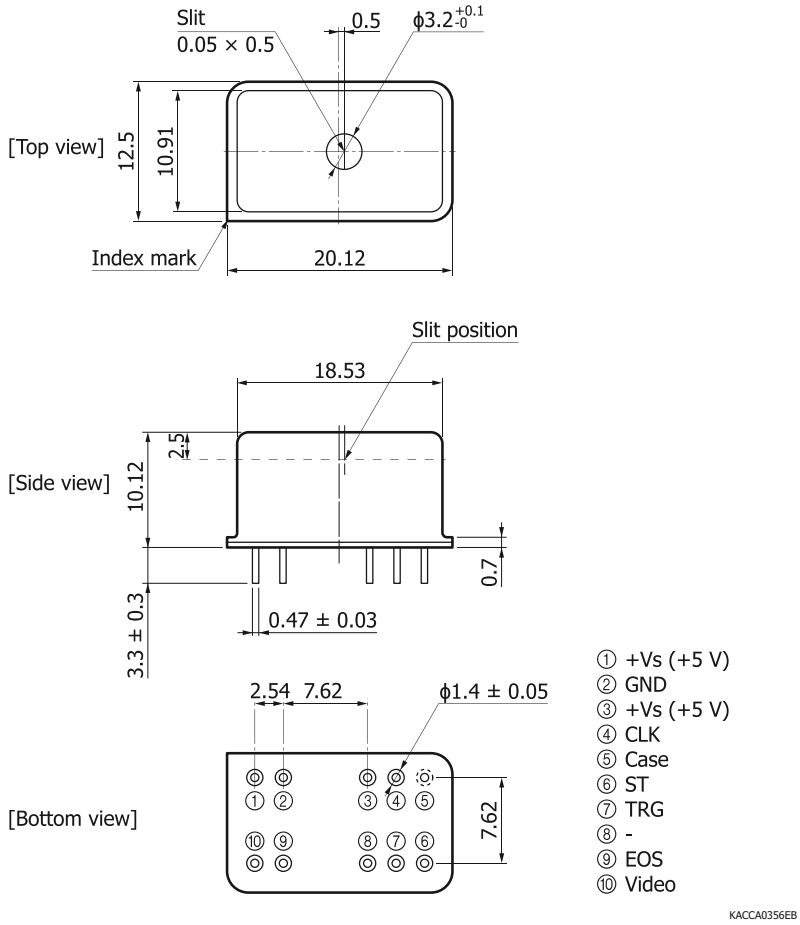

Pin connections

Make electrical connections to an external circuit using leads.

Pin no.	Symbol	Name	I/O	Description
1	+Vs	Supply voltage	I	Sensor power supply: 5 V
2	GND	Ground	-	Sensor ground
3	+Vs	Supply voltage	I	Sensor power supply: 5 V
4	CLK	Clock pulse	I	Sensor clock pulse
5	Case	Case	-	Case connection
6	ST	Start pulse	I	Sensor start pulse
7	TRG	Trigger pulse	O	Pulse for capturing sensor video signals
8	-	Fastening pin	-	Do not connect electrically.
9	EOS	End of scan	O	Sensor scan end
10	Video	Video output	O	Sensor video output

Note: Pin no. 5 and the case of the micro-spectrometer are at the same potential. Ensure that the case is not in contact with other potentials during use. Parts coming in contact with the case must be set at the same potential as pin no. 5 or insulated from other potentials.

Timing chart

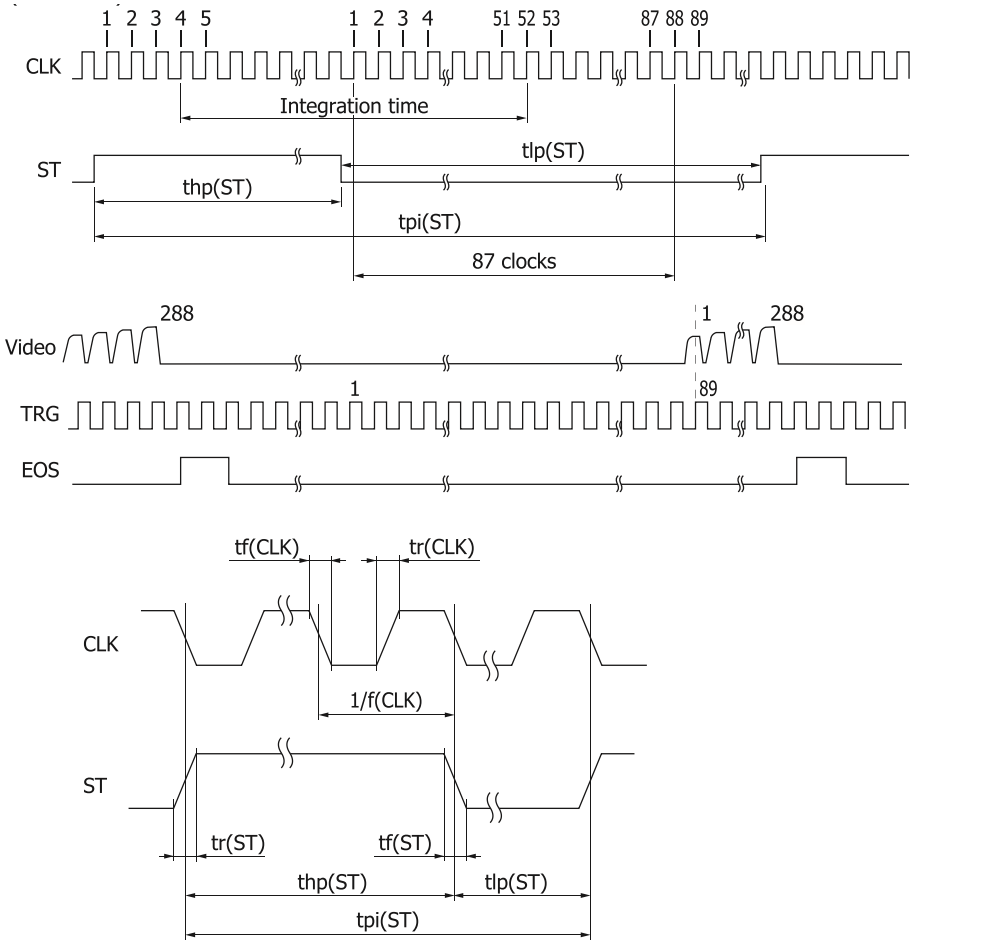

KACCC0771EA

Parameter	Symbol	Min.	Typ.	Max.	Unit
Start pulse cycle*11	tpi(ST)	381/f(CLK)	-	-	s
Start pulse high period*12	thp(ST)	6/f	-	-	s
Start pulse low period	tlp(ST)	375/f	-	-	s
Start pulse rise and fall times	tr(ST), tf(ST)	0	10	30	ns
Clock pulse duty	-	45	50	55	%
Clock pulse rise and fall times	tr(CLK), tf(CLK)	0	10	30	ns

*11: The shortest period required to output the video signals from all pixels.
*12: The integration time equals the high period of ST plus 48 CLK cycles.
The shift register starts operation at the rising edge of CLK immediately after ST goes low.
The integration time can be changed by changing the ratio of the high and low periods of ST.
If the first TRG pulse after ST goes low is counted as the first pulse, the Video signal should be acquired at the rising edge of the 89th TRG pulse.

Operation example

This is an operating example when the clock pulse frequency is set to maximum (video data rate is also set to maximum), the time per scan to minimum, and the integration time to maximum.

- Clock pulse frequency [f(CLK)] = Video data rate
  = 5 MHz

- Start pulse cycle [tpi(ST)] = 381/f(CLK)
  = 381/5 MHz
  = 76.2 µs

- Low period of start pulse min. [tlp(ST)] = 375/f(CLK)
  = 375/5 MHz
  = 75 µs

- High period of start pulse [thp(ST)] = Start pulse cycle [tpi(ST)] - Low period of start pulse min. [tlp(ST)]
  = 76.2 µs - 75 µs
  = 1.2 µs

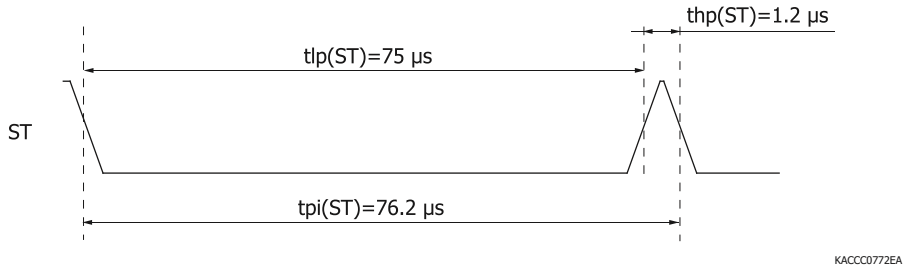

Integration time is equal to the high period of start pulse + 48 cycles of clock pulses, so it will be 1.2 µs + 9.6 µs = 10.8 µs.

Mini-spectrometer/micro-spectrometer lineup

Type no.	Type		Spectral response range(nm)	Spectral resolution max. (nm)	Image sensor
C10082CA	Mini-spectrometer TM Series	TM-UV/VIS-CCD High sensitivity		6	Back-illuminated type CCD Image sensor
C10082CAH		TM-UV/VIS-CCD High resolution	200 to 800	1*	
C10082MD		TM-UV/VIS-MOS Wide dynamic range		6	CMOS linear image sensor
C10083CA		TM-VIS/NIR-CCD High sensitivity		8 (Wavelength 320 to 900 nm)	Back-thinned CCD image sensor
C10083CAH		TM-VIS/NIR-CCD High resolution	320 to 1000	1* (Wavelength 320 to 900 nm)	
C10083MD		TM-VIS/NIR-MOS Wide dynamic range		8	CMOS linear image sensor
C11697MB		TM-VIS/NIR-MOS-II Trigger compatibility		8	High-sensitivity CMOS linear image sensor
C9404CA	Mini-spectrometer TG Series	TG-UV-CCD High sensitivity		3	Back-thinned CCD image sensor
C9404CAH		TG-UV-CCD High resolution	200 to 400	1*	Back-thinned CCD image sensor
C9405CB		TG-SWNIR-CCD-II IR enhanced	500 to 1100	5 (Wavelength 550 to 900 nm)	IR-enhanced back-thinned CCD image sensor
C11713CA		TG-RAMAN-I High resolution	500 to 600	0.3*	Back-thinned CCD image sensor
C11714CB		TG-RAMAN-II High resolution	790 to 920	0.3*	IR-enhanced back-thinned CCD image sensor
C11482GA	Mini-spectrometer TG Series	TG2-NIR Non-cooled type		7	InGaAs linear image sensor
C9913GC		TG-cooled NIR-I Low noise(Cooled type)	900 to 1700	7	
C9914GB		TG-cooled NIR-II Low noise(Cooled type)	1100 to 2200	8	
C11118GA		TG-cooled NIR-III Low noise(Cooled type)	900 to 2550	20	
C13555MA	Mini-spectrometer TF Series	TF-VIS-MOS-II Compact, thin case	340 to 830	3	High-sensitivity CMOS linear image sensor
C13053MA		TF-SWIR-MOS-II Compact, thin case	500 to 1100	3.5	
C14486GA		TF-NIR Compact, thin case	950 to 1700	5*	InGaAs linear image sensor
C13054MA		TF-RAMAN Compact, thin case	790 to 920	0.4*	High-sensitivity CMOS linear image sensor
C14214MA		TF-RAMAN Compact, thin case	790 to 1050	0.6	
C11007MA	Mini-spectrometer RC series	RC-VIS-MOS Spectrometer module	340 to 780	9	CMOS linear image sensor
C11008MA		RC-SWNIR-MOS Spectrometer module	640 to 1050	8	IR-enhanced CMOS linear image sensor

* Typ. Value

For incorporation into mobile measurement devices

Type no.	Type		Spectral response range(nm)	Spectral resolution max. (nm)	Image sensor
C11009MA	Mini-spectrometer RC series	RC-VIS-MOS Spectrometer head	340 to 780	9	CMOS linear image sensor
C11010MA		RC-SWNIR-MOS Spectrometer head	640 to 1050	8	IR-enhanced CMOS linear image sensor

For incorporation into mobile measurement devices (Ultra-compact)

Type no.	Type		Spectral response range(nm)	Spectral resolution max. (nm)	Image sensor
C11708MA	Mini-spectrometer MSseries	MS-SWNIR-MOS Spectrometer head	640 to 1050	20	CMOS linear image sensor
C12666MA	Micro-spectrometer	Spectrometer head	340 to 780	15	CMOS linear image sensor
C12880MA		Spectrometer head	340 to 850	15	High-sensitivity CMOS linear image sensor

Related information

www.hamamatsu.com/sp/ssd/doc_en.html

■ Precautions
· Disclaimer

■ Technical information
· Mini-spectrometers

HAMAMATSU www.hamamatsu.com

HAMAMATSU PHOTONICS K.K., Solid State Division
1126-1 Ichino-cho, Higashi-ku, Hamamatsu City, 435-8558 Japan, Telephone: (81) 53-434-3311, Fax: (81) 53-434-5184
U.S.A.: Hamamatsu Corporation: 360 Foothill Road, Bridgewater, N.J. 08807, U.S.A., Telephone: (1) 908-231-0960, Fax: (1) 908-231-1218, E-mail: usa@hamamatsu.com
Germany: Hamamatsu Photonics Deutschland GmbH: Arzbergerstr. 10, D-82211 Herrsching am Ammersee, Germany, Telephone: (49) 8152-375-0, Fax: (49) 8152-265-8, E-mail: info@hamamatsu.de
France: Hamamatsu Photonics France S.A.R.L.: 19, Rue du Saule Trapu, Parc du Moulin de Massy, 91882 Massy Cedex, France, Telephone: 33-(1) 69 53 71 00, Fax: 33-(1) 69 53 71 10, E-mail: infos@hamamatsu.fr
United Kingdom: Hamamatsu Photonics UK Limited: 2 Howard Court, 10 Tewin Road, Welwyn Garden City, Hertfordshire AL7 1BW, United Kingdom, Telephone: (44) 1707-294888, Fax: (44) 1707-325777, E-mail: info@hamamatsu.co.uk
North Europe: Hamamatsu Photonics Norden AB: Torshamnsgatan 35 16440 Kista, Sweden, Telephone: (46)8-509 031 00, Fax: (46)8-509 031 01, E-mail: info@hamamatsu.se
Italy: Hamamatsu Photonics Italia S.r.l.: Strada della Moia, 1 int. 6, 20020 Arese (Milano), Italy, Telephone: (39)02-93 58 17 33, Fax: (39)02-93 58 17 41, E-mail: info@hamamatsu.it
China: Hamamatsu Photonics (China) Co., Ltd.: B1201, Jiaming Center, No.27 Dongsanhuan Beilu, Chaoyang District, Beijing 100020, China, Telephone: (86) 10-6586-6006, Fax: (86) 10-6586-2866, E-mail: hpc@hamamatsu.com.cn
Taiwan: Hamamatsu Photonics Taiwan Co., Ltd.: 8F-3, No. 158, Section2, Gongdao 5th Road, East District, Hsinchu, 300, Taiwan R.O.C. Telephone: (886)03-659-0080, Fax: (886)03-659-0081, E-mail: info@hamamatsu.com.tw

Cat. No. KACC1226E08 Aug. 2018 DN

ATTACHMENT 2 - HAMAMATSU RANGE OF SPECTROPHOTOMETERS

Micro-spectrometers, MS series

Ultra-compact spectrometer heads

Wide dynamic range C12666MA
High sensitivity C12880MA
For near IR C11708MA

Based on an advanced MOEMS technology, a thumb-sized ultra-compact spectrometer heads have been achieved by combining an input-slit-integrated CMOS image sensor and grating formed through nanoimprint on a convex lens. As they employ an easily mountable package, you can use them as though they were sensors.

Spectral response (RC/MS series, micro-spectrometers)

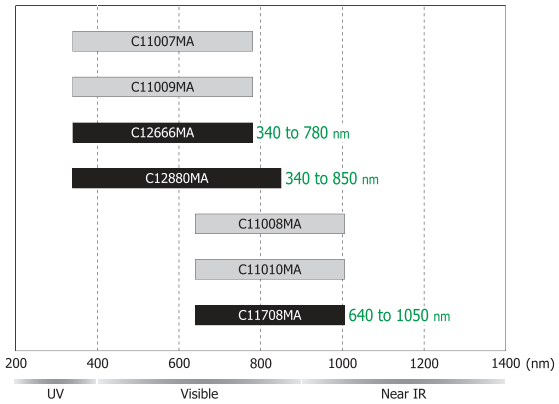

KACCB0388EA

Features

- Ultra-compact
- Hermetically sealed package:
  High reliability under humid conditions (C12666MA, C12880MA)
- For installation into mobile measuring devices
- Wavelength conversion factor*7 is listed on final inspection sheet.

Applications

[C12666MA, C12880MA]

- Color monitoring on printers, printing presses, etc.
- Tester for lights, LEDs, etc.
- Display color adjustment
- Water quality control monitors and other environment measuring instruments
- Measuring instruments that use portable devices, such as smartphones and tablets

[C11708MA]

- Sugar content measurement of fruits
- Taste evaluation of grains
- Composition analysis

*7: A factor for converting image sensor pixel numbers to wavelengths. A calculation factor for converting the A/D converted count into a value proportional to the input light level is not provided.

Specifications (Ta=25 °C)

Parameter	Micro-spectrometer		MS series	Unit
	C12666MA	C12880MA	C11708MA	
Photo				-
Type	Spectrometer head / Wide dynamic range	Spectrometer head / High sensitivity	Spectrometer head / For near IR	-
Spectral response range	340 to 780	340 to 850	640 to 1050	nm
Spectral resolution (FWHM)*1	15 max.		20 max.	nm
Wavelength reproducibility*2	-0.5 to +0.5			mm
Wavelength temperature dependence	-0.1 to +0.1		-0.05 to +0.05	nm/°C
Spectral stray light*1 *3	-25 max.			dB
Dimensions (W × D × H)	20.1 × 12.5 × 10.1		27.6 × 16.8 × 13	mm
Weight	5		9	g
Image sensor	CMOS linear image sensor	High-sensitivity CMOS linear image sensor	CMOS linear image sensor	-
Number of pixels	256	288	256	pixels
Slit (H × V)*4	50 × 750	50 × 500	75 × 750	μm
NA*5	0.22			-
Operating temperature*6	+5 to +50			°C
Storage temperature*6	-20 to +70			°C
Trigger compatible	-			-
Evaluation circuit (sold separately)	C14465-10	C13016	C14465	-

Note: We also provide the C12880MA-10, which is identical to the C12880MA except that it has an SMA connector.

Measurable incident light level

CMOS image sensor built into the C12666MA has a large saturation charge, and that built into the C12880MA has a large charge-to-voltage conversion gain.
To perform high S/N measurement, the C12666MA is recommended when the incident light level is high and the C12880MA when the level is low.

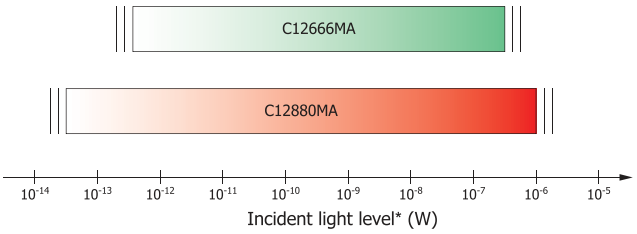

* Input spot diameter: 800 μm (λ=550 nm)
The measurable light level is calculated from the settable integration time.
The settable integration time is different between the C12666MA and C12880MA.
The S/N during measurement is not taken into account.

KACCB0354EA

Micro-spectrometer evaluation circuit

A circuit board designed to simply evaluate the characteristics of the micro-spectrometer is available (sold separately). The micro-spectrometer is connected to a PC with a USB cable A9160 (AB type, sold separately). Evaluation software is included.

C14465-10 and C12666MA

Evaluation software display example

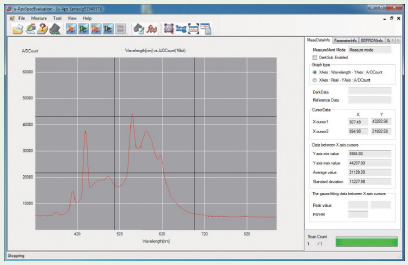

Connection example

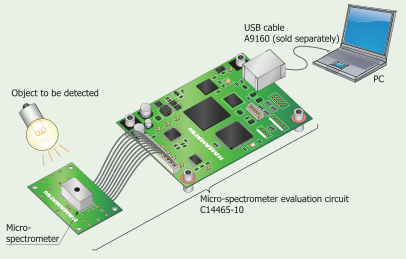

KACCC0799EB

*1: When the slit in the table is used. The spectral resolution depends on the slit. *2: Measured under constant light input and other conditions *3: The ratio of the count measured when the following wavelength light is input to the count measured when that wavelength ±40 nm light is input, C12666MA: 560 nm, C12880MA: 655 nm, C11708MA: 850 nm *4: Input slit aperture size *5: Numeric aperture (solid angle) *6: No dew condensation

ATTACHMENT 3 - HAMAMATSU C12880MA CALIBRATION TABLE

HAMAMATSU

HAMAMATSU PHOTONICS K.K

			2018 / 03 / 19
FINAL INSPECTION SHEET 検査成績書			HAMAMATSU PHOTONICS K.K. SOLID STATE DIVISION 浜松ホトニクス株式会社　固体事業部
Name	Micro-Spectrometer	Approved by 責任者	Yosuke Matsuno
Type No.	C12880MA	Inspected by 検査員	Shinya Ohta
Date Inspected: 検査日：	2017/ 10/ 12　24.0 °C　～　2017/ 10/ 17　24.0 °C		

*1) Wavelength resolution: Test conditions / Maximum value of FWHM at 340nm, 400nm, 450nm, 500nm, 550nm, 600nm, , 655nm, 710nm, 760nm, 810nm, 850nm wavelength
波長分解能　：検査条件　/ 波長340nm, 400nm, 450nm, 500nm, 550nm, 600nm, , 655nm, 710nm, 760nm, 810nm, 850nmのFWHMの最大値

	Calibration coefficients　Wavelength[nm]=$A_0+B_1*pix+B_2*pix^2+B_3*pix^3+B_4*pix^4+B_5*pix^5$ 波長変換係数						Wavelength resolution *1) 波長分解能	
Serial No.	A_0	B_1	B_2	B_3	B_4	B_5	Standard for Shipment 出荷基準 [nm]	Result
17I00590	3.058378720E+02	2.705700264E+00	−1.278460348E−03	−6.524451154E−06	5.298714185E−09	9.920513162E−12	≦15	9.6
17I00591	3.060296379E+02	2.705434692E+00	−1.156550769E−03	−7.409532680E−06	8.489893036E−09	5.245897834E−12		8.8
17I00592	3.050442961E+02	2.706106765E+00	−1.272996920E−03	−5.730124763E−06	−4.426834800E−10	2.073015896E−11		9.6
17I00593	3.057776934E+02	2.697982093E+00	−1.145747807E−03	−7.718892820E−06	9.891532291E−09	3.535326558E−12		8.9
17I00594	3.116462449E+02	2.705513292E+00	−1.433070963E−03	−5.114527701E−06	−6.233238479E−10	1.908385669E−11		9.7
17I00595	3.052577632E+02	2.712451830E+00	−1.407120031E−03	−4.706807554E−06	−3.796645369E−09	2.484096755E−11		9.0
17I00596	3.071188765E+02	2.710355256E+00	−1.368366888E−03	−5.161080308E−06	−1.645262382E−09	2.137989782E−11		9.8
17I00618	3.060042613E+02	2.736722784E+00	−1.772317105E−03	−2.812893538E−06	−7.739925344E−09	2.720689069E−11		10.8
17I00619	3.159141628E+02	2.689066261E+00	−1.237086247E−03	−6.547177413E−06	4.112548453E−09	1.332710776E−11		10.3
17I00620	3.223245445E+02	2.687989109E+00	−1.166866909E−03	−7.387676867E−06	8.085566747E−09	6.639998101E−12		10.3
17I00621	3.179260581E+02	2.692255983E+00	−1.200230169E−03	−6.812614974E−06	4.770215829E−09	1.282168982E−11		9.9
17I00622	3.103713273E+02	2.697263697E+00	−1.328643191E−03	−5.399831998E−06	−7.956255474E−10	2.014496745E−11		9.8
17I00624	3.054838699E+02	2.707215114E+00	−1.269350245E−03	−5.801025318E−06	−2.709694057E−10	2.085404272E−11		9.5
17I00625	3.042955747E+02	2.706509065E+00	−1.295913282E−03	−6.028386749E−06	1.992461094E−09	1.633848756E−11		8.9
17I00626	3.081329429E+02	2.697384791E+00	−1.065246848E−03	−8.284240396E−06	1.198022534E−08	4.416570136E−13		9.2
17I00630	3.053678031E+02	2.710709064E+00	−1.396166726E−03	−5.422446350E−06	7.708270360E−10	1.665877262E−11		9.5
17I00634	3.082062153E+02	2.704793941E+00	−1.249434201E−03	−6.482950807E−06	5.065538987E−09	9.465479187E−12		8.7
17I00636	3.081233409E+02	2.722485964E+00	−1.692429237E−03	−3.078709774E−06	−7.279473796E−09	2.679983619E−11		9.6
17I00642	3.100074571E+02	2.712574575E+00	−1.458442871E−03	−4.384048695E−06	−4.531058091E−09	2.515413593E−11		9.1
17I00643	3.062381820E+02	2.721821525E+00	−1.585340129E−03	−3.436069465E−06	−7.359380146E−09	2.802066721E−11		9.4